Title
High Resolution Additive Patterning of Nanoparticles and Polymers Enabled by Vapor Permeable Polymer Templates

Author
Demko, Michael Thomas

Publication Date
2012

Peer reviewed|Thesis/dissertation

High Resolution Additive Patterning of Nanoparticles and Polymers Enabled by Vapor Permeable Polymer Templates

By

Michael Thomas Demko

A dissertation submitted in partial satisfaction of the

requirements for the degree of

Doctor of Philosophy

in

Engineering - Mechanical Engineering

in the

Graduate Division

of the

University of California, Berkeley

Committee in charge:

Professor Albert P. Pisano, Chair
Professor Liwei Lin
Professor Ming C. Wu

Spring, 2012

Abstract

High Resolution Additive Patterning of Nanoparticles and Polymers

Enabled by Vapor Permeable Polymer Templates

by

Michael Thomas Demko

Doctor of Philosophy in Engineering - Mechanical Engineering

University of California, Berkeley

Professor Albert P. Pisano, Chair

The structure and chemistry of nanoparticles and polymers are interesting for applications in electronics and sensors. However, because they are outside of the standard material set typically used for these applications, widespread use of these materials has not yet been realized. This is due in part to the limited ability of traditional manufacturing processes to adapt to these unique materials. As a result, several alternative manufacturing methods have been developed, including nanoimprint lithography, gravure printing, inkjet printing, and screen printing, among many others. However, these current processes are not able to simultaneously produce patterns with high resolution and high dimensional fidelity, rapidly, over large areas, and in a completely additive manner.

In this work, a novel template-based manufacturing process for patterning nanoparticles and polymers is developed. This process uses vapor permeable polymers as templates for patterning nanoparticle or polymer inks, consisting of the solutes dissolved in a carrier solvent. Briefly, a template is filled with clean solvent and an evaporation-driven flow is used to fill the templates with ink. Continued evaporation is used to completely remove the solvent from the ink, leaving only solidified solute and therefore preventing reflow of material once the template is removed. This allows the patterned features to retain the same resolution and dimensional fidelity of the original template. The process is also completely additive, eliminating the need for an etching step to remove any residual layer, and can be used to pattern over large areas. Finally, the process is such that many different types of materials can be patterned within the same template in a single

processing step, enabling rapid and low cost creation of complex devices with a limited number of processing steps.

Mathematical modeling and experimental analysis are used to confirm the principles of operation and demonstrate the viability of the manufacturing process. Various nanoparticles including gold, silver, zinc oxide, and iron oxide, and polymers including cellulose acetate, chitosan, poly(methyl methacrylate), poly(vinylidene fluoride), and acrylonitrile butadiene styrene are patterned on various substrates, including silicon, polyimide, and glass. The proposed mechanism of operation is confirmed by comparing experimentally observed nanoparticle fluid flow in the templates to the developed mathematical model.

The template materials, being the critical components of the manufacturing process, are then examined. Two materials, poly(dimethylsiloxane) (PDMS) and poly(4-methyl-2-pentyne) (PMP), are used for creating templates. It is shown that, while PDMS is a simple prototyping material that is easily used to create microscale features, much higher resolutions and faster patterning is possible using PMP. This is due to the higher vapor permeability and Young's modulus of the PMP as compared to the PDMS. Using the PMP templates, a patterning resolution of less than 350 nm is achieved.

Further manufacturing viability is demonstrated by converting the stamp-and-repeat process into a continuous, roll-to-roll process. A simple prototype roller system is created utilizing patterned, vapor permeable PDMS-aramid fiber or PMP-PDMS-aramid fiber composite belts. Using such a system, simple patterns are created having patterning fidelity similar to that obtained with the stamp-and-repeat process.

Finally, two applications of nanoparticles are demonstrated using the proposed manufacturing system. First, low-temperature metallization is performed on a polymer substrate using gold nanoparticles. The particles are patterned and sintered into conductive traces at a temperature of only 220 °C due to the small size and therefore low melting temperature of the particles. Additionally, an ultraviolet light sensor is created using zinc oxide nanoparticles by aligning patterns of the nanoparticles to previously patterned gold electrodes on a silicon dioxide substrate.

Contents

List of Figures

List of Tables

List of Symbols and Abbreviations

Abbreviation	Description	Definition
ABS	Acrylonitrile Butadiene Styrene	page 48
COC	Cyclic Olefin Copolymer	page 41
DMF	Dimethylformamide	page 38
EDX	Energy-Dispersive X-Ray Spectroscopy	page 89
EHD	Electrohydrodynamic	page 16
FT-IR	Fourier Transform Infrared Spectroscopy	page 83
MIMIC	Micromolding in Capillaries	page 23
NMP	n-methylpyrrolidone	page 38
PDMS	Poly(dimethylsiloxane)	page 8
PMMA	Poly(methyl methacrylate)	page 38
PMP	Poly(4-methyl-2-pentyne)	page 29
PTMSDPA	Poly[1-phenyl-2-[p-(trimethylsilyl)phenyl]acetylene]	page 81
PTMSP	Poly(1-trimethylsilyl-1-propyne)	page 81
PVDF	Poly(vinylidene fluoride)	page 38
SAMIM	Solvent Assisted Micromolding	page 25
SEM	Scanning Electron Microscope	page 86
ZnO	Zinc Oxide	page 41
A	Area	page 55
A_m	Constant of Integration Corresponding to the m^{th} Eigenvalue	page 132
A_{mn}	Constant of Integration Corresponding to the m^{th} and n^{th} Eigenvalues	page 144
a_1	Fitting Parameter for Sensor Sensitivity	page 108

Abbreviation	Description	Definition
a_2	Fitting Parameter Accounting for Lensing Effects	page 108
a_3	Fitting Parameter for Sensor Non-Linearity	page 108
b	Square Channel Width	page 66
B_m	Constant of Integration Corresponding to the m^{th} Eigenvalue	page 133
B_{mn}	Constant of Integration Corresponding to the m^{th} and n^{th} Eigenvalues	page 145
C	Three-Dimensional Concentration of Solute	page 57
C_f	Maximum Concentration of Solute	page 61
C_m	Mean Concentration of Solute	page 54
C_{m-ss}	Mean Concentration of Solute in Steady State	page 150
$\bar{C}_m$	Dimensionless Mean Concentration of Solute	page 59
C_0	Reservoir Concentration of Solute	page 55
C_1	Constant of Integration	page 127
C_2	Constant of Integration	page 127
D	Solute Diffusivity	page 55
f_n	n^{th} Coefficient of Series Expansion	page 57
h	Square Channel Height	page 66
$\Delta H_{m,\infty}$	Enthalpy of Fusion of the Bulk Material	page 102
I	Current	page 108
I_0	Maximum Current	page 108
J_n	Bessel Function of the First Kind of Order n	page 132
k_B	Boltzmann Constant	page 55
k_n	Coefficient Relating Time Derivative to n^{th} Spatial Derivative of Concentration	page 57
k_2	Effective Diffusion Constant	page 56
$L(t)$	Channel Length as a Function of Time	page 60
L_f	Filling to Drying Transition Location	page 62
$L_x(t)$	Effective Channel Length	page 63
L_0	Channel Length	page 55
m	Particle Mass	page 160
m_{tot}	Total Mass	page 155
P	Pressure	page 56
$\bar{P}$	Dimensionless Pressure	page 71
P_l	Liquid Phase Pressure	page 159
$P_{m,\infty}$	Melting Pressure for Bulk Material	page 159
P_p	Vapor-Permeable Perimeter	page 55
P_s	Solid Phase Pressure	page 159
P_0	Pressure Scale	page 71

Abbreviation	Description	Definition
P_∞	Atmospheric Pressure	page 161
q"	Evaporation Rate	page 54
R	Cylindrical Duct Radius	page 127
r	Cylindrical Coordinate in Cross Section of Duct	page 127
R_h	Hydraulic Radius	page 66
r_p	Solute Particle or Molecule Radius	page 55
S	Entropy	page 160
s	Specific Entropy	page 160
T	Temperature	page 55
t	Time	page 54
$\bar{t}$	Dimensionless Time	page 59
t_f	Filling to Drying Transition Time	page 62
T_m	Particle Melting Temperature	page 102
$T_{m,\infty}$	Bulk Melting Temperature	page 102
t_s	Time Scale	page 59
$u(\zeta)$	Unit Step Function	page 62
U_{avg}	Average Velocity	page 128
U_m	Characteristic or Maximum Velocity	page 128
u_z	Velocity in the Axial Direction	page 56
V	Particle Volume	page 160
v	Average Velocity	page 54
x	Cartesian Coordinate in Cross Section of Duct	page 136
y	Cartesian Coordinate in Cross Section of Duct	page 136
z	Axial Position	page 54
$\bar{z}$	Dimensionless Axial Position	page 59
α	Aspect Ratio of a Rectangular Channel	page 139
γ_s	Surface Energy of the Solid Phase	page 102
γ_l	Surface Energy of the Liquid Phase	page 102
$\delta(\zeta)$	Dirac Delta Function	page 128
δ_{mn}	Kronecker Delta	page 130
$\epsilon(z)$	A Positive Function	page 58
η	Viscosity	page 55
η_0	Solvent Viscosity	page 71
θ	Cylindrical Coordinate in the Cross Section of the Duct	page 127
λ_m	mth Eigenvalue	page 133
μ_l	Chemical Potential of the Liquid Phase	page 159
μ_m	mth Eigenvalue	page 132
μ_s	Chemical Potential of the Solid Phase	page 159

Abbreviation	Description	Definition
ρ	Particle Density	page 102
τ	Time Constant for Current Decay	page 108
ω	Light Intensity	page 109

Acknowledgements

This work would not have been possible without the various and important contributions of many different people. First, the support and guidance of my adviser, Albert P. Pisano, was invaluable. The advice, discussion, and collaboration of Jim C. Cheng was also extremely important in the success of the research. Practical advice and guidance from Paul Lum in the Biomolecular Nanotechnology Center (BNC) and Mick Franssen and Gordon Long in the Mechanical Engineering Student Machine Shop were very helpful. Discussion and collaboration with Sun Choi, Yegan Erdem, Tim Brackbill, and Trey Cauley were also helpful in the completion of this research. Finally, the discussion, advice and encouragement throughout this research from various members of the Berkeley Micromechanical Analysis and Design (BMAD) Lab were very much appreciated.

Chapter 1

Introduction

Recent years have seen a rapid expansion in the availability and use of portable electronics and sensors. Electronics have become smaller and lighter while incorporating more functionality, while sensors have become smaller and more functional, accurate, and environmentally robust. Continued advancements in the form and function of these devices are likely to continue well into the future. However, the current material set used in sensing and electronics is somewhat limited, with most devices relying on bulk ceramic semiconductor materials. New applications in sensing and electronics, as well as reduction in cost or expansion of functionality or efficiency of existing applications, may be possible using alternative materials such as nanoparticles and polymers. A remaining challenge in the development of devices based on such alternative materials is the creation of the patterns necessary for the desired device. While numerous patterning methods currently exist, no single process has the patterning resolution, fidelity, throughput, and versatility necessary to pattern such a wide range of very different materials in different configurations necessary for a range of diverse applications. However, an understanding of these interesting materials and the currently available patterning processes is critical to the design of a new system for patterning that does satisfy all of the desired patterning metrics.

The current chapter will provide an overview of existing patterning technology for nanoparticles and polymers. It will begin by providing motivation for patterning these materials, highlighting specifically their utility in electronics and sensing applications. A review of the most commonly used and most promising new patterning techniques will follow, along with a detailed discussion of the advantages and disadvantages of these processes. Finally,

a pathway to a new patterning process will be established based on the lessons learned from previous works, which will motivate the current work discussed in subsequent chapters.

While this chapter focuses on reviewing existing patterning technologies, other introductory material and literature review will be contained in subsequent chapters, as the specific topics required are discussed. That is, existing research on vapor permeable polymers will be discussed in Chapter 4, and existing work on the application of nanoparticles in both low temperature metallization and ultraviolet light sensing will be reviewed in Chapter 6.

1.1 Alternative Materials for Electronics and Sensing

Materials are the critical components in electronics and sensing. Bulk semiconductors like silicon, gallium arsenide, or zinc oxide are the current industry standards, and have been researched and applied extensively for these applications. However, there is considerable interest in expanding the current material set beyond these traditional materials, enabling new devices and applications as well as improvements in portability, functionality, efficiently, and cost of existing devices. Specifically, nanoparticles and polymers are promising materials that have unique properties owing to their unique chemistry and structure.

1.1.1 Nanoparticles

Nanoparticles, shown schematically in Figure 1.1(a), have been studied extensively due to their potential uses in electronics and sensing. For crystalline solids, nanoparticles with sizes less than approximately 10 nm can exhibit remarkable differences in physical, optical and electronic properties as compared to bulk materials. These changes are due to the increasing presence of the boundary of the crystal due to the small size of the particle, and can be used in electronics, optics, and sensing applications. However, in addition to size related property changes, the small size and high surface to volume ratio of nanoparticles can also be useful for creating porous materials with a large surface area, amplifying existing surface effects for applications in sensing, thermoelectrics, catalysis, and filtration and separations.

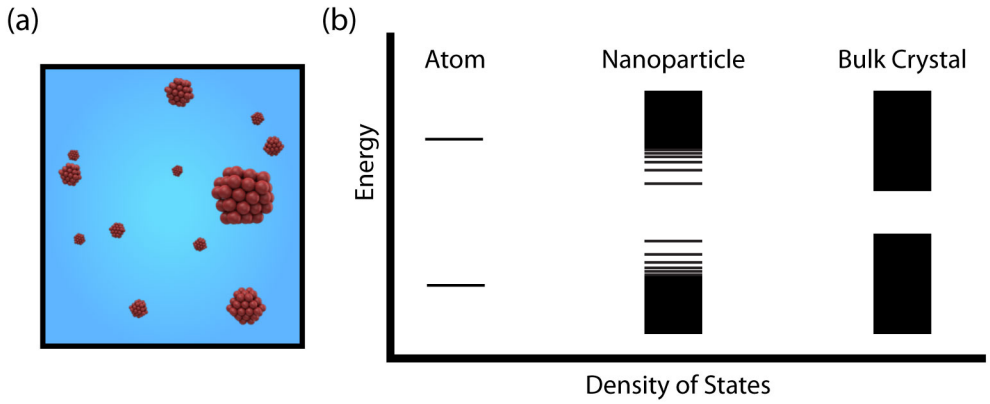

Figure 1.1: (a) Nanoparticles are useful materials due to their small size and high surface to volume ratio. (b) The electronic density of states for nanoparticles lies between those of individual atoms and bulk crystalline materials.

The small size of crystalline nanoparticles is responsible for changes in the optical and electronic properties of these materials as compared to the corresponding bulk materials. The electronic and optical properties are related to the band structure and density of states of the nanomaterial. Since the size of these nanocrystals is between that of atoms or molecules and bulk materials, the density of states is observed to be a hybrid of the discrete density of states seen in atoms or molecules and the continuous bands seen in bulk materials, as shown in Figure 1.1(b). As a crystal decreases in size, the states around the edge of a band gap are affected first, causing a change in the magnitude of the energy gap between conduction and valence bands.[1–3] Such changes in the band structure of nanoparticles have a profound effect on semiconducting materials because the Fermi level lies within the band gap, allowing changes in the density of states and the size of the band gap to strongly influence electronic properties. For metallic particles, the Fermi level exists near the center of a band and therefore such discretization has only a modest effect that is seen only at extremely small size scales. However, when these metallic particles are exposed to light, collective oscillation of free electrons in the electron gas of the conduction band results from the small size of the particle relative to the wavelength of incident light, enabling a well-defined surface plasmon absorption.[4] These changes in electronic and optical properties of both semiconducting and metallic nanoparticles can be used in the creation of novel optics, electronics, and sensors.[5]

In addition to changes in the electronic and optical properties, the high

surface to volume ratio of the nanoparticle can also cause changes in the physical properties of the crystalline material. The surface of a material has many unoccupied binding sites, known as coordinative unsaturation, which causes the material to have a very high surface energy. Due to the relatively large number of atoms at the surface of the nanoparticle, there is a significant contribution from the surface to the total energy of the solid particle. As a result, it can become energetically favorable for a solid crystal to transition its phase to a liquid, in order to minimize surface area, at temperatures well below that of the corresponding melting temperature of the bulk material.[1] In a similar manner, the high surface to volume ratio can lead to changes in the solid-solid phase transitions of a material.[6] The changes in physical properties can be useful in low temperature material processing or exploitation of material properties present in a phase not normally stable at the given thermodynamic conditions.[6,7]

Finally, the high surface to volume ratio of nanoparticles can be used to amplify surface effects that are already present in the equivalent bulk materials. Creation of a highly porous material with a very large surface area can be accomplished using agglomerations of nanoparticles, which can be useful for catalysis,[8] filtration and separations,[9] or creation of optical or chemical sensors that rely on surface chemistry for proper operation.[10,11]

1.1.2 Polymers

Polymers, shown schematically in Figure 1.2(a), are large molecules that consist of repeating structural units. The chemical composition of these repeating units determine the electronic, physical, and chemical properties of the polymer, which can be useful in electronic, structural and sensing applications. Due to the long length of the polymer chains and the corresponding difficulty in packing these materials into crystalline structures, polymers have a largely amorphous form. Additionally, the existence of a glass transition temperature at which the material softens and the ability to dissolve these materials in certain solvents allows for simple and low-cost processing.

A specific class of polymers that are particularly useful for electronics and sensing applications are known as conjugated polymers. These materials, such as the poly(aniline) shown in Figure 1.2(b), have alternating single and double bonds in the backbone of the polymer chain.[12] The alternating bonds allows for a continuous chain of carbon atoms with sp^2 hybridization. Here, the p_x and p_y orbitals hybridize with the s orbital, and the remaining

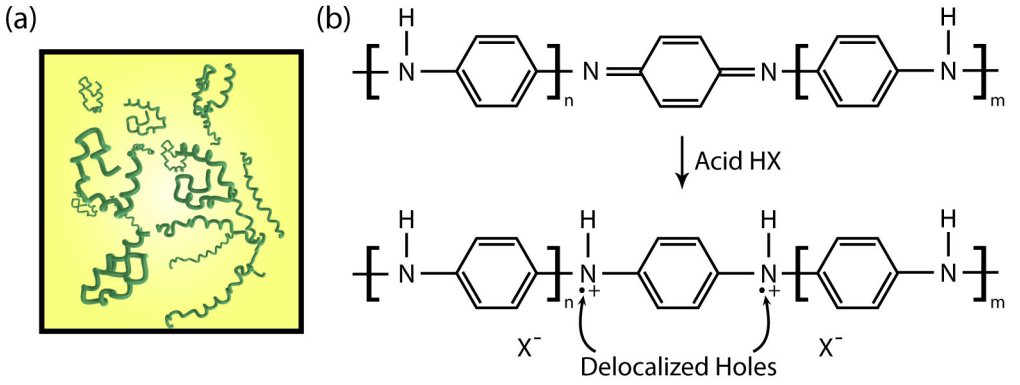

Figure 1.2: (a) Polymers are useful materials due to the many different chemical compositions attainable. (b) Certain conjugated polymers, which contains alternating single and double bonds in the backbone, can be made conductive by doping. Here, the emeraldine base form of poly(aniline) is doped using an acid to introduce delocalized holes, creating the conductive emeraldine salt form of the polymer.

p_z orbitals overlap, forming a continuous, connected conduction pathway. The remaining electron from each atom not involved in the formation of the covalent bonds is then delocalized, existing in the continuous overlapping p_z orbital as a free conduction electron. However, the overlap in the p_z orbitals leads to the formation of two molecular orbitals at distinct energy levels, of which one is completely empty and the other completely full.[13] The resulting polymer remains non-conductive until electrons are either added to the lowest unoccupied molecular orbital or removed from the highest occupied molecular orbital. This process, known as doping, is performed by chemically oxidizing or reducing the polymer, which adds or subtracts mobile electrons. By doping the polymer, the conductivity can be controllably adjusted over several orders of magnitude, similar to traditional semiconductor materials like silicon or gallium arsenide.[14] This class of polymers is therefore useful in the creation of various electronic devices, including electronic interconnects,[15] transistors,[16] light emitting diodes,[17] sensors,[18] and actuators.[19]

While conjugated polymers are of particular importance to electronics applications, other polymers can also be useful in the creation of electronic components, sensors or structural layers. Interaction of chemicals with side groups on the polymer chain together with the weak van der Waals bonding between separate polymer chains allows the polymer to swell in response to chemicals, with different chemicals interacting with various polymers in

different ways. This interaction can cause changes in the structural or dielectric properties of the polymer, which can be used for sensing applications.[20,21] The low processing cost of polymers also make them useful as structural or encapsulation materials,[22] dielectrics,[23] or as surface treatments for modification of wetability properties.[24]

1.2 Patterning Metrics for Nanoparticles and Polymers

Realization of useful applications of nanoparticles and polymers in electronics and sensing is dependent on an ability to pattern these materials in a manner that enables proper placement of the required materials in the proper configuration on an appropriate substrate. While the desired application must be known in order to properly evaluate any given patterning process, these processes can still be discussed in an abstract sense. To do this, a set of patterning metrics is necessary by which the various processes may be compared. These metrics are motivated by some of the most commonly seen patterning requirements from targeted applications in electronics and sensing. They are:

1. **The patterning process should be versatile.** The large variation in the chemical structures and physical properties of the materials and substrates involved in the creation of practical electronics and sensing applications necessitates that a given process be able to pattern a variety of materials with sometimes very dissimilar properties without the need for significant development effort. Therefore, the requirements on the materials or inks involved in the patterning must be minimal. Additionally, any material-specific processing steps should be eliminated. It is noted that each material requires a different etching process, and thus elimination of any material removal steps greatly extends the versatility of the designed process. A completely additive process not only eliminates the need for any such etching step, but also reduces material waste, which for some more exotic materials can lead to substantial cost savings.

2. **The patterning process should result in high quality pattern transfer.** The structure of patterned features is of critical importance to many applications, and therefore suitable pattern transfer is required. The most commonly used metric for pattern transfer is the

attainable resolution of the process, measured as minimum attainable width of a patterned line. Such resolution is important for applications in electronics and sensing as, for example, the dimensions of patterned features on a transistor are related to operating speed and power consumption[25] and on some sensor components are related to the surface to volume ratio and thus the sensitivity to a target analyte.[26] However, in addition to the minimum line width, other factors are also important in measuring the quality of pattern transfer. For example, the ability to accurately place features relative to one another, to achieve the designed dimensions, and to minimize variation in the width of lines, termed here as patterning fidelity, is critical to reliable and repeatable production of devices. The ability to accurately control the three-dimensional structure of patterned features, including the straightness of sidewalls and the ability to achieve designed feature heights with a minimum of variation, is also important for ensuring uniform electronic, sensing, and structural properties along the length of patterned features.

3. **The patterning process should be able to align subsequent layers of features.** For creation of practical devices, patterning more than one material or more than one layer is often necessary. Therefore, the ability to easily and accurately align one layer with respect to a previous layer is critical for rapid and efficient device creation.

4. **The patterning process should have sufficiently high throughput.** For application in an industrial manufacturing setting, a process which is able to pattern at high throughput and over large areas is desired. This is aided by rapid completion of a minimum number of simple processing steps.

1.3 Patterning Methods for Nanoparticles and Polymers: An Overview

Numerous processes exist for patterning nanoparticles and polymers. As shown in Figure 1.3, these processes can be broadly classified according to the different methods used to create the patterns. Most generally, these patterning processes can be broadly classified into two groups: traditional and alternative. The traditional processes are defined as those that use

photolithography as the primary means of creating the pattern, whether directly or indirectly. This includes direct photolithography, lift-off, and thin film deposition and etching processes. The alternative patterning processes are those that do not use photolithography at any point in the patterning, other than perhaps for creation of the necessary reusable templates. These alternative techniques can themselves be broadly classified into two groups: inkjet based and template based. Inkjet based methods, which include inkjet printing, electrohydrodynamic jet printing, and electrospinning, pattern ink directly on the substrate without the use of any predefined template. In contrast, the template-based methods use a physical template to confine ink to certain pre-defined regions on the substrate and exclude ink from other regions. These processes include gravure printing, screen printing, nanoimprint lithography, micromolding in capillaries, solvent assisted micromolding, and solvent absorption micromolding. The template-based methods can be further divided into two subgroups depending on the material used for the template: rigid and soft templates. The rigid template methods use ceramics, metals, and rigid polymers for patterning the ink, while the soft template methods all use poly(dimethylsiloxane) (PDMS). The difference in rigidity is often associated with differences in absolute positional accuracy, template lifetimes, and management of existing surface topology and defects. However, an additional and often overlooked distinction between the two classes of template materials is the vapor permeability, with the PDMS templates having a much higher vapor permeability than the rigid templates. This remarkable difference in vapor permeability that exists between the two classes of templates is related to the ability to change the rheology of ink while inside the template by solvent depletion, enabling higher patterning fidelity without requiring a change in the chemical composition of the ink.

1.4 A Review of Traditional Patterning Methods

Traditional patterning methods are defined as those that rely on photolithography as the primary means of patterning materials. These processes are commonly used in the microfabrication industry, and as such have benefited from many years of continuous research and development. It is therefore attractive to attempt to use such processes, or variations thereof, for patterning nanoparticles and polymers. For example, the material of

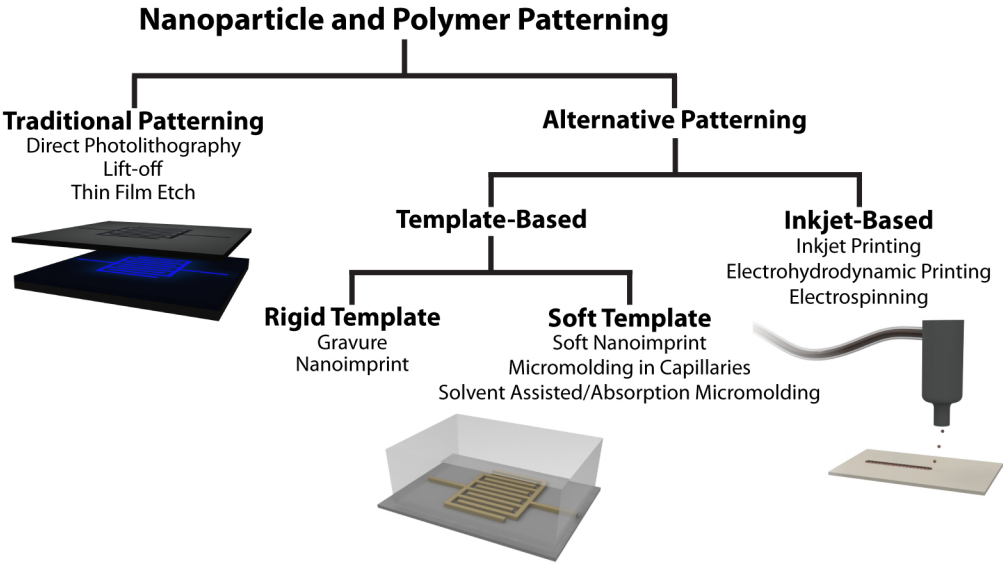

Figure 1.3: A classification of common processes for patterning nanoparticles and polymers.

interest can either be patterned by direct photolithography, by formation of a resist template by photolithography followed by material deposition and lift-off, or by deposition of a thin film of material followed by resist deposition, photolithography, and etching of the material. However, as will be discussed in the following sections, such traditional patterning processes are compatible with only a limited set of materials, and are thus lacking in the versatility required for manufacturing practical devices from nanoparticle and polymer materials.

1.4.1 Direct Photolithography

Photolithography, shown schematically in Figure 1.4, is the primary method by which patterns are formed in all traditional microfabrication processes. Direct photolithography refers to the process wherein the material to be patterned contains a photosensitive component, allowing chemical differentiation between exposed and unexposed regions.

When photolithography is used in traditional microfabrication, a polymer with a photosensitive chemical is spread on a substrate using spin-coating. When exposed to light or electrons of sufficient energy, the solubility of the polymer changes, allowing differentiation of those areas exposed to light from those left unexposed. The exposure to light causes either a photoacid generator to make the exposed regions more soluble as

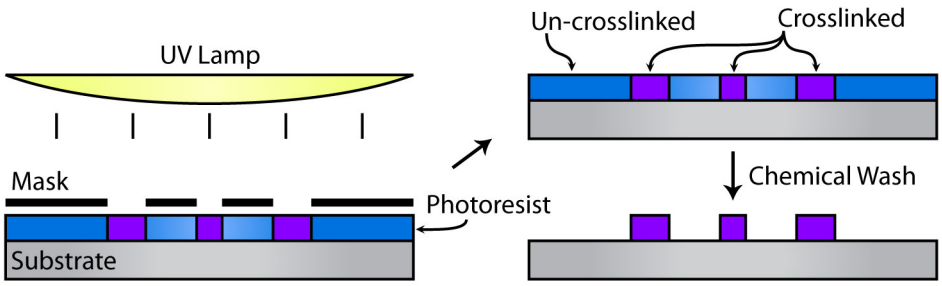

Figure 1.4: In the direct photolithography process, the material of interest contains a photoactive material which, when exposed to ultraviolet light, changes the solubility of the material in a chemical developer. As shown, the photoresist contains a UV activated crosslinker, which makes the material insoluble with respect to the uncrosslinked material.

compared to unexposed regions (positive photoresist), or causes a photoactivated crosslinker to make the exposed region insoluble as compared to unexposed regions (negative photoresist). Following exposure, the photoresist is selectively removed from the substrate using a chemical developer. In the case of light as the patterning initiator, the image is formed in the polymer by selectively allowing or blocking the light reaching the photosensitive polymer, using a mask containing the image of the features to be created. This mask is either placed in direct contact or close proximity to the polymer, or in front of projecting optics to reduce the size of features. In the case of electrons, the patterns may be written directly on the substrate without the use of any predefined mask.[27]

Photolithography has been used extensively to create patterns of various polymers on a range of substrates in microfabrication process flows. Resolution of smaller than 50 nm is possible using either high frequency ultraviolet light or electron beams to expose the photoresist. Features of larger size are also possible using much simpler contact, proximity, and projection lithography.[27] The created features are of high quality, with straight edges and controllable heights and with precise control over position of features. However, not all polymers are compatible with this process, as a photoinitiated chemical change is required. When such a chemical can be found, use of chemical crosslinkers or photoacids can change the properties of the patterned polymer in a manner that may be undesirable to the operation of the final device.

In addition to polymers, nanoparticles can also be patterned using direct photolithography. However, the necessity of having a photochemical

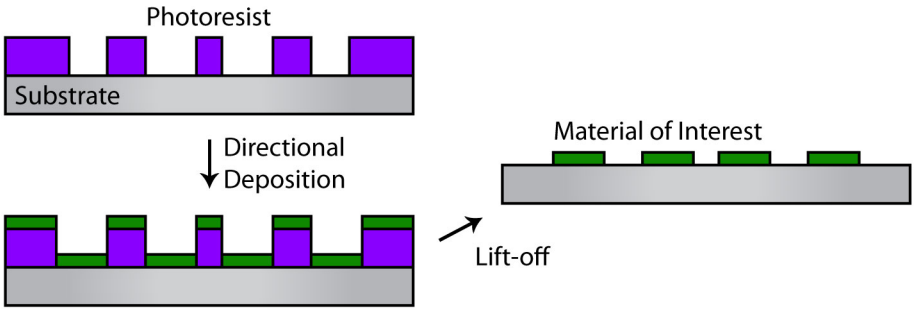

Figure 1.5: In a lift-off process, a photoresist template is created on the substrate, after which the material of interest is deposited such that a separation exists between material on the substrate and on the photoresist template. The photoresist template is then removed using a chemical etch, leaving only patterns of the material of interest.

response to differentiate the exposed and unexposed regions complicates the process. For nanoparticles, this can be done by incorporating a polymer binder with photoactivated crosslinker[28,29] or by coating the nanoparticles with a ligand which can be removed by exposure to incident radiation.[30] The results of the patterning are similar to that attainable by photolithography with polymers discussed above, offering high resolution with excellent pattern definition.[28] However, the polymer additives can be difficult to remove and can adversely affect the performance of the patterned material, again limiting the versatility of the process.[31]

1.4.2 Lift-off Processes

Lift-off processes are commonly used in the microfabrication industry for patterning materials that are difficult to etch. In this process, shown schematically in Figure 1.5, a photoresist is spin-coated on the wafer, exposed, and developed to form the negative of the desired patterns. The material to be patterned is then deposited uniformly over the substrate and photoresist in a directional manner, such that the material deposited on top of the photoresist is physically separated from the material deposited on the substrate. The photoresist is then stripped using chemical dissolution, carrying away the excess deposited material and leaving only the desired patterns of material on the substrate.[27]

Nanoparticles can be patterned using this process by depositing them uniformly on the substrate using spin-coating,[32] evaporation of a sessile droplet of nanoparticle ink,[33] or other similar processes. Using the correct

concentration of nanoparticles in an appropriate solvent, particles can be deposited into the voids in the photoresist template without connection to the residual layer of particles on top of the photoresist.[34] After deposition, the photoresist is stripped using a chemical etch, which must completely remove the photoresist without harming the patterned nanoparticle features or allowing redeposition of particles on the substrate. This requirement is not easily fulfilled, and limits the applicability of this process to only a small set of materials.

Polymers can also be patterned using a lift-off process. However, the method of depositing the polymer to ensure a separation between the material on the substrate and the residual material lifted off upon removal of the photoresist template complicates the process. This can be done using, for example, bottom-up assembly of polymers in the templates prior to lift-off[35,36] or spin-coating on a template with etched holes that are much deeper than the height of the features being produced.[37]

1.4.3 Thin Film Deposition and Etching

Thin film deposition and etching is one of the most commonly used methods of patterning materials in the microfabrication industry. In this process, shown schematically in Figure 1.6, a thin film of material is deposited uniformly over the entire substrate using one of a number of different processes. Photoresist is then spin-coated on top of the deposited material, exposed, and developed to form the positive image of the desired pattern, leaving the material to be removed exposed on the substrate. A material-specific etch is then used to remove the exposed part of the previously deposited thin film. Following etching, the photoresist is stripped, leaving the patterned material on the substrate.[27]

Nanoparticles and polymers can be patterned using thin film deposition and etching.[38,39] The material is typically deposited using spin-coating of the material dissolved or dispersed in solvent, and etched using either wet chemistry or dry etching processes. While this standard process allows for formation of high-quality patterns with high throughput, the process is restricted by its limited versatility. Each material requires its own etching recipe, which must remove the material of interest without removing the photoresist mask. Ideally, the etch should be sufficiently anisotropic to prevent etching of material from under the photoresist. Once the etching is complete, the photoresist must be stripped without harming the material of interest. These chemical processes must all occur without modifying any

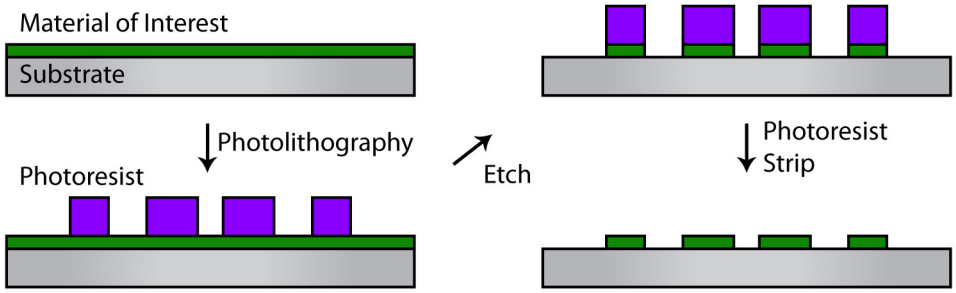

Figure 1.6: In a thin-film etching process, the material of interest is deposited uniformly across the entire substrate. A photoresist etch mask is then created, after which the material of interest is etched. The photoresist is then stripped, leaving the desired patterns of the material of interest.

of the chemical properties of the patterned material to prevent appearance of any adverse effects in the ultimate application of the patterned material.[37] These restrictions limit the use of this process to only a small set of materials.

1.5 A Review of Non-Traditional Patterning Methods

Non-traditional patterning methods are defined as those that do not use photolithography as the primary means of creating the patterns, other than perhaps in the creation of reusable templates, and as such are not commonly used in the microfabrication industry. The development of these alternative processes is motivated by the lack of versatility with respect to the specific material when patterning nanoparticles and polymers using traditional patterning methods. These alternative processes can be broadly classified into two groups: those that pattern without the use of a physical template, and those that use a physical template. The template-less processes create patterns by spraying ink on the substrate in selective locations, and include inkjet printing, electrospinning, and electrohydrodynamic jet printing. These methods feature patterning with no residual layer and therefore no chemical etching, which allows for increased versatility with respect to the materials being patterned. However, the spraying process is inherently complex, has low patterning quality in terms of either patterning resolution or fidelity, and has low throughput. In contrast, the template-based methods, which include gravure printing, screen printing, nanoimprint lithogra-

phy, micromolding in capillaries, solvent assisted micromolding, and solvent absorption micromolding, use a physical template to confine ink into patterns on a template. This template provides a physical boundary which controls the interaction between the ink and the substrate, simplifying the fluid handling. However, the presence of a physical template provides a challenge for changing the ink from a liquid to a solid since, unlike the template-less methods, solvent in the ink cannot simply evaporate directly into the environment. Such changes in ink rheology can be obtained by, for example, thermally induced phase change, UV or thermally activated crosslinkers, or solvent absorption or evaporation through vapor permeable templates. Any incomplete solidification of the ink can result in low patterning quality due to reflow of the ink on the substrate once the template is removed.

1.5.1 Inkjet Patterning

Inkjet patterning, illustrated schematically in Figure 1.7(a), is the most well-established and popular of the non-traditional methods for patterning polymers and nanoparticles. In this process, ink droplets are ejected from a nozzle and directed at a substrate to form a large number of discrete dots which, in aggregate, create a pattern. The first known inkjet patterning process was developed as early as 1858 by William Thomson (Lord Kelvin), using electrostatic deflection of a stream of droplets as a means of recording telegraph messages automatically.[40] In the 1950s, inkjet technology developed more rapidly, culminating in the large number of commercial inkjet printers that are available today.[40] The process is attractive for patterning nanoparticles and polymers because, as a completely additive process, there is no need for any material-specific etching, allowing the process to be used with a wide variety of materials.

Inkjet print nozzles can be classified into continuous and drop-on-demand systems. In a continuous system, a stream of fluid is ejected from a nozzle, which then breaks up into droplets by means of a Rayleigh-Plateau instability. Electrostatic charge is selectively applied to the droplets, which are either directed at the substrate to form a pattern, or into a gutter for collection and re-use.[41] In a drop-on-demand system, droplets of fluid are ejected from a nozzle individually, using a pressure pulse to overcome surface tension at the fluid-air interface and cause a droplet of fluid to be ejected. In modern printers, the most common means of creating the pressure pulse is by either thermal or piezoelectric actuation.[42] Thermal actuation is per-

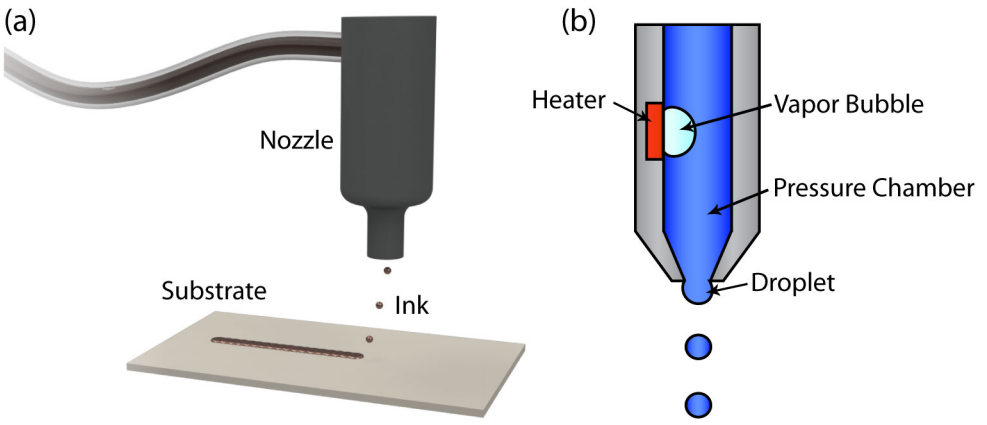

Figure 1.7: (a) Inkjet printing uses the controlled ejection of droplets from a nozzle to pattern material suspended in a fluid. (b) A thermal inkjet printer uses a small heater to create a vapor bubble in the ink, displacing fluid and ejecting ink from the nozzle toward the substrate.

formed by creating a small vapor bubble in the ink, which displaces liquid and creates the necessary pressure pulse, as shown in Figure 1.7(b). The formation of the vapor bubble forces the ink out from the nozzle, and the collapse of the vapor bubble pinches off the droplet and creates a negative pressure in the nozzle which drives the flow of additional ink into the reservoir. The entire droplet ejection process and the refilling of the nozzle can be completed in a time scale on the order of approximately 100 μs, with the limitation being due to the refill of the nozzle with ink rather than the droplet ejection speed.[41] Piezoelectric actuation is performed using the deformation of a piezoelectric crystal to create the required pressure pulse.[42] The fluidics of the ink ejection are the same as in the thermally actuated nozzle, except that the deformation of a piezoelectric crystal rather than a vapor bubble drives the fluid ejection and refill of the nozzle with ink. The time scale for piezoelectric actuation is similar to that of the thermal actuation due to the refill of the nozzle with ink being the rate limiting step.[41]

Patterning of both polymers and nanoparticles have been demonstrated extensively using inkjet printing, and many practical devices have been created from these materials. For example, polymers have been patterned by inkjet printing for applications in organic light-emitting diodes (OLEDs),[43,44] organic transistors,[45] organic photovoltaics,[46] biosensors[47] and chemical sensors,[21,48] while nanoparticles have been patterned for use in low-temperature metalization,[49] transistors,[50] photosensors,[51] chemical

sensors,[52] and biosensors.[53] However, despite the widespread use of inkjet printing for patterning these materials for such a wide variety of applications, there are numerous disadvantages of this process. First, there is a very high dependence on the fluidic properties of the ink, which must be precisely controlled for proper operation. For example, the viscosity and surface tension of the ink are important for proper droplet ejection and for creation of the necessary pressure forces and fluid motion to refill the nozzle with ink in a sufficiently short time scale. The volatility of the solvent together with the viscosity of the ink determine how the ink reflows on the substrate as it dries, which is important for satisfactory patterning resolution and fidelity. The volatility of the solvent and the surface tension and stability of the ink suspension determine the long-term stability of the system as the solute must not agglomerate in the nozzle and thus interfere with droplet formation or fluid refill. Much effort is therefore expended on engineering the properties of the ink, which includes use of various solvents, stabilizers, surfactants, binders, and crosslinkers in the ink.[42] As a result, the process becomes highly dependent on the material being patterned, reducing versatility of the process. Additionally, the use of a nozzle to eject individual droplets severely limits the throughput of the process, although throughput can be increased by utilizing an array of inkjet nozzles in parallel.[54] The resulting patterned features are typically thin films, with additional height obtained by patterning multiple times over the same area allowing higher aspect ratios of as much as 1:10.[55] The height of patterned features is ultimately limited by the stability of the fluid on the substrate, allowing only limited control over three dimensional geometry.[42] Even with properly engineered ink, patterned features often have wavy edges and slanted sidewalls due to incomplete coalescence of ink, instability of the fluid film, or surface tension interactions between the liquid ink on the substrate.[42] Finally, the resolution of the patterned features is limited by the ability to create sufficiently small droplets and by variations in the flight path of droplets between the nozzle and the substrate, with modern printers only able to create line widths of approximately 20 μm.[56]

1.5.2 Electrohydrodynamic (EHD) Printing and Electrospinning

Liquid flows driven by electric fields have been studied extensively over the course of many years.[57] A practical application of this, known as electrospinning, was created in 1902[58,59] and has been used extensively to create

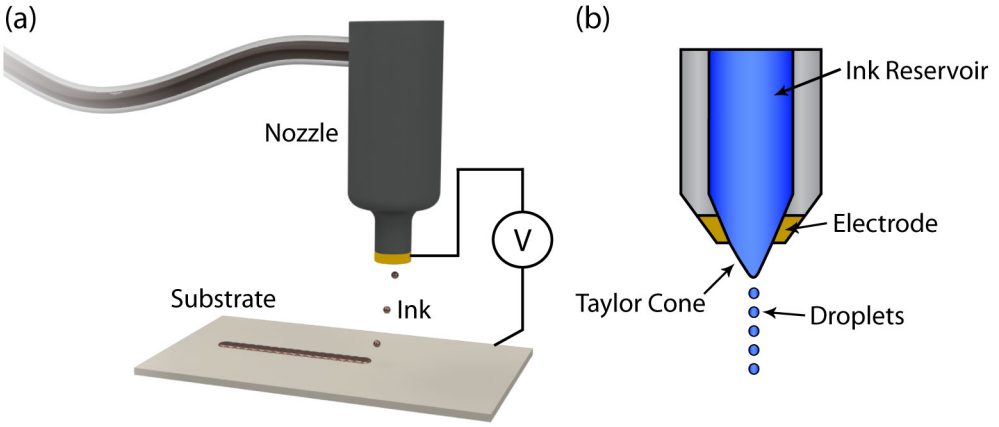

Figure 1.8: (a) Electrohydrodynamic jet printing uses an electric potential to eject droplets from a nozzle. (b) The electric field causes the fluid to form a Taylor cone at the end of the nozzle which, at sufficiently high voltages, becomes unstable and ejects fluid with a droplet or stream diameter that is much smaller than the nozzle diameter.

polymer wires with nanoscale dimensions for applications in catalysis, filtration, tissue scaffolding, electronics and sensing.[60] However, only recently has the principle of an electrically driven flow been considered for use as a replacement for the technology used in drop-on-demand inkjet printing.[61] Through the use of the electrohydrodynamic fluid flow, a controllable stream of either continuous fluid or of droplets with very small diameter may be created, allowing patterning of material in a manner similar to inkjet printing but with substantially higher resolution.[61]

A schematic of this process is shown in Figure 1.8(a). When a sufficiently high voltage is applied across a fluid interface, the bulk of the fluid will begin to carry a charge or, in certain ink formulations, the applied potential can cause mobile ions in the fluid to accumulate at the surface.[61,62] This charge causes a repulsive force in the fluid as a result of Coulombic interactions which, at a fluid-air interface, is counteracted by surface tension. As a result, this balance of forces is observed to distort a normally spherical meniscus into a Taylor cone, as illustrated in Figure 1.8(b).[62] At sufficiently high voltages, the repulsive force in the fluid can overcome the surface tension forces and cause a fluid-air interface to become unstable. The ejection of fluid from the Taylor cone results in either a continuous jet or a stream of discreet droplets with a characteristic dimension that is much smaller than the diameter of the nozzle from which the fluid is ejected.

Both electrospinning and electrohydrodynamic jet printing use the same

principle of operation, with only subtle differences. Electrospinning uses a continuous jet of liquid formed by the charge in the body of the fluid caused by the application of a voltage.[62,63] Electrohydrodynamic jet printing uses either a continuous jet or a stream of discreet droplets formed by the influence of the applied voltage on mobile ions in the fluid.[61]

Both nanoparticles and polymers have been successfully patterned using these processes.[61,63,64] Similar to inkjet printing, the deposition process is completely additive, eliminating the need for material removal by etching following the deposition. However, unlike inkjet patterning, the use of electrohydrodynamic flows allows for creation of fluid jets of much smaller diameter and droplets of much smaller volume than is attainable using an inkjet nozzle. The smaller volume of fluid allows for patterning at higher resolution, with current patterning able to create features with a minimum line width of less than 300 nm.[61–63] However, accurate positioning the features accurately on the substrate is challenging. Statistical variations in the flight path of droplets as well as charge accumulation and Coulombic repulsion of fluid streams can lead to inaccuracies in the position of features, causing wavy lines or incorrect pitch.[56,63] The result is a variation in the placement on lines which, for the highest resolution lines, can vary by more than 100% of the width of the line.[61–63] Additionally, the size and morphology of patterned features is highly dependent on the rheological and electrostatic properties of the ink, and any modification or variation in those properties would require a corresponding variation in patterning parameters. Precise control over the shape of the cross section of the patterned features is not possible, as features will either maintain the shape of the jet or the droplet agglomerations on the surface, or be heavily influenced by the reflow of ink on the substrate. Finally, the throughput of the process is low as a result of writing individual features sequentially, discouraging application of this method in a manufacturing setting.

1.5.3 Gravure Printing

Gravure printing is a continuous and high throughput process that is capable of creating patterns over large areas. As such, gravure printing has seen considerable commercial success in rapid reproduction of graphic designs in the production of newspapers, magazines, currency, packaging, wall paper, as well as many other applications where high volume reproduction of a graphic design is needed. Recently, this well-established process has been explored for patterning nanoparticles and polymers for a variety of

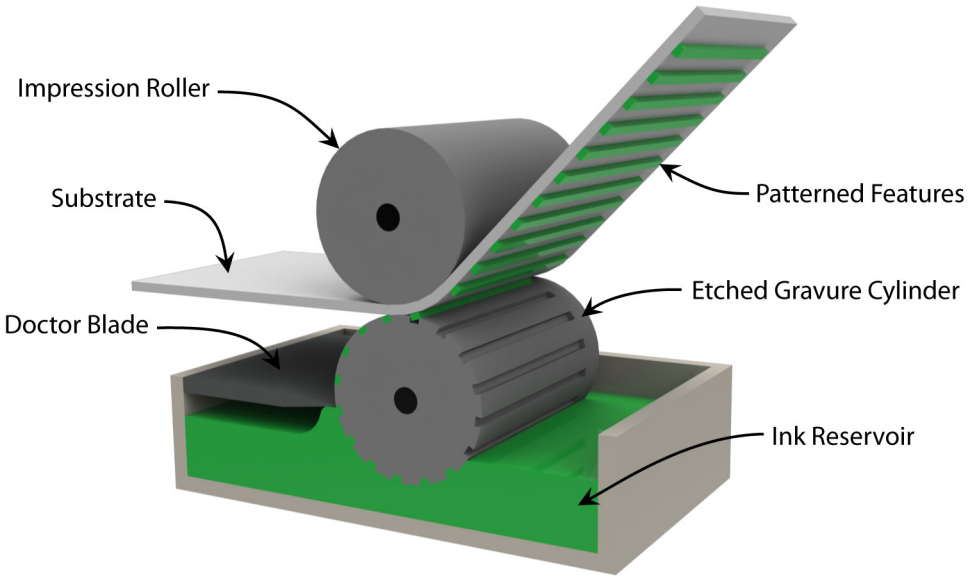

Figure 1.9: In the gravure process, an etched gravure cylinder is rolled through an ink reservoir, filling the recessed features. Residual ink is removed using a doctor blade, and the gravure cylinder is pressed against the substrate with assistance from the impression cylinder. Once the ink is transferred to the substrate, the substrate is removed from the gravure cylinder.

electronic applications.

A schematic of the process is shown in Figure 1.9. A cylinder with etched patterns is rolled through a reservoir of ink. The patterns on the etched cylinder can be either a series of discrete wells or continuous "intaglio" trenches. Following filling, a doctor blade is used to remove excess ink from the cylinder, ensuring that only the etched wells are filled with ink and the rest of the cylinder is free from any residual fluid. The ink is then either transferred to the substrate or to an intermediate offset roller and then onto the substrate by direct contact. Following transfer of ink, the fluid reflows on the substrate, allowing discrete features with sufficiently close spacing to flow together and form continuous lines, and then solidifies by evaporation of the ink's solvent into the environment.[65]

Nanoparticles and polymers have been successfully patterned using this process for a few basic applications, including eletrical interconnects,[66] antennas,[67] and organic thin film transistors.[68] High quality patterning with these materials is dependent on the precision of the gravure roller, the fluidic properties of the ink, and the interaction between the ink and the substrate.

The ink must fill completely into the features during coating so as to ensure that the proper volume of fluid is transferred to the substrate, which determines the ultimate size and morphology of the patterned features. Removal of the excess ink by the doctor blade ensures a lack of residual layer of material on the surface and eliminates the need for material-specific etching processes, but must occur without inadvertently removing the ink from the wells of the gravure cylinder. Finally, the reflow of ink on the substrate determines the ultimate shape of the patterned features. The extent of the reflow is determined by the evaporation rate of the solvent, the fluidic properties of the ink suspension, and the interactions between the fluid and the substrate as well as between adjacent fluid droplets. While this reflow can be used to join discrete points on a surface to form continuous lines, the reflow ultimately limits resolution, with the minimum line width of features being approximately 20 μm.[69,70] Improper reflow can also create incomplete joining of adjacent droplets of ink or cause instabilities to form in lines, causing wavy edges or variations in line width along the length of the line.[70] Finally, three-dimensional patterns are not possible due to this reflow of ink on the substrate, allowing only patterns with very low aspect ratios of at most 1:4.[68]

1.5.4 Screen Printing

Screen printing, illustrated in Figure 1.10, is a simple method for patterning various materials on substrates that has been used for many years for rapid and low-cost reproduction of graphic designs. A woven mesh is used to support a stencil which selectively blocks ink. The mesh is positioned above the substrate, ink is applied, and mechanical force from a squeegee is used to press the mesh into the substrate. This brief contact between the mesh and the substrate transfers ink in the regions not blocked by the stencil. The ink is then dried by evaporation, leaving the patterned material of interest on the substrate.[71]

Both nanoparticles and polymers have been patterning using screen printing, and a variety of practical devices have been created. With polymers, conjugated polymer electrodes,[72] organic field effect transistors,[73] organic light emitting diodes,[74] and solar cells[75], and with nanoparticles, gas sensors,[76] electrodes,[75] solar cells,[75] and field effect transistors[77] have all been successfully created. The process is simple, creates patterns over large area, and has high throughput. However, the patterning resolution is limited to a minimum line width of approximately 100 μm due to the reflow

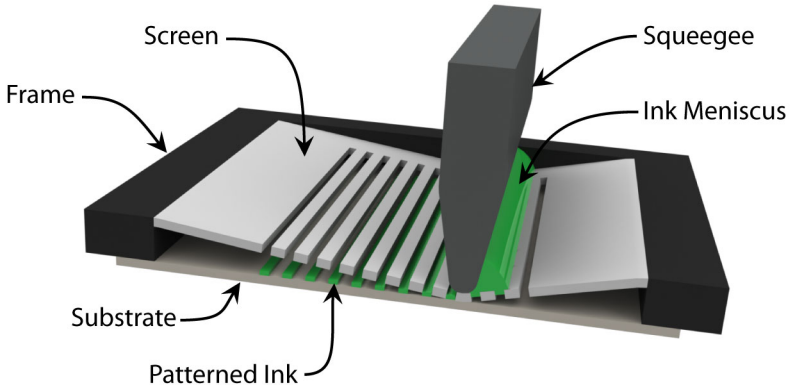

Figure 1.10: In the screen printing process, an ink is spread over a stencil which is supported on a woven mesh, which is then forced into brief contact with the substrate using a squeegee. Ink is transferred from the mesh to the substrate only in areas not blocked by the stencil.

of ink on the substrate after the mesh detaches and while the solvent in the ink dries.[78] The patterns have very low aspect ratio, typically less than 1:4, and lack a physical boundary for the ink which prevents formation of three-dimensional patterns.[79]

1.5.5 Nanoimprint Lithography (NIL)

Nanoimprint lithography, shown schematically in Figure 1.11, was originally developed as a low cost alternative to the expensive photolithographic processes for creation of features with sub-50 nm dimensions. Since its introduction in 1995,[80] research in nanoimprint lithography has produced several robust and sophisticated tools which can create patterns with extremely high resolution over large areas with high throughput.[81] In this process, a layer of material to be patterned is deposited on the substrate by spin-coating. This material is either a liquid polymer containing a UV or thermal activated crosslinker, or a thermoplastic polymer which is raised above its glass transition temperature prior to patterning. A patterned template is then pressed into the material, causing it to flow into the template features. This template is typically made from either silicon or PDMS, and the resulting patterning processes are termed hard and soft nanoimprint lithography, respectively. The material is then hardened using either a UV light activated crosslinker (UV-NIL), or by lowering the temperature to solidify the liquefied thermoplastic polymer (thermal NIL).[82] The template is then removed, leaving the patterned features with a thin layer of residual

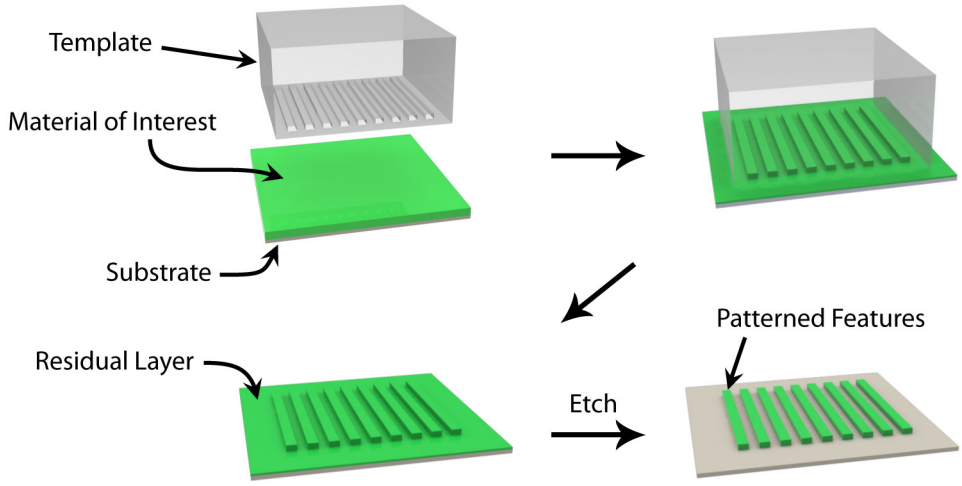

Figure 1.11: In the nanoimprint lithography process, a substrate is coated with a material of interest and patterned by pressing with a template. Once the ink is solidified, the template is removed, leaving the material of interest as well as a residual layer. The residual layer is typically then etched away, leaving only the patterned features.

polymer between them. This residual layer is typically etched away using plasma or chemical etching before subsequent processing steps.[83]

Since it was developed as a replacement for photolithography, nanoimprint lithography was originally created for use with polymers. As such, many different types of polymers have been patterned using this method, including both thermoplastic and thermoset polymers. Applications include creation of masking layers for subsequent pattern transfer[83], organic field effect transistors,[84] optical components,[85] scaffolding for biomolecules,[86] and even patterning of compact disks and digital video disks.[87] The resulting patterns have high resolution with line widths below 50 nm and are patterned at high throughput. The patterns have high quality, including straight edges and precise placement relative to adjacent features,[82] and can have high aspect ratios of as much as 10:1.[88] However, the presence of a residual layer can prove problematic, as this layer must be removed in an etch process that varies based on the specific material. Additionally, for uniform features, the patterning must be done in a manner that produces a uniform residual layer, ensuring that features have uniform and predictable height over the entire patterned area when the etching process is complete.[89] Finally, precise placement of features can be difficult due to deformation of the mold, especially considering the high pressures required

to drive a highly viscous polymer in a squeeze-film type flow.[90]

While use of nanoimprint lithography is intuitive for use with polymers, patterning nanoparticles is more challenging on account of the difficulty of changing the rheology of the nanoparticle ink while the template is in place on the substrate. However, despite this limitation, nanoparticles have been patterned with this process for applications in metallization for transistors and electrodes on flexible electronics.[7,91] When nanoparticle inks are patterned using this process, the template is invariably made from PDMS. Although the reason for use of this material is not stated explicitly in the literature, PDMS is a highly vapor permeable polymer which allows the nanoparticle ink to solidify by solvent evaporation and diffusion through the nanoimprint template itself. The process is, therefore, essentially the same as for solvent absorption micromolding, which will be discussed in a subsequent section. The patterns created using this process with nanoparticles have very high resolution, with line widths smaller than 100 nm. The patterns are of high quality with smooth and straight sidewalls. However, there is a residual layer which must be removed in an etching process which, given the high variability of materials being patterned, requires very different etching chemistries for each material patterned. This residual layer is often non-uniform, due to the low Young's modulus of the PDMS template together with the high pressures used to exclude liquid from under the template in a squeeze-film flow, complicating the etching process. Similarly, the placement of features is not accurate over large areas due to the low Young's modulus and high Poisson ratio of the PDMS template material together with the high pressures applied to the template. The cross sectional profile of features is often different from the shape of the template due to distortion of the template by the pressure applied to the template as well as the swelling of the template when exposed to solvent.[92] Finally, the features can show some non-uniform height over the length of features due to reflow of ink inside the template, driven by surface-tension interactions, as the solvent evaporates and the volume of liquid becomes less.[7,91]

1.5.6 Micromolding in Capillaries (MIMIC)

Micromolding in Capillaries (MIMIC), illustrated schematically in Figure 1.12, was invented as a low-cost alternative to standard photolithographic processes for creating patterns of polymer resists.[93] Here, a patterned template is created consisting of capillaries that extend to the edge of the template, which is then placed in contact with the substrate onto which features

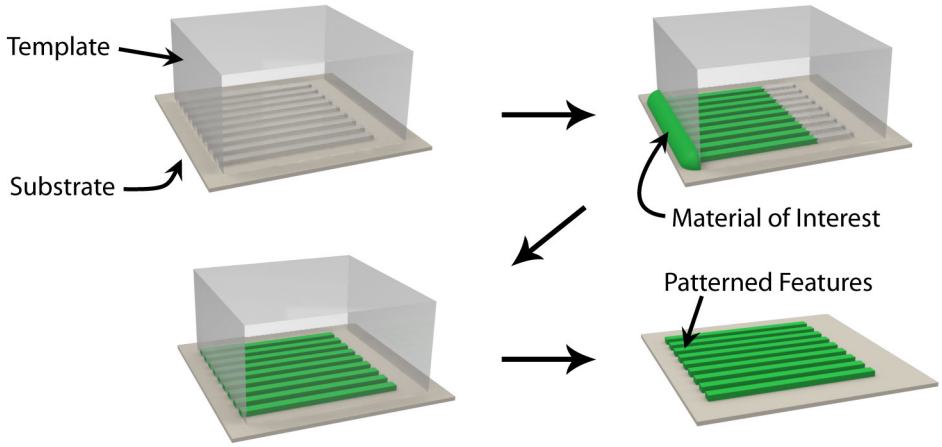

Figure 1.12: In the micromolding in capillaries process, a patterned template is placed in contact with a substrate. The template is filled with an ink containing the material of interest by capillary action. After the material is solidified in the template, the template is removed, leaving the intended patterns on the substrate.

are to be patterned. This template is typically made from PDMS, as this material is able to conform well to the substrate material and form capillaries that prevent any wicking of the ink between the mold and the substrate, ensuring that no unwanted residual layer is formed. Additionally, the high vapor permeability of the polymer allows gas to escape from the capillaries while the liquid ink fills, enabling the ink to fill longer distances. The ink is applied to the edge of the template and wicks into the features by capillary forces. At this point, as is the case in nanoimprint lithography, the rheology of the ink must change such that the ink does not reflow on the substrate after the template is removed. Originally, this was done using a polymer ink consisting of a UV activated crosslinker, patterned inside of a transparent template,[93] although this has also been done using a sol-gel chemical reaction[94] and by evaporation of solvent through the template.[95] Once solidified, the template is removed, leaving the patterns on the substrate.

The MIMIC process was originally developed for patterning polymers that are traditionally used in photolithography, although use of this process with other polymers and nanoparticles has also been demonstrated.[95,96] The process is capable of producing lines of as small as 300 nm in width,[94] with patterned lines having straight sides, vertical sidewalls, and uniform feature heights. Moderate aspect ratios, close to 1:1,[93] are attainable with this process due to the presence of a template during patterning and the rheology

change that occurs while the ink resides in the template. However, there are a few drawbacks to this process. Since this process depends on capillary action for filling features in the template, the process can be extremely slow, with the smallest features taking a very long time to pattern,[95] and features can only fill over a limited area, limiting the throughput of this process. Finally, the low Young's modulus of the PDMS template material combined with the pressures involved in keeping the template in conformal contact with the substrate as well as pressures from the capillary driven fluid flow cause deformation of the template, distorting the feature dimensions and making uniform, predictable dimensions difficult to achieve over large areas.[97]

1.5.7 Solvent Assisted and Solvent Absorption Micromolding

Solvent assisted micromolding (SAMIM) is another process that was developed as an alternative to traditional photolithography, originally for use with polymer resists. In this process, shown in Figure 1.13, a polymer film is spin-coated on a substrate to form a thin, uniform film. A soft PDMS stamp is created in the negative image of the desired pattern and is coated in a thin film of solvent that can dissolve the dried polymer on the substrate. The stamp is then pressed into the polymer film. The solvent dissolves the polymer film locally, allowing the polymer to deform and flow into the features on the PDMS stamp. Capillary wetting of the PDMS stamp with solvent drives the flow, allowing patterning with minimal external applied pressure. Eventually, the solvent absorbs into the PDMS and the polymer film dries and solidifies. The PDMS stamp is then removed, leaving the patterned polymer and a thin residual layer. This residual layer may then be removed by etching.[98]

Solvent absorption micromolding was developed slightly later using a similar operating principle. A schematic of the process is shown in Figure 1.13. Instead of using a dried polymer film on the substrate and dissolving the film in solvent, a polymer ink is applied to the substrate and patterned by pressing with a PDMS stamp. Once the features are filled with the polymer ink, the pressure is removed but the stamp remains on the substrate. The solvent is then allowed to absorb into the PDMS stamp, with the complete filling of the features assured by the capillary wetting of the solvent on the template. When the solvent is completely absorbed and the polymer dried, the stamp is removed, leaving the patterned polymer and a thin

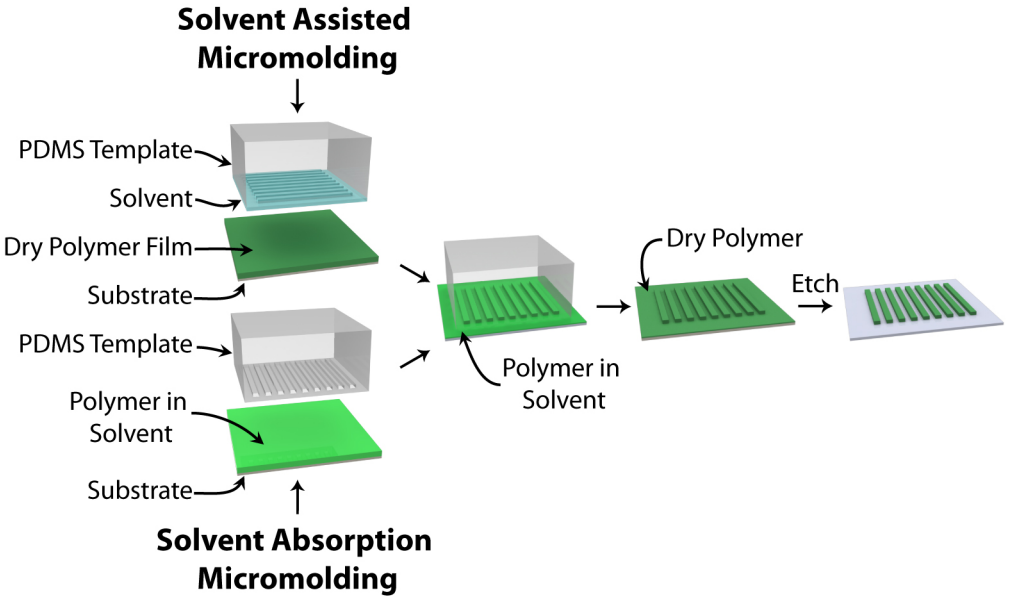

Figure 1.13: A schematic of the process flow for solvent assisted micromolding and solvent absorption micromolding. Patterns are created by either softening the material of interest using solvent spread on a template, or by pressing into an ink spread on a substrate using a dry template. The material solidifies as the solvent absorbs into the template, after which the template is removed and any residual layer is etched away.

residual layer. The residual layer may again be removed by etching.[98–100]

Since these processes were developed as an alternative to traditional photolithography, several different polymers have been patterned using these methods.[99,100] Nanoparticles have also been patterned using this process, although this work was characterized by the researchers as nanoimprint lithography.[7,91] Although, given that the importance of the solvent absorption into the PDMS templates to proper pattern transfer cannot be understated, perhaps such nanoparticle patterning is better denoted as solvent absorption micromolding.

While useful as a laboratory-scale processes, these methods have limited applicability to industrial manufacturing. In fact, they are remarkably similar to nanoimprint lithography, using solvent absorption into the template instead of temperature or UV-activated crosslinkers to change the rheology of the ink before and after patterning. This difference can be advantageous, as it increases the versatility of the process, enabling the use of a larger material set without the need for polymer binders or chemical additives. However, the use of solvent absorption to change the ink rheology can be

disadvantageous due to the increased difficulty of controlling the patterning fidelity over large areas. The PDMS templates distort under pressure and swell when exposed to solvents, causing feature dimensions to change and cross sectional profiles to become distorted. Additionally, several other disadvantages of the process also exist, which are similar to those seen in soft nanoimprint lithography, as discussed previously.

1.6 A Discussion of Patterning Processes for Nanoparticles and Polymers

It is important to evaluate the various patterning processes and, more broadly, the various classes of patterning processes, with respect to the established patterning metrics. Such a comparison, given in Figure 1.14, is useful to consider when determining a path forward toward a new patterning process. Understanding of the benefits and shortcomings of the various classes of patterning methods will enable desired features of each process to be combined and common drawbacks to be avoided.

Traditional patterning processes, including direct photolithography, lift-off processes, and thin film deposition and etching, have all been demonstrated to be able to produce features with excellent quality, alignment capability, and high throughput. However, these methods all suffer from a lack of versatility. A great deal of engineering effort must be expended to create the correct chemistries for each material used, including use of appropriate photoacids or crosslinkers and chemical etches and washes. Additionally, some materials are not chemically compatible with these processes at all, as the chemical modification of the material during patterning can destroy the desired properties of the material and therefore its utility as part of a device.

Alternative patterning methods, in general, decrease the dependence on the material properties and can eliminate the need for chemical changes that are typically used in the traditional patterning methods. The inkjet-based methods pattern material directly, altogether eliminating the need for any etching process. However, the method of patterning the materials does depend, to some degree, on the fluidic properties of the ink, again limiting versatility. Additionally, the lack of a well-defined boundary for the liquid ink on the substrate makes patterning of three-dimensional structures impossible, and writing individual features in a serial process has an inherently low throughput.

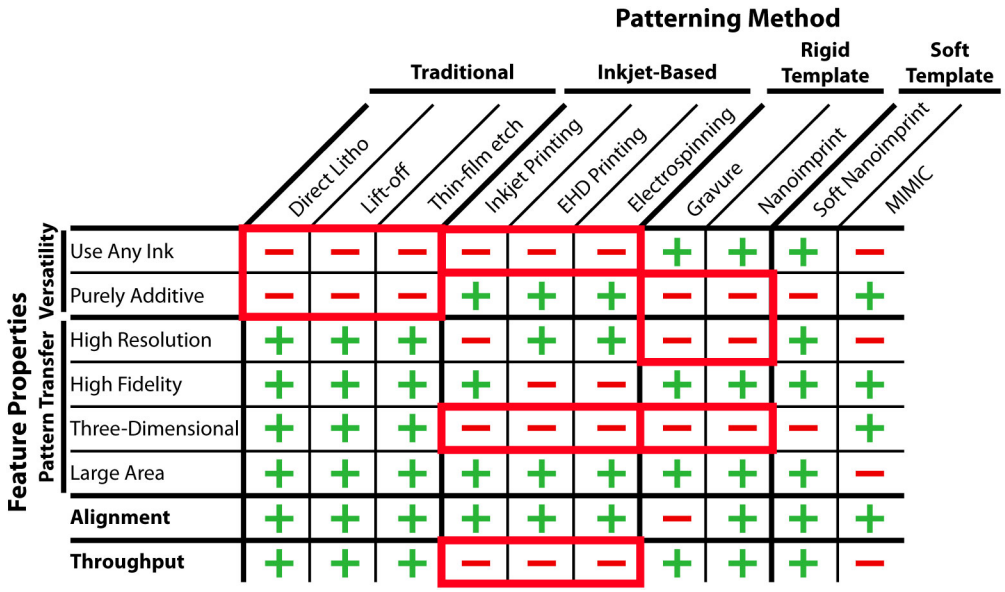

Figure 1.14: A comparison, with respect to fulfillment of the established patterning metrics, of the patterning methods discussed. The green plus sign indicates that the metric is satisfied, while the red minus sign indicates that the metric is not satisfied. A red box indicates that all processes within the given class fail to satisfy the given patterning metric.

The template-based methods are generally divided into two groups depending on whether they use soft, vapor permeable PDMS or hard, vapor impermeable ceramic, metal, or polymer templates. The hard templates suffer from problems related to pattern transfer, including the ability to pattern at high resolution and with control over three dimensions, due to the inability of the ink to change from a liquid to a solid while the template confines the ink on the substrate. Unlike inkjet patterning, where solvent can simply evaporate into the environment to solidify the ink, the presence of a solid template blocks this evaporation. While such solidification can be enabled by phase change or thermal or UV-activated chemical crosslinking, this changes the chemical nature of the material and limits the versatility of the process. However, the rheology of the ink can change while confined within the soft PDMS templates. This is due to the high vapor permeability of the template, which allows the solvent in the ink to absorb into or evaporate and diffuse through the template. While the currently available processes based on soft templates all have their own flaws, there is no critical flaw that is common to all patterning methods in this class.

1.7 Summary

Nanoparticles and polymers are important materials for a variety of applications in sensing and electronics. Patterning is important for realization of practical devices, and therefore many such processes have been developed for these materials. Of these, template-based methods are the most promising for creation of high resolution and high fidelity patterns in a versatile manner with high throughput and alignment capability. More specifically, those processes that use soft, vapor-permeable templates show the most promise for the ability to meet the desired patterning metrics. Currently, the methods of filling the ink in the template are not ideal, and improvements to the process may be able to create features of high quality, in a manner that is independent of the properties of the patterned material or substrate, with registration capability and at high throughput. Additionally, the correlation between rigid and vapor impermeable and soft and vapor permeable need not necessarily exist. Through the use of a simultaneously rigid and vapor permeable template, the best qualities of both classes of template based processes can be combined to produce patterns of even higher quality than possible with either class of template alone.

In the chapters that follow, a new process for patterning nanoparticles and polymers will be introduced. In Chapter 2, the process will be described and characterized using a soft and vapor permeable PDMS template. This process will explicitly rely on the vapor permeability of the template for both the filling of the template and the solidification of the ink. Some variations of the proposed process that can expand its capabilities are also discussed. In Chapter 3, the flow of solute in the template will be modeled mathematically, providing valuable insight into the operation of the manufacturing process. In Chapter 4, the process will be further refined by using a rigid and vapor permeable poly(4-methyl-2-pentyne) (PMP) template instead of the soft PDMS, allowing for a dramatic increase in pattern transfer quality. Detailed descriptions will be given of the polymer synthesis, casting, and use as a template in the proposed patterning process. In Chapter 5, the patterning will be converted into a continuous, roll-to-roll process, allowing for a potential increase in the patterning throughput and reduction of cost when incorporated into a larger roll-to-roll manufacturing system. Finally, in Chapter 6, the patterning capabilities of the process will be demonstrated by creating some practical devices, including low temperature metallization using sintered metal nanoparticles and patterning of zinc oxide nanoparticles to form a working ultraviolet light sensor.

Chapter 2

A New Template-Based Patterning Process

Template-based patterning processes hold great promise for creating simple, high-resolution, three-dimensional patterns on a substrate. The presence of a physical boundary for the ink allows for precise placement of materials and eliminates problems associated with reflow of ink as seen in template-less patterning methods. However, a remaining problem in these template-based methods is the handling of ink once inside of the template. Solidification of the liquid ink is necessary to prevent reflow on the substrate once the template is removed. While some processes admit reflow of ink and accept the corresponding reduction in attainable resolution,[70] others change the rheology of the ink by relying on ink-specific material properties or by changing the chemical structure of the material while inside the template. For example, thermal processing can be used to soften certain thermoplastic polymers during patterning and then re-solidify the ink when patterning is complete.[80] Alternatively, polymer binders and crosslinkers can be used to pattern a liquid ink formulation, followed by ultraviolet (UV) light or heat activated chemical crosslinking of the binder, causing solidification.[93] However, these approaches to solidifying ink are either dependent on the use of specific types of materials, or can adversely modify the chemical properties of the material being patterned, in turn affecting the performance of the device being created. A simple approach to changing the rheology of the ink while inside the template is by solvent absorption or evaporation through a vapor-permeable template. This has been done before in the con-

text of solvent assisted micromolding,[98] solvent absorption micromolding,[99] and nanoimprint lighography.[7] However, none of these processes patterns in a completely additive manner, which is critical for achieving high versatility with respect to the various materials and ink chemistries that can be used.

In this chapter, a new patterning process will be introduced that uses solvent evaporation through a vapor permeable template to drive the filling of a template with ink and concentrate the ink solute inside the template features. First, the process will be introduced conceptually. Further details on the patterning, including information on the materials and specific procedures used, will follow. Some experimental results from this basic patterning process will also be given. Finally, variations of the basic process which enhance the processing capability will be presented, and results shown.

2.1 The Microfluidic Molding Process

2.1.1 Process Description

The patterning concept is shown in Figure 2.1. A vapor-permeable template is created with the negative image of the features to be created on the substrate. These features must be continuously connected to a reservoir of ink, which may either be a vertical reservoir through the back of the template or simply the open edge of the template. A substrate onto which the features are to be patterned is coated with clean solvent, which can either be the same or different from the solvent used in the subsequent nanoparticle or polymer ink. The template is then pressed into the clean solvent, causing the solvent to fill the features completely. The filling of template features is driven by a combination of a pressure-driven flow driven by the pressure gradients present in the squeeze-film flow of fluid from under the template together with capillary filling of the solvent into the template. It is important that the features are filled without trapping any residual pockets of air, ensuring proper filling with ink in subsequent steps. Thus, a solvent that wets the template is preferred, ensuring complete coverage of the template surface with solvent and aiding in removal of air pockets from under the template. It is noted that while some of the solvent will inevitably be trapped under the template due to the pressure distribution in the squeeze film flow coupled with the finite elasticity of the template, this trapped solvent will evaporate completely through the vapor-permeable template in subsequent steps, leaving no residual layer. After filling the template fea-

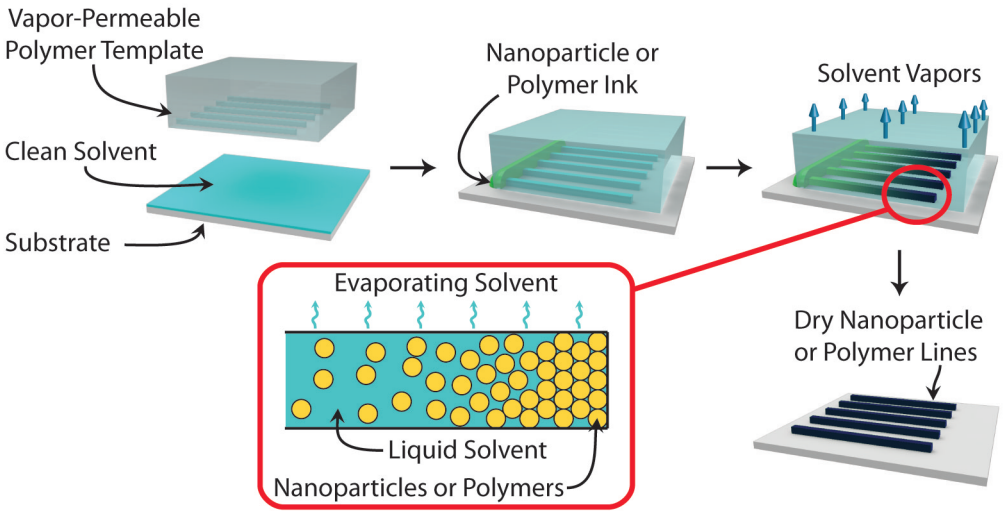

Figure 2.1: The microfluidic molding patterning process. A vapor permeable polymer template is positioned above a substrate which is coated in clean solvent. The template features are pre-filled with solvent by pressing. Nanoparticle or polymer ink is then added to the ends of the features. Evaporation of solvent through the template causes the ink to flow in the template, and further solvent evaporation causes densification of the solute in the ink. Eventually, the template features become completely filled with solute as any residual solvent is dried. At this point, the template is removed, leaving the patterned features on the substrate.

tures with clean solvent, the nanoparticle or polymer ink is added to the reservoir. The solvent evaporates through the vapor permeable template, which may be assisted by heating the system. The loss of fluid in the template due to evaporation causes a negative pressure inside the template, which causes fluid to flow through the template, replacing the material lost. This process, known as permeation pumping,[101] draws the nanoparticle or polymer ink from the reservoir into the template features. While this ink is inside the template, the solvent in the ink itself begins to evaporate, causing the solute to become more concentrated. The evaporation of solvent and concentration of solute continues until the templates are completely filled with solute and all of the solvent is removed. The template is then removed, leaving the dried patterns of nanoparticles or polymers on the substrate.

2.1.2 Experimental Procedure

Materials

The vapor-permeable templates were made from poly(dimethylsiloxane) (PDMS). While there are several choices in vapor-permeable polymers, as will be discussed in detail in Chapter 4, PDMS is chosen for initial prototyping work due to the high availability and corresponding low cost of the polymer as well as the simplicity with which the material can be patterned. These patterning templates were created by casting on a silicon master. The silicon master was created by spin-coating SU-8 photoresist (MicroChem) on a cleaned and dried silicon wafer and exposing it with UV light in the positive of the desired final patterns, crosslinking the polymer at those locations. A chemical developer was used to selectively remove the uncrosslinked photoresist, leaving only the positive image of the desired patterns on the silicon wafer. The wafer was placed on aluminum foil, which was bent up around the edges, forming a temporary and easily-removed container for subsequent PDMS casting. At this point, the PDMS pre-polymer and crosslinker were mixed in a 10:1 ratio by weight and poured over the silicon wafer master. The system was heated to 70 °C for approximately 2 h on a hotplate to crosslink the polymer. Once hardened, the aluminum foil container was removed from the PDMS and silicon wafer, and the PDMS gently detached from the edges of the silicon wafer and carefully removed from the silicon master.

The inks used in the patterning are widely varied, with solvents and concentrations highly dependent on the specific material used. It is noted that the physical properties of the ink are only indirectly related to its ability to fill the template. Since the template features are pre-filled with solvent by stamping, the gas phase is eliminated from the template features, eliminating any dependence on surface interactions between the ink and substrate. The clean solvent used to pre-fill the template is typically chosen to be the same as the solvent used in the ink. However, in the case that this solvent does not wet the template material, a different solvent that does in fact wet the template can be chosen. This ensures that no air pockets are trapped, which is critical to successful patterning using this process. The solvent used in the pre-filling must then be miscible with the solvent in the ink such that when the ink is added to the reservoir, the removal of the first solvent ensures the filling of the template with the second without introduction of any air bubbles. This solvent must also have a vapor pressure on the same order of magnitude or less than the solvent in the ink, ensuring

that the ink does not harden in the template prior to the complete removal of the solvent used to pre-fill the template. Hence, even inks that do not wet the template can be patterned, provided that a suitable miscible solvent that does wet the template can be found.

Since the patterning method can handle many ink formulations, specific formulations are chosen such that a stable suspension is created. For polymers, this simply means that the material is soluble in the solvent, whereas for nanoparticles, the particles must form a stable suspension without particle agglomeration or precipitation. The concentration of the ink formulations must be sufficiently dilute such that the ink flows easily into the channel and does not become so concentrated that it solidifies prematurely and clogs the channel during patterning. High concentration inks, however, are preferred to lower concentration inks as the channels are more quickly filled with solute, leading to lower patterning times. Thus, an ideal ink formulation is the highest concentration ink possible such that a stable suspension is maintained and the features fill completely without clogging prematurely. The materials used in the following experiments are listed in Table 2.1, and specific ink formulations will be given along with the corresponding results in subsequent sections.

A wide variety of substrates are used in the patterning, including many different ceramics and polymers. The patterning process is highly robust with regards to the physical properties of the substrate. While the solvent must fill the template completely without the generation of any air pockets, even solvents that do not wet the substrate are seen to fill the template. This is assisted by careful loading of the clean solvent onto the substrate in a manner that does not trap air bubbles on the substrate, as well as the wettability of the solvent into the recessed features in the template. While the template filling is simple with sufficiently planar substrates, those with more varied surface topology may be more difficult to fill, imposing the requirement that the substrate be wetting to the solvent used in stamping in order to avoid the formation of any trapped air pockets. The specific substrates used in the patterning will be given along with the corresponding patterning results shown in subsequent sections.

Patterning Procedure

The patterning was done using a customized patterning press, shown in Figure 2.2. This press consists of a movable platform actuated by a rotating screw turned by a stepper motor. The movable platform is connected to

Material	Substrates	Solvents	Pre-Fill Solvents
Gold Nanoparticles	Glass Polyimide Silicon	Terpineol Toluene	NMP Terpineol Toluene
Silver Nanoparticles	Alumina Glass Polyimide Silicon	Hexadecane Toluene	Toluene
Zinc Oxide Nanoparticles	COC Silicon	Water	None
Iron Oxide Nanoparticles	Silicon	Ethanol	None
Cellulose Acetate	COC Glass Polyimide Silicon	Acetone NMP	Acetone NMP
PMMA	Glass Silicon	NMP	Acetone NMP
ABS	Glass	Acetone	Acetone
PVDF	Glass	DMF	DMF
Chitosan	Glass	Acetic Acid	Acetone
Cell Culture Medium	Glass	Water	Acetone

Table 2.1: A list of nanoparticles and polymers used in formulating inks for patterning, along with the substrate onto which the material was patterned and solvents used in the patterning process. Materials with no pre-fill solvent listed were patterned only using the lift-off method described in Section 2.2.1.

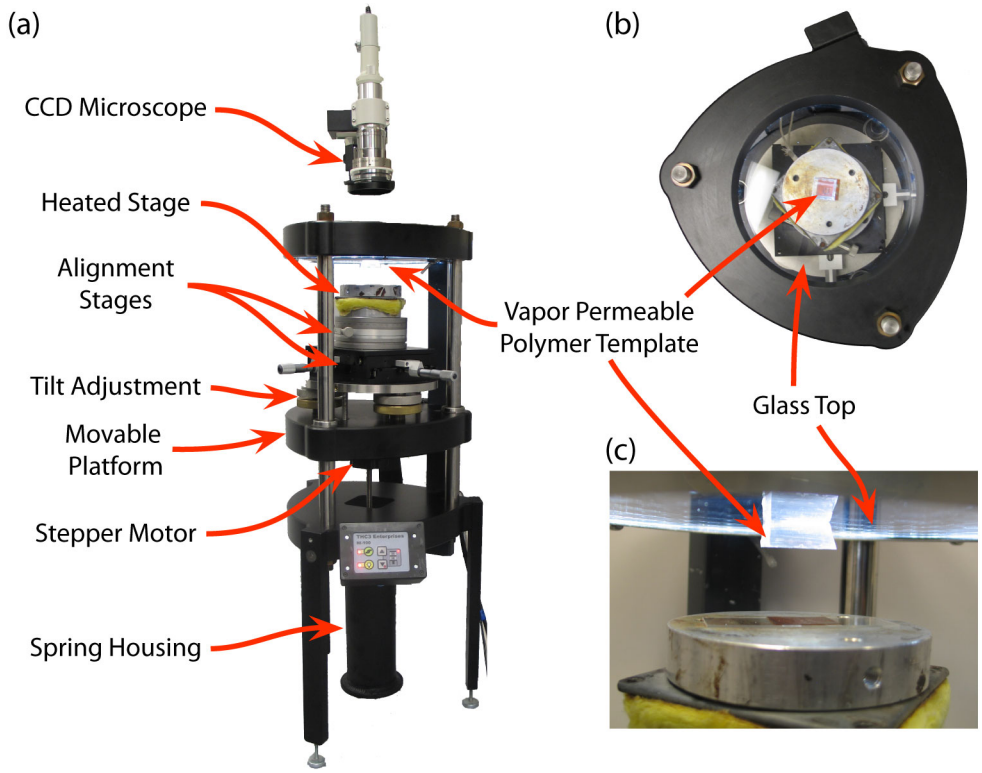

Figure 2.2: The press used in the patterning process. (a) A side view of the press assembly, with key parts labeled. (b) A top view of the press assembly. (c) A close up view of the polymer template mounted on the glass plate.

the actuator through a spring and a load cell, which allows a gradual and controlled amount of force to be applied by the press. On the platform is a tilt plate, which can be used to ensure that the template is sufficiently parallel to the substrate such that a uniform pressure can be applied over the entire template. Two orthogonal translation stages and a rotation stage are mounted on the movable platform, allowing precise alignment of the template to the substrate. A heated block with an attached thermocouple is then mounted on the alignment assembly, allowing control over the evaporation rate of solvent and therefore the patterning speed. The substrate is mounted on the heated block. Opposite this, a fixed glass plate is used as the top of the press, onto which the templates are attached. In the case of the PDMS templates, simple van der Waals forces are used for this attachment. Above the system, a CCD microscope with a long working distance is used to image the template and substrate, enabling alignment to be performed when necessary.

During patterning, the substrate is first placed on the heater block and the template on the fixed glass plate. The platform is raised until it is nearly in contact with the substrate, and then the tilt plate adjusted until the template and substrate are sufficiently parallel to each other, ensuring that uniform pressures will exist across the template when the two are pressed into contact. The platform is then lowered, and the clean solvent is loaded onto the substrate using a syringe. The movable platform is raised slowly until there is contact between the template and the substrate. This contact is then adjusted by further raising the stage until approximately 14 kPa of pressure exists at this interface. The ink is then loaded into the reservoir using a syringe. At this point, the heater may be used to increase the evaporation rate, if desired, increasing the speed of the patterning. Additional solvent may be added to the reservoirs during patterning, if needed. When the patterning is complete, the template is removed by lowering the platform, leaving the substrate with patterned features of solute.

The patterning system can be reused indefinitely with sufficient cleaning, creating many patterned substrates from a single template. The use of a vapor permeable template that is not explicitly porous prevents fouling of the surface of the template with solute. Complete and reliable release of features from the template is also observed for features with sufficiently small aspect ratio (typically less than 1:1), although the release properties of the template may vary depending on the specific inks and substrates used. However, while excellent release of patterns from the template is observed, it is recommended that the templates still be cleaned frequently to remove any residual solids on the surface and thus maintain good patterning quality.

2.1.3 Patterning Results

The patterning process was first demonstrated by patterning gold nanoparticles on a variety of substrates. Gold nanoparticles encapsulated in a hexanethiol monolayer having a diameter of approximately 4 nm were suspended in alpha-terpineol to a concentration of approximately 3.5 wt%.

The results of the patterning are shown in Figure 2.3. The particles were patterned on glass, polyimide, and silicon substrates. The chosen substrates have very different surface properties, with glass having very high surface energy, polyimide having low surface energy, and silicon having an intermediate surface energy. However, despite the different properties of the substrates, the patterning quality is similarly high for all three materials. The images of the patterns confirm that they were formed over large areas

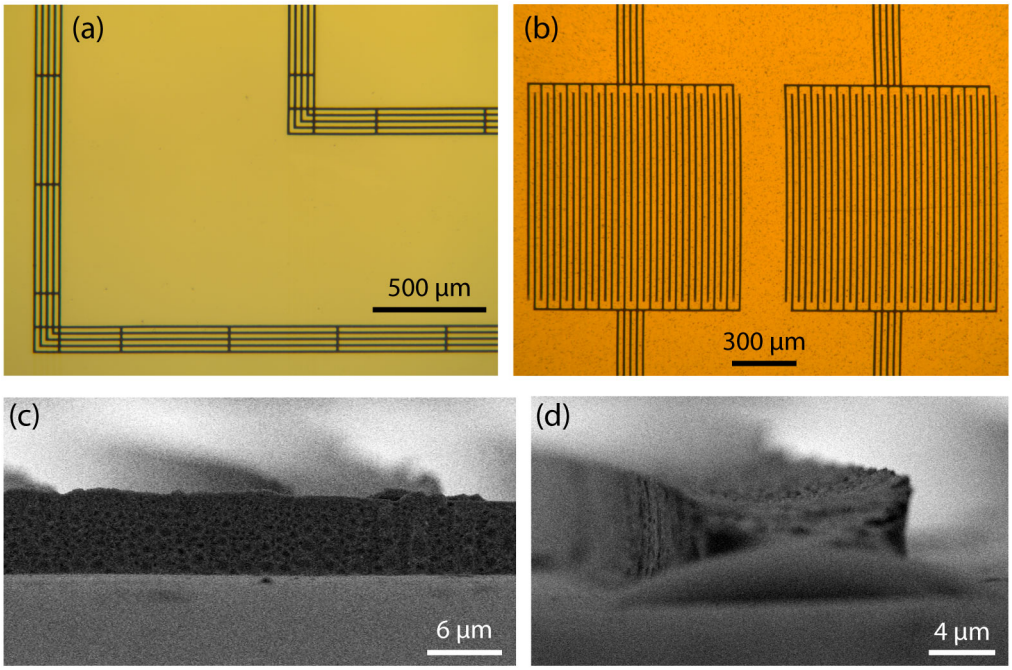

Figure 2.3: Patterning results using gold nanoparticles. Optical micrographs of gold nanoparticles on (a) glass and (b) polyimide, showing that patterns are formed over large areas with no residual layer. Scanning electron micrographs of gold nanoparticles on silicon showing (c) the height of features and (d) the cross sectional profiles, indicating that the template features fill completely with particles.

and with no residual layers formed. The tall features with rectangular cross sections indicate that the template features were, in fact, filled completely with nanoparticles.

In addition to nanoparticles, various polymers were also patterned, using both organic and aqueous solvents. The results from patterning these materials are shown in Figure 2.4. The polymers dissolved in organic solvents include poly(methyl methacrylate) (PMMA) dissolved in n-methylpyrrolidone (NMP) , poly(vinylidene fluoride) (PVDF) dissolved in dimethylformamide (DMF) , and cellulose acetate dissolved in acetone. Each of the materials were patterned on glass and silicon substrates. The results are similar to those for the nanoparticles, including patterning over large areas with no residual layer and with complete filling of the template features with solute.

In addition to organic solvents, aqueous solvents are also used in the patterning process. As an example, chitosan is dissolved in a mixture of 1% acetic acid in water. The chitosan was diluted to form solutions between

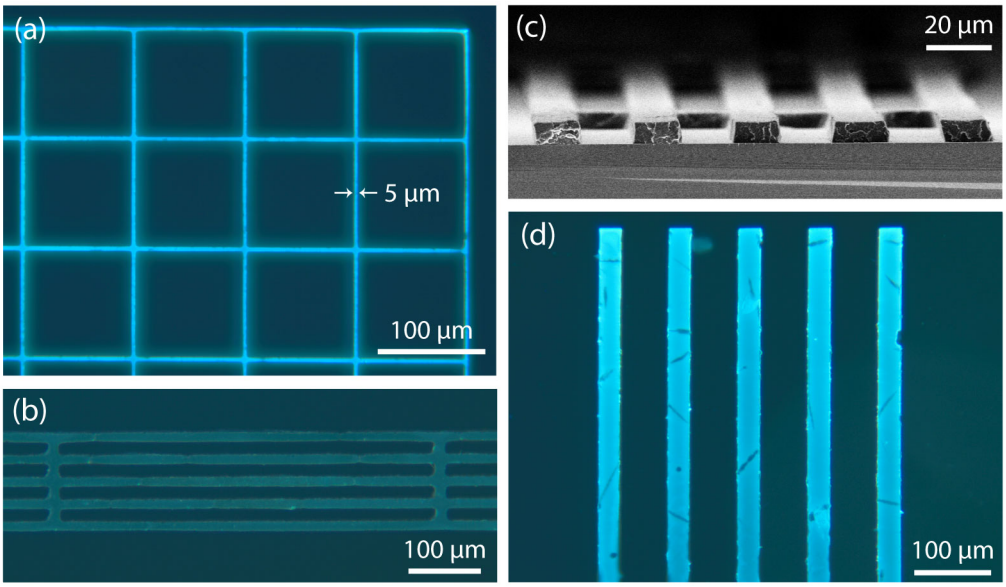

Figure 2.4: Patterning results using various polymers and cell culture medium. Optical micrographs of (a) chitosan, (b) PVDF, and (d) cell culture medium on glass. (c) Scanning electron micrograph of PMMA on silicon.

0.1 and 1 wt%. Since water does not wet the PDMS templates, acetone was used to pre-fill the templates, after which the chitosan in acetic acid was added to the reservoir and patterned. The results are again similar to other previous results, demonstrating that the patterning technique works equally well for both aqueous and organic solvents.

Finally, materials other than nanoparticles and polymers can be patterned as well, provided that they can be dissolved in a suitable solvent. As an example, used cell culture medium was patterned on a glass substrate. This medium contains salts, proteins, and cell parts, among other things, in an aqueous solvent. The medium was patterned using acetone to pre-fill the template, followed by filling with pure deionized water to remove the residual acetone and then the cell culture medium. The results were again similar to those seen previously, and are given in Figure 2.4.

2.2 Process Variations

Once the basic patterning procedure is determined, variations on the process can be created which increase patterning capabilities or enhance the basic functionality. Two such process variations discussed here are the patterning

of isolated features not possible with the proposed process alone, and the ability to pattern multiple different types of materials simultaneously using a single template.

2.2.1 Isolated Features

While isolated features are not possible using the microfluidic molding process, they can be patterned using a simple process variation as shown in Figure 2.5. In this two-step process, a polymer template with weak adhesion to the substrate is first patterned *in situ* on the substrate using the evaporation driven process described previously, followed by deposition of the material of interest using natural evaporation of a sessile droplet and mechanical lift-off of the patterned polymer template using an adhesive tape.

Process Description

This process for patterning isolated features is illustrated schematically in Figure 2.5. A PDMS mold with the positive image of the desired patterns is created by casting from a silicon master with the negative of the desired patterns, as described previously. This template is then used to pattern a polymer with low adhesion to the substrate, which is chosen here to be cellulose acetate. The polymer ink is created by dissolving the polymer in solvent (acetone) to a sufficiently low concentration, according to the conditions described previously. The clean solvent is used to fill the mold features by pressing, after which the mold is held in contact with the substrate using a light pressure not exceeding 14 kPa. The cellulose acetate ink is applied to the edge of the vapor permeable mold and the solvent evaporated, causing the ink to flow into the mold features. Continued evaporation of solvent causes cellulose acetate to concentrate in the mold features and, when the solvent is fully evaporated, the mold is removed, leaving the polymer template. This polymer template exists in the negative image of the desired pattern.

Following template creation, a brief oxygen plasma may be used to ensure that the subsequent ink used in the material deposition by natural evaporation spreads on the substrate, preventing non-uniform deposition of material caused by the Marangoni effect. At this point, a droplet of material in solvent is placed on the surface of the polymer template and allowed to evaporate at room temperature. To prevent unwanted destruction or

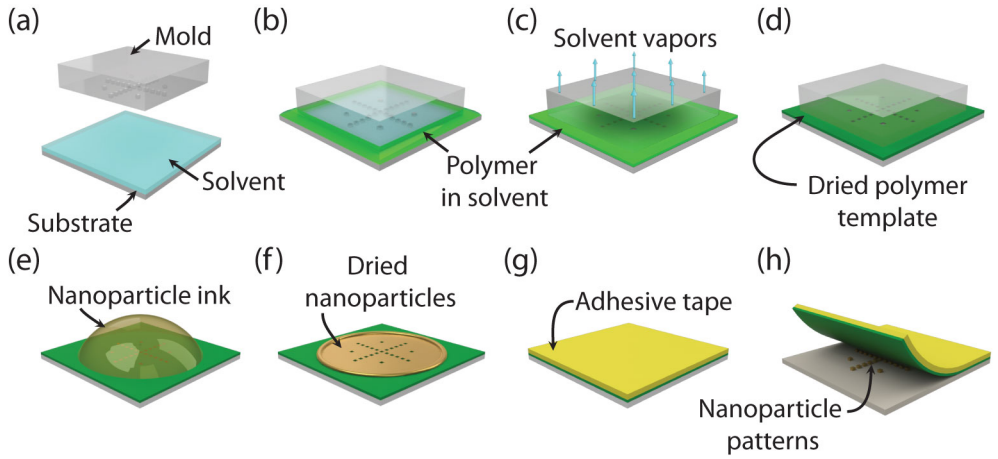

Figure 2.5: The patterning process for creating isolated features. (a) A vapor permeable polymer mold is positioned above a substrate that is coated with clean solvent. (b) The mold is used to pattern the solvent, and polymer ink is introduced around the sides of the mold. (c) The solvent evaporates, causing ink to flow inside the template features and the polymer to become concentrated, until (d) all of the solvent is removed and only the dried polymer remains. (e) The mold is removed and a droplet of nanoparticle ink is placed on the polymer template. (f) The solvent in the nanoparticle ink dries, leaving the particles on the surface. (g) Tape is placed over the template, and (h) the template is pulled from the substrate, leaving only the nanoparticle patterns.

distortion of the polymer template, the solvent used to carry the material must be completely compatible with the polymer template. A convective transport of the particles induces the formation of coffee-ring deposits, and the material of interest fills into the patterned features uniformly, assisted by the induced corner flow[33] and possibly by the enhanced electrostatic attraction between the particles and the substrate due to deprotonation of the substrate resulting from the oxygen plasma treatment.[102] When the system is dry, an adhesive tape is adhered to the surface of the polymer template. The tape is then pulled from the surface, removing the polymer template and trapping any residual particles between the template and the tape, preventing them from settling on the substrate.

Experimental Results

As an initial demonstration, zinc oxide (ZnO) nanoparticles were patterned on silicon and cyclic olefin copolymer (COC) substrates. Cellulose acetate

ink was created by combining polymer sheet with acetone to a 4% concentration. The vapor-permeable polymer mold was created using PDMS, and the cellulose acetate was patterned on silicon and COC substrates using the PDMS mold at room temperature. Following patterning, an oxygen plasma was applied at 30 W for 10 s at 280 mTorr. ZnO nanoparticles (40 wt% of 30 nm diameter particles in water) were diluted into various concentrations of suspension (2.5, 1.25, 0.625, and 0.3125 wt% solutes) by adding a controlled volume of deionized water. The nanoparticle deposition was performed at room temperature and atmospheric pressure. A microsyringe was used to extract a small volume (0.5 - 2.0 mL) of the ZnO nanoparticle solution and a single droplet was placed on the patterned substrate, after which the sample was left at room temperature for 1 h to evaporate the solvent completely. Once the solvent was completely evaporated, the nanoparticles formed a coffee ring on the template with a uniform layer of nanoparticles deposited inside of the ring, as shown in Figure 2.6(a). Finally, crepe paper masking tape was used for the mechanical lift-off. The result was the ZnO nanoparticle patterns on the substrate, as shown in Figure 2.6(b), separated from the polymer template shown in Figure 2.6(c). The particles deposited in the interior of the ring are well adhered to the substrate and are completely patterned everywhere. However, for patterns formed under the ring, some defects are seen as some patterns are missing. This is due to the nanoparticles overflowing the wells, bridging over the template and thus greatly increasing the force applied to the nanoparticle pattens when the template is removed. The increased force during template removal can cause some features to be removed, but only in the area of the coffee ring. To avoid such defects, features should be designed such that they exist completely in the interior of the coffee ring.

The results of the ZnO patterning are shown in Figure 2.7. A large, dense array of isolated squares of particles with a width of 20 μm at a 1:1, 1:2, and 1:4 spacing was formed on the substrate. Each individual square showed good, uniform packing of nanoparticles with no visible cracks or defects. The heights of the patterned features were found to be quite uniform over the printed area, except for an increase in feature heights near the location of the coffee ring on the template, and were controllable by varying the concentration of the nanoparticle ink. It is interesting to note that the pinning of the contact line by nanoparticles at the edge of the droplet plays a significant role in ensuring uniform deposition of nanoparticles inside the coffee-ring region. While nanoparticles are being deposited downward in the drying liquid film, excessive particles are convectively transported toward

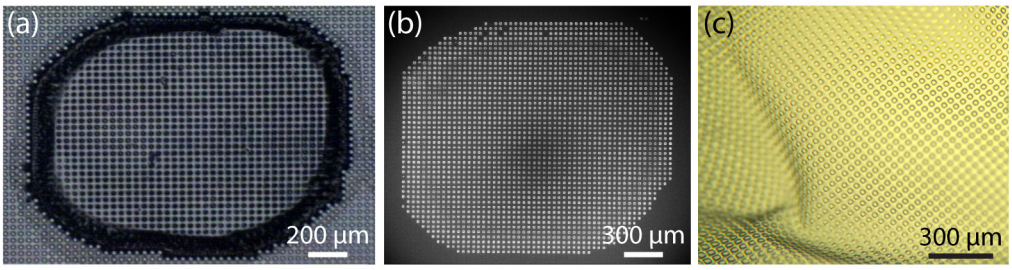

Figure 2.6: Images of the ZnO nanoparticle patterning process. (a) Optical micrograph of ZnO nanoparticles deposited in a coffee ring on a cellulose acetate template on silicon. (b) Scanning electron micrograph of nanoparticle patterns on a silicon substrate after lift-off. (c) Optical micrograph of a released cellulose acetate film.

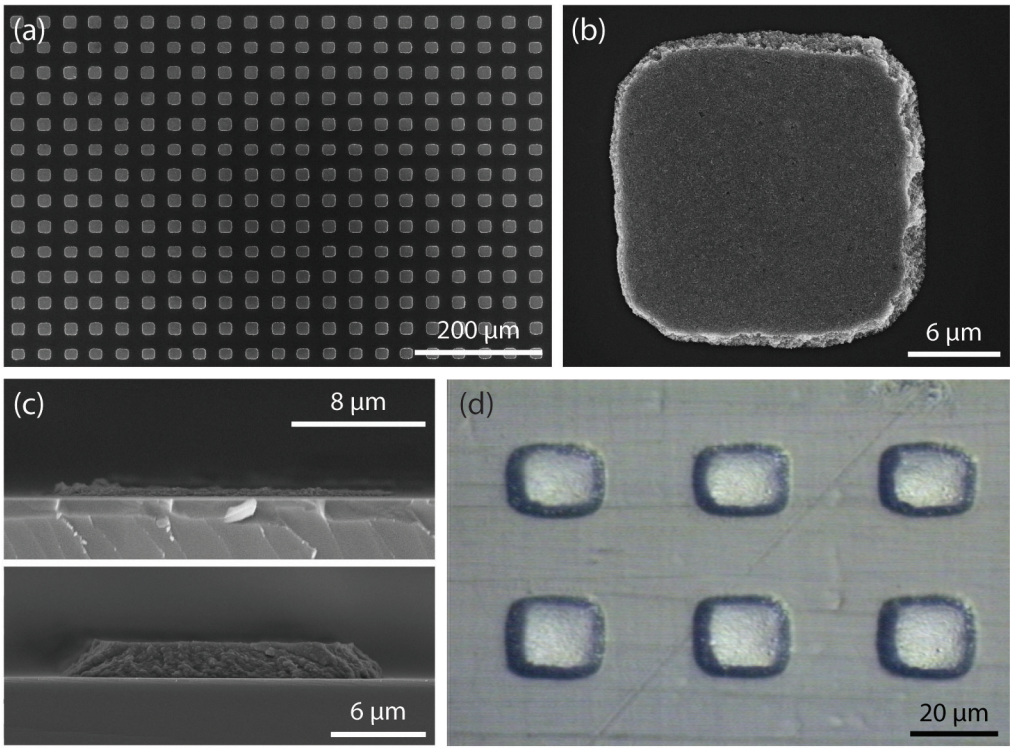

Figure 2.7: ZnO nanoparticle patterns. Scanning electron micrographs of ZnO nanoparticles on a silicon substrate (a) in a large array with 1:1 spacing and (b) individually. (c) Scanning electron micrograph showing the height of patterns using 1 wt% (above) and 2 wt% (below) concentration inks. (d) Optical micrograph of ZnO nanoparticles on a COC substrate.

the edge and form a thick coffee-ring deposit. This transport is caused by a hydrodynamic effect of an evaporating droplet and occurs only if the contact line is pinned at the edge of the droplet.[33,103] If the volume fraction of the particles is too low, the contact line will not be pinned and particles will be deposited as it recedes, causing variation in the feature heights. The thinnest features to be uniformly deposited were created using a 1 wt% nanoparticle solution, resulting in a layer with a thickness around 300 nm and with dimple structures caused by an instability at the particle suspension-air interface.[104] Finally, the sidewalls of the patterned features do show some fracture due to a shearing force caused by the mechanical lift-off, resulting in nearly 45° sidewalls, which are seen to be very repeatable.

For further characterization of the process capabilities, patterns of ZnO nanoparticles were formed over large areas. Such large area patterns of nanoparticles were also formed using the same method described above. A 56 mm square array of 20 μm squares at a 40 μm pitch were patterned on a 100 mm silicon wafer substrate. A cellulose acetate template was created which contained a large, vertical cellulose acetate ring around the extent of the patterned area. A 1 wt% ZnO nanoparticle suspension was spread over the entire template by pinning its contact line at the global cellulose acetate side wall, as seen in Figure 2.8(a), and allowed to dry. Following the nanoparticle deposition, the mold was removed in strips using crepe paper masking tape. Due to the limited width of the tape, the entire area could not be removed at once, but a clean tearing of the template at the edge of the tape allowed for the entire template to be removed one strip at a time. The features were indeed patterned over the entire area, as shown in Figure 2.8(b), although uniformity of the height of the features over the area was not ideal due to the non-uniform coating of the area with nanoparticle ink in the final stages of solvent evaporation. That is, the large volume of liquid ink coating the template broke up into several smaller droplets with non-uniform volume near the end of patterning, causing wells in different areas to receive different amounts of nanoparticles. More uniform patterning could be obtained by controlled deposition of many smaller droplets of nanoparticle ink over the template using an array of inkjet printing heads, microsyringes, or any other similar droplet deposition system.

In addition to the ZnO nanoparticles, magnetic iron oxide nanoparticles were also patterned on a silicon substrate. The iron oxide nanoparticles were suspended in ethanol at a concentration of much less than 0.01%. The particles were deposited onto a cellulose acetate template in a manner similar to the ZnO nanoparticles. However, some modifications in the particle

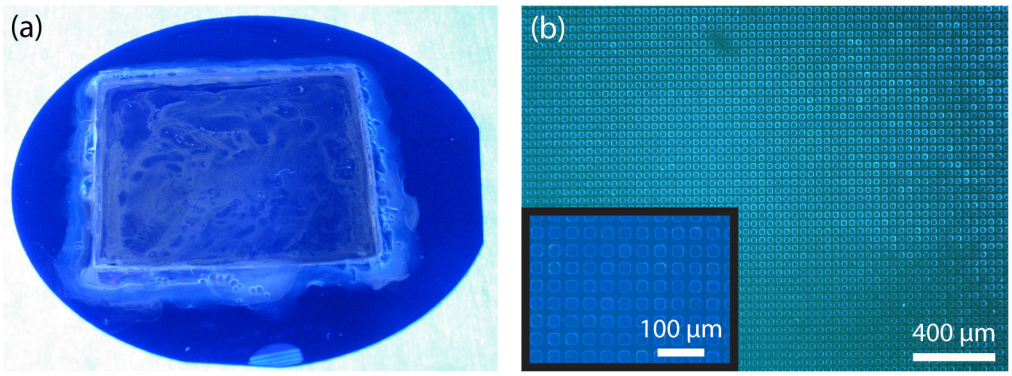

Figure 2.8: ZnO nanoparticle patterns over large areas. (a) The ZnO nanoparticles on a cellulose acetate template patterned on a 100 mm silicon wafer. (b) Optical micrograph of the resulting patterns of ZnO.

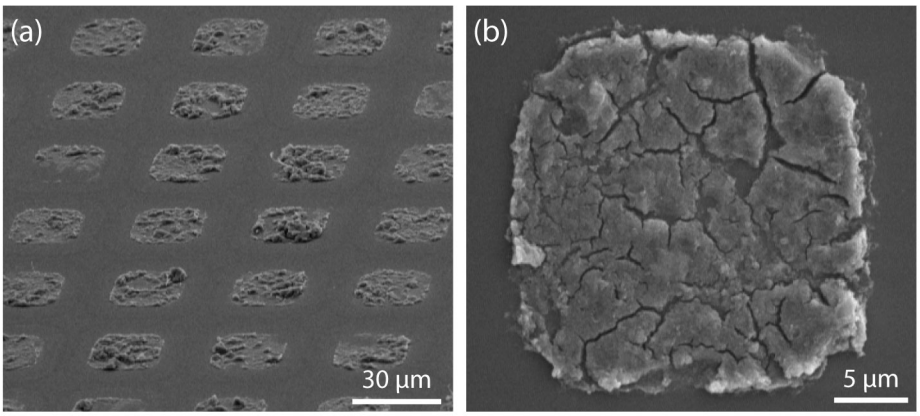

Figure 2.9: Iron oxide nanoparticle patterns. (a) Patterns of iron oxide, showing a lack of uniformity between features caused by particle agglomeration during patterning. (b) A single iron oxide feature, showing a high level of cracks and defects again due to the particle interactions during patterning.

deposition were necessary due to the low concentration of the nanoparticle ink as well as the high propensity for the nanoparticles in the ink to agglomerate during the deposition. No coffee ring was formed due to the low particle concentration, and the droplet deposition and solvent evaporation was done multiple times in the same area to achieve sufficiently high particle densities on the substrate. To prevent agglomeration of nanoparticles during the particle deposition, the substrate was placed on a plastic weigh boat suspended inside of an ultrasonic bath.

The iron oxide nanoparticles were patterned into squares of 20 μm on a

side and with a spacing of 20 μm, as shown in Figure 2.9. Clear patterns of nanoparticles are formed over the entire intended area. However, unlike the ZnO particles, the heights of the features are not uniform, and the features contain many cracks and defects. This is due to the agglomeration of nanoparticles during deposition, which is especially strong towards the end of the deposition process when the ink is highly concentrated.

To further characterize the lift-off process, the peeling forces required to remove the cellulose acetate from the silicon or COC substrates and the tape from the cellulose acetate were measured. Cellulose acetate was dissolved in acetone to a 9% concentration and spin-coated on the appropriate substrate to a thickness of 5 μm. Tape was adhered to the film, and the film was cut with a razor blade to match the contact area with the tape. Excess tape was folded over and attached to a fluid container by means of a light, flexible metal wire. The tape then made a 180° peel angle with respect to the substrate. Weight was gradually added to the fluid container by adding drops of water until the film begins to peel steadily from the substrate and was unable to reach a stationary equilibrium. At this point, the weight of the fluid, container, wire, and folded tape was measured to determine the force applied to the film at peel-off. The peel force is determined by dividing this force by the width of the tape. The experiment was repeated five times for each adhesion measurement, and the standard deviation of these five trials was taken as the uncertainty in the measurement. The resulting peeling force required to remove the cellulose acetate from silicon was 3.8 $\pm$ 0.5 kN/m and from the COC was 2.1 $\pm$ 0.3 kN/m. The force to remove the tape from the cellulose acetate was 100 $\pm$ 10 kN/m. The difference in peeling force of over 25 times explains the reliability with which the mechanical lift-off can be used to remove the template without leaving any residual template on the substrate. That is, a strong adhesion between the template and the tape is used to overcome a weak adhesion between the template and the substrate, allowing complete and simple removal of the template.

2.2.2 Multiple Materials

While the basic process has been, to this point, used only for creation of patterns of a single material, a simple process variation can be used to create pattens of multiple materials at the same time in a single template. Such a patterning process could reduce the number of necessary processing steps needed to create a practical device, reducing the time and the overall cost

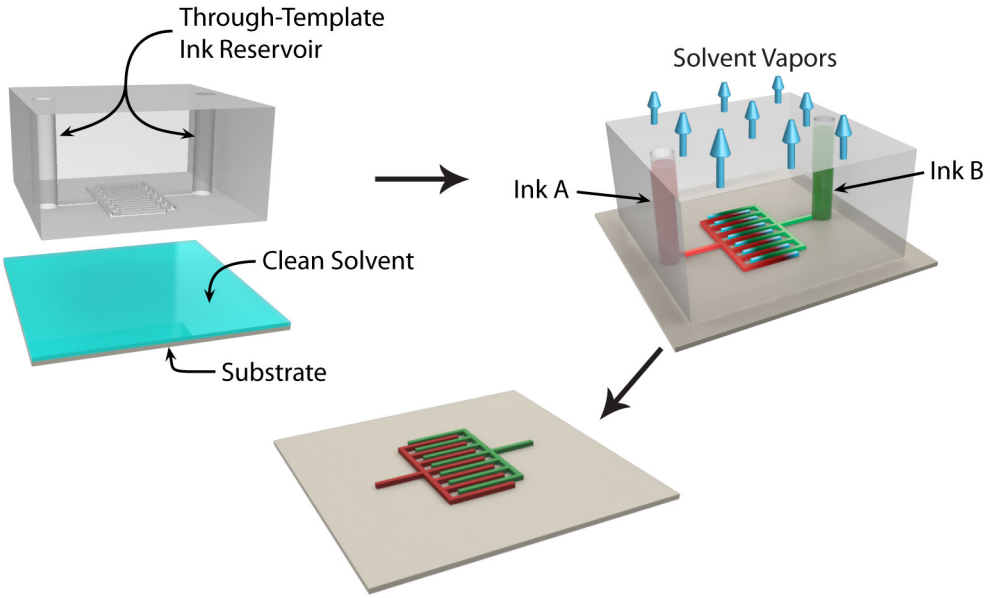

Figure 2.10: Process for patterning multiple inks simultaneously. A template with multiple ink reservoirs is pressed into a substrate that is coated with clean solvent. Multiple different inks are loaded into the different ink reservoirs. Evaporation of solvent through the vapor permeable template causes these multiple inks to flow into the features and concentrate the solute. When dry, the template is removed, leaving patterns of the multiple materials on the substrate.

of the patterning.

Process Description

The process for patterning multiple different materials in a single step is shown in Figure 2.10. The process is dependent on the ability to connect different features in a template to separate, isolated reservoirs. Thus, the geometry of the template is different, but the process is otherwise identical.

The vapor permeable templates are created again from PDMS, albeit by a slightly different process. A silicon master is patterned using SU-8 photoresist using standard photolithography in the positive image of the features to be patterned. However, instead of having the reservoir to exist on the side of the template by simply having features extend past the edge of the PDMS template, multiple isolated reservoirs are molded through the back side of the template. To do this, an acrylic plate is drilled with holes that match the locations on the wafer where the reservoirs are to be made and positioned above the wafer. Metal taper pins are set in the holes of

the acrylic plate, extending down to touch the wafer at the locations where the reservoirs are to be molded. The taper pins are positoned such that the narrow ends are on the wafer and the wide ends on the acrylic plate. A 10:1 mixture of PDMS pre-polymer and crosslinker is the poured onto the wafer and cured on a hotplate, as described previously. When the PDMS is hardened, the acrylic plate is removed and the pins carefully pulled from the PDMS. The PDMS is then removed from the silicon wafer and cut into templates as described previously, but this time without allowing any features to extend past the end of the template.

For the patterning of multiple materials, a separate press was constructed that allowed access to the ink reservoirs in the back of the template. This press, shown in Figure 2.11, consisted of a moving platform onto which a heated spring stage is mounted. The spring stage allows for gradual pressure to be applied as the template makes contact with the substrate as well as for the template and substrate to become parallel as soon as contact is made. The heater on this stage allows for control over the evaporation rate and therefore the patterning speed. Opposite this is a fixed top onto which the acrylic plate containing holes matching the location of the reservoirs, as was used in the PDMS template creation process, can be mounted. The PDMS templates are adhered to the acrylic plate by simple van der Waals forces, and are positioned such that the ink reservoirs in the template align to the holes in the acrylic plate.

The patterning process then follows the basic procedure that was given previously. The substrate is placed on the heated spring stage and coated with solvent. The moving platform is then raised to bring the substrate into contact with the template, causing the template features to fill with clean solvent. At this point, the multiple different types of inks are loaded into the multiple different reservoirs. Evaporation of solvent through the template causes the ink to flow into the template features and concentrate, eventually packing the features completely full of solute. When the solvent is dried, the template is removed, leaving the materials patterned on the substrate.

Experimental Results

The patterning process was first demonstrated by patterning acrylonitrile butadiene styrene (ABS) and cellulose acetate, both dissolved in acetone, on a glass substrate. The patterns featured alternating lines of each polymer with a width of 15 μm and a spacing of 15 μm. The resulting patterns are

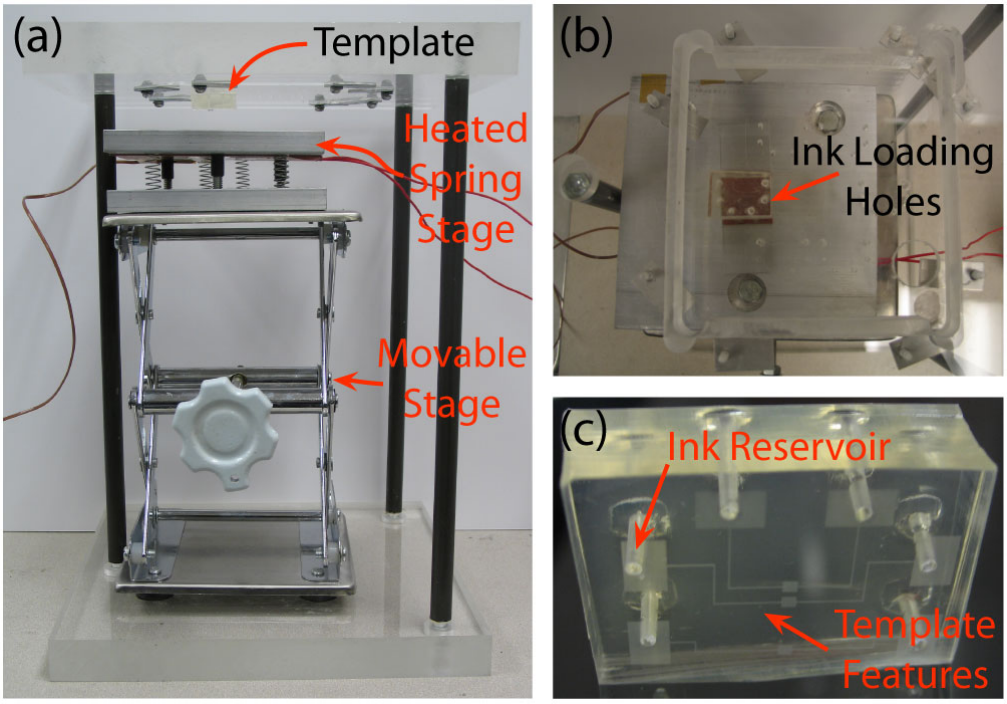

Figure 2.11: The press used for patterning multiple materials in a single patterning step. (a) A side view of the press assembly, with key parts labeled. (b) A top view of the press assembly. (c) A close up view of the polymer template, containing ink reservoirs connected to the recessed channels.

shown in Figure 2.12(a). The patterns of each material were reproduced well, resembling the results of polymer patterning with the basic process described previously for patterning a single material.

To further demonstrate this process, PMMA dissolved in NMP was patterned together with cellulose acetate dissolved in acetone on a glass substrate. The templates were pre-filled by stamping with acetone, followed by addition of the two inks using two different solvents. The acetone was allowed to evaporate at room temperature and, when the cellulose acetate was fully patterned, the system was heated to 75 °C to evaporate the NMP and pattern the PMMA. The intended patterns again featured alternating lines of each polymer with a width of 15 μm and a spacing of 15 μm. The results are shown in Figure 2.12(b). The patterns were reproduced well, with the different types of polymers clearly distinguished from each other after patterning. However, some difference in the size of the patterned lines is observed. This difference in the width of patterned lines is due to the

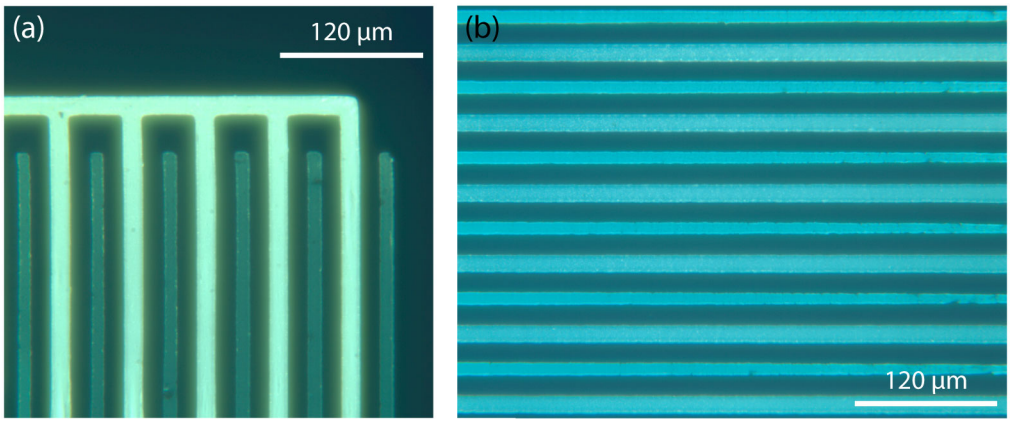

Figure 2.12: Results for patterning multiple inks. Optical micrographs of (a) cellulose acetate and ABS, and (b) cellulose acetate and PMMA patterned on a glass substrate.

different physical properties of the two polymers in their respective solvents. As discussed in Chapter 3, the viscosity of the ink increases exponentially with concentration, and this rate of increase is dependent on the specific polymer and solvent used.[105] Rapid increases in viscosity create a high pressure drop across the length of the channel, causing the soft PDMS template to distort. Such a size difference could be eliminated by optimizing the initial concentration of the ink supplied to the reservoir, as will be discussed in Chapter 3, or using a template with a higher modulus of elasticity, as will be discussed in Chapter 4.

To further test the ability to pattern multiple materials together in a single processing step, both nanoparticles and polymers were patterned in close proximity. Gold nanoparticles in terpineol solvent and cellulose acetate polymer in NMP solvent were patterned on a polyimide substrate. The results are shown in Figure 2.13. Again, the different material lines exhibit slightly different line widths, again due to the difference in the rate of increase of viscosity of the two different types of inks with increasing viscosity. The larger polymer molecules are much more susceptible to increasing viscosity than the smaller nanoparticles, and thus exhibit a larger distortion in the patterned features.[105–107] This distortion could again be minimized by lowering the concentration of the ink loaded into the reservoir or using a more rigid template material.

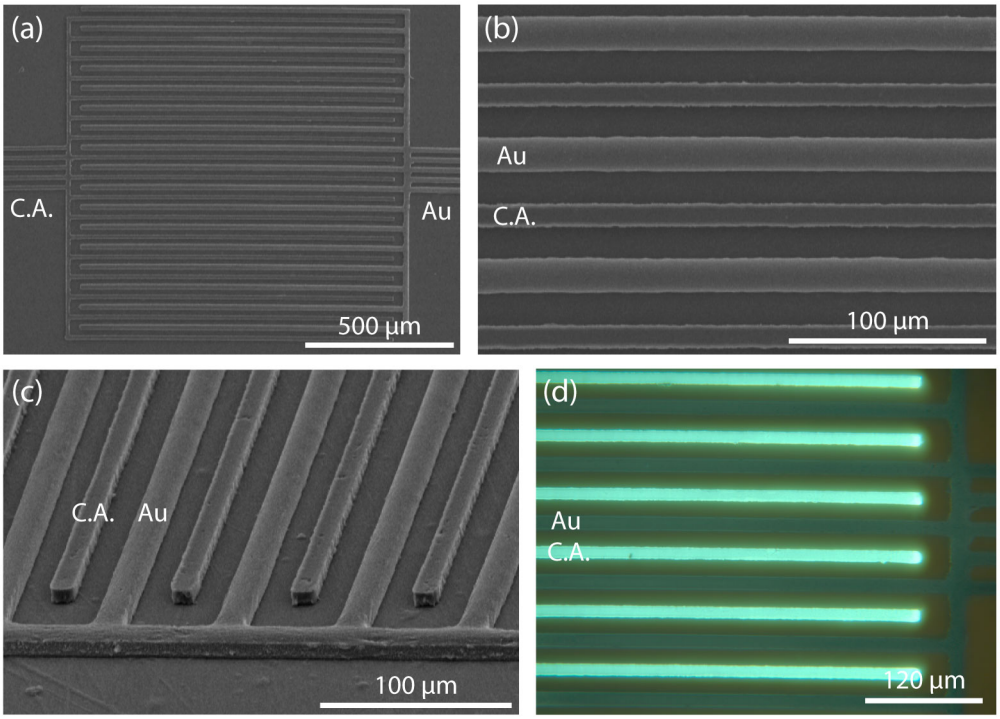

Figure 2.13: (a) An SEM micrograph of gold and cellulose acetate lines patterned on a polyimide substrate. (b) A closer view of the two materials, showing a larger degree of dimensional distortion on the polymer line as compared to the nanoparticle line. (c) An image of the lines taken at a 60° tilt, showing the height of the features. (d) A fluorescence micrograph of the patterned lines, showing clearly the difference between the two materials.

2.3 Future Directions

While the above work demonstrates the patterning concept, significantly more work must be done to further refine the process. This includes creating specialized templates and a corresponding press for better solvent handling and enhanced speed, development of better design rules for patterning conditions to ensure optimal processing speed for a given combination of inks and substrates, and refining the lift-off process for use in patterning multiple different types of materials, with alignment, in close proximity.

Current templates are limited in terms of their ability to handle solvent. The templates are thick and solid, and are sandwiched between a vapor-impermeable substrate and a vapor-impermeable glass plate. The solvent is forced to leave through the sides of the template, resulting in long diffusion paths for the solvent and therefore limiting processing speeds. Better solvent

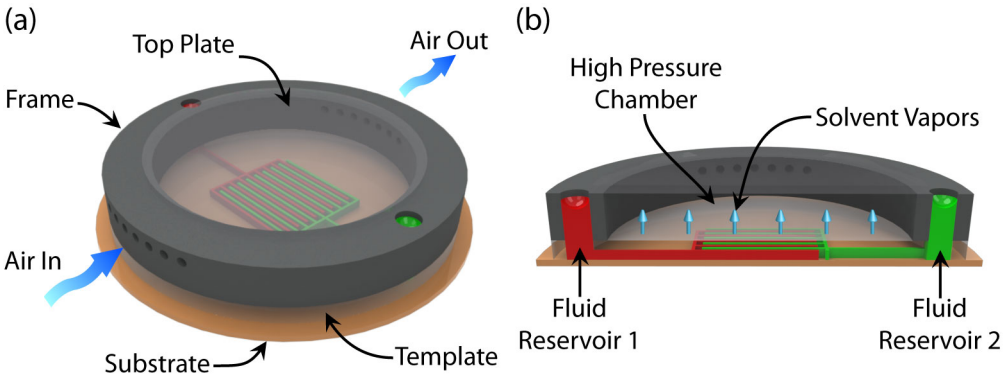

Figure 2.14: (a) A schematic of an improved patterning template and press system. A thin template is held in contact with the substrate using a rigid frame and high pressure air moving over the template. (b) A cross-sectional profile of the same system.

handling requires a different template design that shortens the diffusion path for solvent and increases the evaporation rate, lowering processing times. One such possible design is shown in Figure 2.14. A thin template is held in contact with the substrate using pressurized air, which is continuously replaced with fresh air to ensure a maximum diffusion rate through the template. Solvents may be loaded through discrete reservoirs on the edge of the template, ensuring maximum versatility by allowing patterning of multiple materials in a single template.

Processing conditions, such as temperatures and times, are used to ensure proper patterning of materials at the highest possible speed. Patterning for insufficient times will cause incomplete solidification of ink and cause poor pattern transfer in areas close to the reservoir. While increasing the temperature will decrease the necessary time, exceedingly high temperatures can cause vapor bubbles to form in the channel, interrupting the flow of ink in the template. Design rules for the process are therefore desired so that appropriate processing conditions can be determined for the various solvents used.

Finally, the process for patterning isolated features using mechanical lift-off of an *in situ* patterned polymer template currently only patterns a single material at a time. Modification of the process is needed to allow for patterning of multiple materials using a single template. This could be done by filling the wells in the template selectively, using inkjet printing or other equivalent processes to place ink in selective location, instead of the simple evaporation of a large sessile droplet as described in this work. Such local

deposition of droplets could also be useful in assuring repeatable material deposition over large areas, as discussed previously.

Chapter 3

Process Modeling

A fundamental understanding of the operation of the proposed patterning process is important for its application to a larger set of materials and geometric configurations. Such an understanding can assist in identifying any limitations of the process and creation of any necessary design rules, as well as developing a better understanding of how the proposed process is differentiated from previous processes. In this chapter, an analytical model of the patterning process will be developed and analyzed in order to develop insight into the operations of the process.

3.1 A Description of the Model

A model of the evaporation-driven filling of a channel with solute is desired. The model is shown schematically in Figure 3.1. The channel is modeled as a one-dimensional entity, having only the dimension of length. The concentration C_m as a function of position along the length of the channel z and time t is desired. Since, in reality, the channel is a three-dimensional entity, the concentration in this model actually represents the average concentration across the width and height of the channel. Similarly, the velocity v of the moving fluid is only a function of the distance along the length of the channel. Again, this one-dimensional velocity actually represents the real velocity averaged across the width and height of the channel.

The flow is driven by evaporation of solvent through a vapor permeable polymer template. Here, this evaporation of solvent is modeled using a volumetric flow rate per unit of permeable surface area q", which is assumed

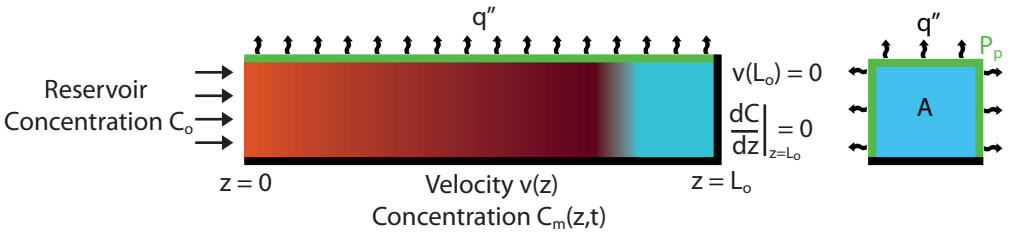

Figure 3.1: An illustration of the mathematical model. The concentration of solute in the channel as a function of position and time is desired.

to be a constant that is independent of position and particle concentration. The vapor permeable portion of the perimeter is given by P_p and a cross-sectional area given by A. The channel is assumed to be free of all nanoparticles when the patterning begins at time $t = 0$. The source of the nanoparticles is then a reservoir, located at $z = 0$, which is assumed to have a constant concentration of solute given by C_0. The other end of the channel at $z = L_0$ is assumed, for simplicity, to have zero velocity. That is, evaporation of solvent through the end of the channel is neglected here. Additionally, the end of the channel at $z = L_0$ is assumed to have zero flux of particles though the wall.

The particles in this model are subject to particle diffusion. These particles are assumed to have a diffusivity D given by the Stokes-Einstein relation

$$D = \frac{k_B T}{6\pi\eta r_p} \tag{3.1}$$

where η is the fluid viscosity, r_p is the particle radius, k_B is the Boltzmann constant, and T is the temperature. However, the value of the diffusivity must be modified to include shear-enhanced diffusion caused by velocity gradients perpendicular to the direction of the flow, which are neglected in the one-dimensional model used here. The source of this enhanced diffusivity is illustrated in Figure 3.2. The presence of velocity gradients perpendicular to the flow cause an increased mixing of nanoparticles as compared to a similar flow having the same average velocity but without these velocity gradients. To understand why, consider a section of fluid in a two-dimensional channel containing a simple Poiseuille flow with a parabolic velocity profile. After a short time, an initially straight section of fluid is distorted into a parabolic shape, with the center of mass of the distribution of particles moving a distance given by the average velocity of the flow v multiplied by the elapsed

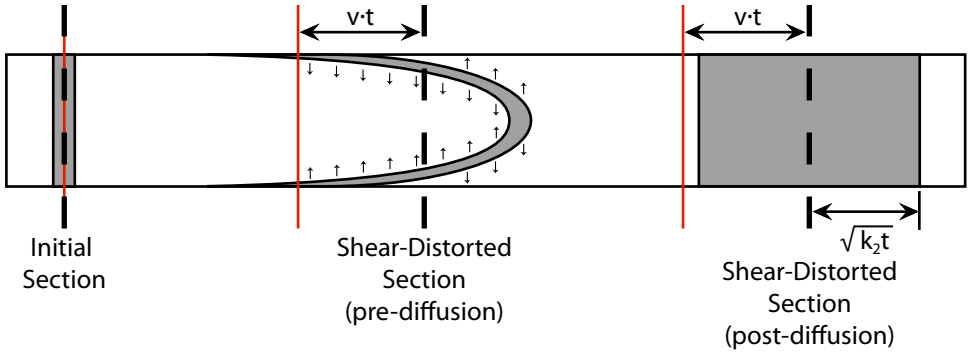

Figure 3.2: A schematic of Taylor dispersion in a microchannel. An initially rectangular cross section is distorted into a parabolic shape by the velocity gradients in the channel, with its center of mass traveling a distance given by the average velocity multiplied by time. The particles diffuse over this increased surface area, crossing streamlines and therefore mixing in the fluid. This mixing and diffusion can be modeled in a one-dimensional system if the particles travel according to the mean velocity and diffuse along the channel with an effective diffusivity greater than that of the solute in a quiescent fluid.

time t. This parabolic shape, as compared to the original cross section, has more area over which particle diffusion can occur, allowing an efficient mechanism for particles to cross streamlines and mix in the fluid stream. The resulting system can be modeled as a one-dimensional channel where the fluid moves at the average velocity of the channel and diffuses with an effective diffusivity k_2 that is greater than the particle diffusivity.

The effective diffusivity of particles diffusing along the length of the channel for use in the one dimensional model is found by considering the diffusion of particles in a steady flow of fluid within the three-dimensional flow in a geometry resembling the system under study. The three dimensional velocity of fluid traveling in the channel is found by solving the momentum equations for low Reynolds number flow, which for this flow can be reduced to

$$\frac{1}{\eta}\frac{dP}{dz} = \nabla^2 u_z \tag{3.2}$$

where P is the pressure and u_z is the three-dimensional velocity component along the length of the channel. The resulting three-dimensional velocity is then used with the continuity equation for the particles in the flow, considering both convection and diffusion. This is given by

$$\frac{\partial C}{\partial t} + u_z \frac{\partial C}{\partial z} = D\left(\nabla^2 C\right) \tag{3.3}$$

where C is the three-dimensional concentration. To find the effective diffusion constant, the above continuity equation is averaged over the cross sectional area of the channel. To assist in this, the three dimensional concentration is expanded from the mean concentration using

$$C = \sum_{n=0}^{\infty} f_n \frac{\partial^n C_m}{\partial z^n} \tag{3.4}$$

where the function f_n is the n^{th} coefficient of the series expansion, and may be a function of time and the spacial coordinates representing distances within the cross section of the channel. The resulting averaged continuity equation then takes the form

$$\frac{\partial C_m}{\partial t} = \sum_{n=1}^{\infty} k_n \frac{\partial^n C_m}{\partial z^n} \tag{3.5}$$

where $k_n(t, z)$ is a collection of terms resulting from the averaging process. Details of the calculation as well as expressions for k_n in the case of cylindrical and rectangular ducts are given in Appendices A and B. For the case of $n = 2$, Equation 3.5 resembles a Fickian diffusion relationship, with k_2 serving as the diffusion coefficient. The functions f_n are then found by using Equation 3.4 in the governing equation for the concentration as given in Equation 3.3 and equating the coefficients of like orders of derivatives of mean concentration with respect to position. The resulting equation is given by

$$\frac{\partial f_n}{\partial t} + \sum_{j=1}^{\infty} k_j f_{n-j} + u_z f_{n-1} = D\nabla^2 f_n \tag{3.6}$$

Thus, the various expressions for k_n are found by solving Equation 3.2 for the velocity and Equation 3.6 for the functions f_n. These functions are then used to determine the values of k_n, of which the result for k_2 is the effective diffusion constant for the system. The actual values for this coefficient depend on the geometries in which the equation is being solved and the corresponding boundary conditions. In general, the solution takes the form

$$k_2 = D\left[1 + \epsilon(z)\right] \tag{3.7}$$

where $\epsilon(z)$ is a positive function of the particle diffusivity, the dimensions of the channel, and the average velocity in the channel which itself may be a function of the position along the channel. The exact form of the effective diffusion constant is solved for a cylindrical duct in Appendix A and for a rectangular duct in Appendix B.

The proposed model of the nanoparticle filling process is a sufficiently accurate description of the filling process, with a few caveats. First, the assumption that there is no velocity at the end of the channel is only an approximation, used to simplify the mathematics, and in reality there will be some evaporative flux through this boundary. Thus, the model may not be completely realistic at the end of the channel. Additionally, the use of an effective diffusivity derived from constant flow in a channel in a channel with a velocity gradient that also exists along the length of the channel is an approximation that is valid only when the velocity gradients along the length of the channel are much smaller than velocity gradients across the channel. Again, this is true only sufficiently far from the end of the channel. Finally, the assumption that the evaporation of solvent through the vapor permeable polymer template occurs at a constant rate that is independent of the concentration of solute is only valid at low concentrations.

3.2 Derivation of the Governing Equations

The concentration of solute in the one dimensional channel as a function of position and time is desired. A continuity equation for the solute can be found by performing a mass balance on an arbitrary control volume in the fluid. This results in

$$\frac{\partial C_m}{\partial t} + \frac{\partial}{\partial z}\left(vC_m\right) = \frac{\partial}{\partial z}\left(k_2 \frac{\partial C_m}{\partial z}\right) \tag{3.8}$$

For the system considered here, the boundary conditions include that the concentration of solute is constant in the ink reservoir at $z = 0$ and that there is no flux of solute through the end of the channel, given by

$$C_m(t, z = 0) = C_0 \tag{3.9}$$

and

$$\left.\frac{\partial C_m}{\partial z}\right|_{z=L_0} = 0 \tag{3.10}$$

The initial condition consists of the channel being completely free of solute, given by

$$C_m(t = 0, z) = 0 \tag{3.11}$$

The average velocity $v(z)$ can be found by performing an integral control volume balance on the channel, with one edge of the control volume at the end of the channel $z = L_0$ where $v = 0$ and the other at an arbitrary location z. This results in

$$v(z) = \frac{q'' P_p}{A}(L_0 - z) \tag{3.12}$$

Using this result with Equation 3.8 results in

$$\frac{\partial C_m}{\partial t} + \frac{\partial C_m}{\partial z}v + \frac{\partial v}{\partial z}C_m = k_2\frac{\partial^2 C_m}{\partial z^2} + \frac{\partial k_2}{\partial z}\frac{\partial C_m}{\partial z} \tag{3.13}$$

$$\frac{\partial C_m}{\partial t} = \frac{q'' P_p}{A}\frac{\partial C_m}{\partial z}(z - L_0) + \frac{q'' P_p}{A}C_m + k_2\frac{\partial^2 C_m}{\partial z^2} + \frac{\partial k_2}{\partial z}\frac{\partial C_m}{\partial z} \tag{3.14}$$

At this point, the above equation and the boundary conditions from Equations 3.9 and 3.10 and the initial condition from Equation 3.11 can be put in dimensionless form. The concentration is scaled using the solute concentration in the ink reservoir $C_m = C_0\bar{C}_m$, the position is scaled based on the length of the channel $z = L_0\bar{z}$, and the time is scaled based on a collection of terms related to the evaporation of solvent given by $t = t_s\bar{t}$ where

$$t_s = \frac{A}{q" P_p} \tag{3.15}$$

The resulting dimensionless equation is

$$\frac{\partial \bar{C}_m}{\partial \bar{t}} = \frac{\partial \bar{C}_m}{\partial \bar{z}}(\bar{z} - 1) + \bar{C}_m + \frac{k_2 t_s}{L_0^2}\frac{\partial^2 \bar{C}_m}{\partial \bar{z}^2} + \frac{t_s}{L_0^2}\frac{\partial k_2}{\partial \bar{z}}\frac{\partial \bar{C}_m}{\partial \bar{z}} \tag{3.16}$$

with boundary conditions

$$\bar{C}_m(\bar{t}, \bar{z} = 0) = 1 \tag{3.17}$$

and

$$\left.\frac{\partial \bar{C}_m}{\partial \bar{z}}\right|_{\bar{z}=1} = 0 \tag{3.18}$$

and initial condition

$$\bar{C}_m(\bar{t} = 0, \bar{z}) = 0 \tag{3.19}$$

The above partial differential equation describes the filling of the channel with solute. This filling stage continues until the maximum concentration of nanoparticles is reached at some point in the channel, stopping the flow of fluid and nanoparticles in that region. At this point, the drying stage begins and the effective length of the channel with respect to nanoparticle self-concentration and fluid flow, $L(t)$, can no longer be considered a constant, but is rather a function of time. The velocity can again be found using an integral control volume analysis, resulting in

$$v(t, z) = \frac{q'' P_p}{A}(L(t) - z) \tag{3.20}$$

Using this result with Equation 3.8 results in

$$\frac{\partial C_m}{\partial t} + \frac{\partial C_m}{\partial z} v + \frac{\partial v}{\partial z} C_m = k_2 \frac{\partial^2 C_m}{\partial z^2} + \frac{\partial k_2}{\partial z} \frac{\partial C_m}{\partial z} \tag{3.21}$$

$$\frac{\partial C_m}{\partial t} = \frac{q'' P_p}{A} \frac{\partial C_m}{\partial z}(z - L(t)) + \frac{q'' P_p}{A} C_m + k_2 \frac{\partial^2 C_m}{\partial z^2} + \frac{\partial k_2}{\partial z} \frac{\partial C_m}{\partial z} \tag{3.22}$$

For the boundary conditions, it is assumed that the channels are filled with solute at the position $z = L(t)$, so that there is no flux of solute at this position. The condition that the concentration of solute in the reservoir remains unchanged. This results in

$$C_m(t, z = 0) = C_0 \tag{3.23}$$

and

$$\left. \frac{\partial C_m}{\partial z} \right|_{z=L(t)} = 0 \tag{3.24}$$

The initial condition requires that the concentration in the channel match the concentration at which the system transitions from the filling regime to the drying regime. Therefore

$$C_m(t = t_d^+, z) = C_m(t = t_d^-, z) \tag{3.25}$$

where t_d^+ is the limit of the time at which the drying stage starts taken from higher values of time, and t_d^- is the limit of the time at which the drying

stage starts taken from lower values of time. These equations can be non-dimensionalized using the same dimensionless variables as used previously, resulting in

$$\frac{\partial \bar{C}_m}{\partial \bar{t}} = \frac{\partial \bar{C}_m}{\partial \bar{z}} \left(\bar{z} - \frac{L(\bar{t})}{L_0} \right) + \bar{C}_m + \frac{k_2 t_s}{L_0^2} \frac{\partial^2 \bar{C}_m}{\partial \bar{z}^2} + \frac{t_s}{L_0^2} \frac{\partial k_2}{\partial \bar{z}} \frac{\partial \bar{C}_m}{\partial \bar{z}} \tag{3.26}$$

with boundary conditions

$$\bar{C}_m(\bar{t}, \bar{z} = 0) = 1 \tag{3.27}$$

and

$$\bar{C}_m \left(\bar{t}, \bar{z} = \frac{L(t)}{L_0} \right) = \frac{C_f}{C_0} \tag{3.28}$$

where C_f is the maximum solute concentration. The initial condition is

$$\bar{C}_m(\bar{t} = t_d^+, \bar{z}) = \bar{C}_m(\bar{t} = t_d^-, \bar{z}) \tag{3.29}$$

3.3 Solute Dispersion in the Zero Diffusion Case

3.3.1 Filling Stage

In the case where diffusion is neglected ($k_2 = 0$), an analytical solution to the governing equations is possible. For the solute filling process, the Equation 3.16 reduces to

$$\frac{\partial \bar{C}_m}{\partial \bar{t}} = \frac{\partial \bar{C}_m}{\partial \bar{z}} (\bar{z} - 1) + \bar{C}_m \tag{3.30}$$

while the boundary and initial conditions are the same as in Equations 3.17, 3.18, and 3.19. The analytical solution to the above equation that satisfies the given boundary condition is found in Appendix C. Briefly, the steady-state solution is first found by solving the differential equation with the time derivative term set to zero. The solution to the time-dependent equation is then found by considering that a fixed volume of fluid entering the system at an arbitrary time will always be subject to the same rate of solvent depletion since there is no diffusion of nanoparticles across the control volume boundary in this case. Such a behavior suggests a form of the solution, which can be verified by substitution into the governing

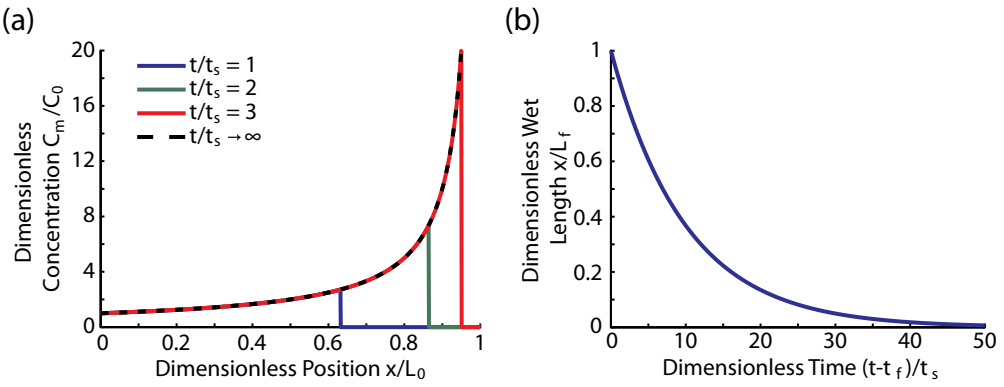

Figure 3.3: Analytical solutions for the case of negligible diffusion, showing (a) concentration as a function of position for various times during the filling stage, and (b) wet channel length as a function of time during the drying stage.

differential equation. The solution to the concentration as a function of position and time is therefore given by

$$\bar{C}_m = \frac{1}{1-\bar{z}} u(1 - \exp(-\bar{t}) - \bar{z}) \tag{3.31}$$

where $u(\zeta)$ represents the unit step function. The solution to the concentration as a function of time is plotted in Figure 3.3. It is seen that, at any time, the concentration profile traces the steady state concentration profile, with a sharp drop to zero at a position in the channel which is dependent on time.

3.3.2 Drying Stage

The filling stage continues as described above until the channel fills completely with solute at some area. Once this maximum concentration is reached, the drying stage begins. This transition occurs at a time t_f that can be determined by equating concentration in the filling stage solution to the saturation concentration of solute, denoted symbolically as C_f. This maximum concentration is achieved at a position of L_f , which is different from the length of the channel L_0 as a result of the zero diffusion assumption as well as the assumption that there is no evaporative flux through the end of the channel. The calculation of the position and time of the transition to the drying stage is performed in Appendix C, resulting in

$$L_f = L_0 \left(1 - \frac{C_0}{C_f}\right) \tag{3.32}$$

$$t_f = t_s \ln \left[\frac{C_f}{C_0}\right] \tag{3.33}$$

In the case where diffusion is neglected ($k_2 = 0$) the Equation 3.26 reduces to

$$\frac{\partial \bar{C}_m}{\partial \bar{t}} = \frac{\partial \bar{C}_m}{\partial \bar{z}} \left(\bar{z} - \frac{L(\bar{t})}{L_0}\right) + \bar{C}_m \tag{3.34}$$

The boundary conditions that must be satisfied by the solution are given by Equations 3.27 and 3.28 and the initial condition by Equation 3.29. The equation may be further simplified in the case that the drying is a quasi-steady process. In this case, the magnitude of the time derivatives of concentration in Equation 3.34 are small in comparison to the other terms in the equation. In the drying stage, these time derivatives of concentration must be driven only by the fact that the length of the channel is a function of time. Considering a mass balance on the system, this term will be small provided that the maximum concentration in the channel is much larger than the initial concentration ($C_f >> C_0$). Therefore, the fundamental equation becomes

$$\frac{\partial \bar{C}_m}{\partial \bar{z}} \left(\bar{z} - \frac{L(\bar{t})}{L_0}\right) + \bar{C}_m = 0 \tag{3.35}$$

However, the equation given above is only a first order differential equation in the concentration. This means that only one boundary condition on the concentration can be satisfied, when in reality the concentration is fixed on either side of the channel. A simple adjustment can be made to the equation, which is the equivalent to enabling some flux of solvent to evaporate through the end of the channel. This is done by replacing the length of the channel $L(\bar{t})$ by an effective length represented by $L_x(\bar{t})$, where $L_x(\bar{t}) > L(\bar{t})$. The use of an effective length enables the boundary conditions at both ends of the channel to be satisfied. The equation therefore becomes

$$\frac{\partial \bar{C}_m}{\partial \bar{z}} \left(\bar{z} - \frac{L_x(\bar{t})}{L_0}\right) + \bar{C}_m = 0 \tag{3.36}$$

The solution to the above equation may be found by simple integration. The boundary condition on the left end of the channel is used to find the constant of integration, and the boundary condition on the right side of the

channel is used to find the relationship between $L_x(\bar{t})$ and $L(\bar{t})$. At this point, a control volume balance is used to relate the time rate of change of the mass of solute in the control volume to the flux of solute through the inlet to the channel. This mass balance is used to find the wet length of the channel as a function of time, $L(\bar{t})$, which is the desired result. The details of this calculation are given in Appendix C, resulting in

$$L(\bar{t}) = L_f \exp\left(-\frac{C_0}{C_f}\frac{t - t_f}{t_s}\right) \tag{3.37}$$

The solution to the wet length as a function of time is plotted in Figure 3.3. It is seen that the wet channel length decreases at slower rates as the drying process progresses, asymptotically approaching the full channel length at long times.

3.4 A Numerical Solution to the Solute Dispersion Problem

In actual operation, the solute in the ink is subject to random forcing and therefore motion that results in solute diffusion. The analytical solution described above neglects diffusion, and therefore has only limited applicability to a real system. However, such an analytical solution is not possible when the extra diffusion terms are included in the governing equation. Therefore, a numerical solution must be developed.

Similar to the analytical solution, the process is broken into a filling and a drying stage, depending on whether the maximum concentration of nanoparticles has been reached at any point in the channel. For the filling stage, the fundamental equation is given in Equation 3.16 with boundary conditions given in Equations 3.17 and 3.18 and an initial condition described by Equation 3.19. For the drying stage, the fundamental equation is given in Equation 3.26 with boundary conditions given in Equations 3.27 and 3.28 and an initial condition described by Equation 3.29. The diffusion coefficients for the system, represented by k_2, are found by considering the Taylor dispersion of solute due to the velocity gradients in the full, three-dimensional system. The process of obtaining these coefficients, along with the exact form of the coefficients, are described in Appendix A for a cylindrical duct and Appendix B for a rectangular duct.

The numerical solution is obtained by discretizing the governing equation using a finite difference method. The time derivatives are approximated

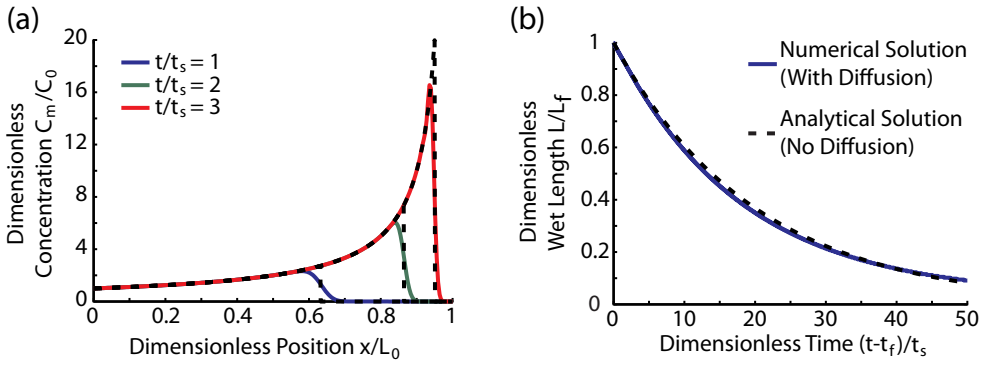

Figure 3.4: Numerical solutions, including diffusion, for (a) concentration as a function of position for various times during the filling stage, and (b) wet channel length as a function of time during the drying stage. For each, the corresponding analytical solutions are shown as black dotted lines.

using a forward difference, contributing to the simplicity and stability of the solver. Spatial derivatives are approximated using a center difference when possible, and either forward of backward derivatives for points at the ends of the channel. At each point, a diffusion coefficient is calculated using the analytical solution for the velocity at that location as given in Equation 3.12. When necessary, spatial derivatives of the diffusion coefficient are calculated using similar finite difference methods. The accuracy of the solver is ensured by using a sufficiently small spacing in both time and position.

The results for the concentration as a function of position and time for a square duct, along with the equivalent solutions from the no-diffusion analytical solution, are shown in Figure 3.4. It is seen that the results from the numerically obtained solution closely follow the analytical solution, except that steep concentration gradients in the analytical solution are smoothed out by the finite diffusion in the system. The results for the numerically obtained wet length of the channel as a function of time during the drying stage is also given in Figure 3.4, along with the equivalent analytical solution. It is seen that these two solutions are nearly indistinguishable, showing that diffusion has little effect on the drying of the channels.

While the actual process described here uses a square duct, the solution for the dispersion coefficient is significantly simplified by using the dispersion coefficient for a cylindrical duct. That is, the square duct solution contains numerous nested infinite sums which must be evaluated with a sufficiently high number of terms in order to get a sufficiently accurate value for the dispersion coefficient. Since, in general, there is a different

velocity at each point in the channel and at any given time, this coefficient must be calculated many different times. The computational complexity of the numerical solution can be reduced by using the explicit solution for a cylindrical duct, using the hydraulic radius R_h of the rectangular duct that is given by

$$R_h = \frac{bh}{b+h} \tag{3.38}$$

where b is the width and h the height of the square channel. The error incurred by approximating the dispersion coefficient using a cylindrical channel is small, provided that the width and height of the channels are nearly equal, as shown in Figure 3.5 for a square channel. As the aspect ratio of the channel differs from 1:1, the error in the approximation increases. This is shown in Figure 3.5, where the aspect ratio of a rectangular channel is changed while keeping the cross sectional area of the channel the same. Aspect ratios that are farther from 1:1 exhibit decreased levels of Taylor dispersion, on account of the increased presence of the wall and corresponding lower overall velocity gradients.

3.5 Experimental Verification of the Solute Dispersion Model

To verify the applicability of the models described above, the filling process was observed experimentally and compared to the numerical model described above. The filling was performed using an ink consisting of 3.5 wt% of gold nanoparticles with a hexanethiol monolayer in an alpha-terpineol solvent. The channels were initially filled with clean alpha-terpineol. The gold nanoparticles were chosen due to their high visibility in the ink, and the solvent for its low vapor pressure and therefore slow evaporation speed. The filling process was performed at a constant temperature of 75°C. During the filling process, optical images were taken using a Canon 5D Mark II camera with a Canon EF 100 mm f/2.8 macro lens with a working distance of 8 cm. Continuous video was taken of the filling process, and the video was subsequently split up into individual frames for analysis. Three such frames are shown in Figure 3.6. The resulting images were analyzed using Matlab (MathWorks) to convert the images to grayscale and subtract the background from the images. ImageJ was used to analyze the average intensity of the light in the images along the microchannels.

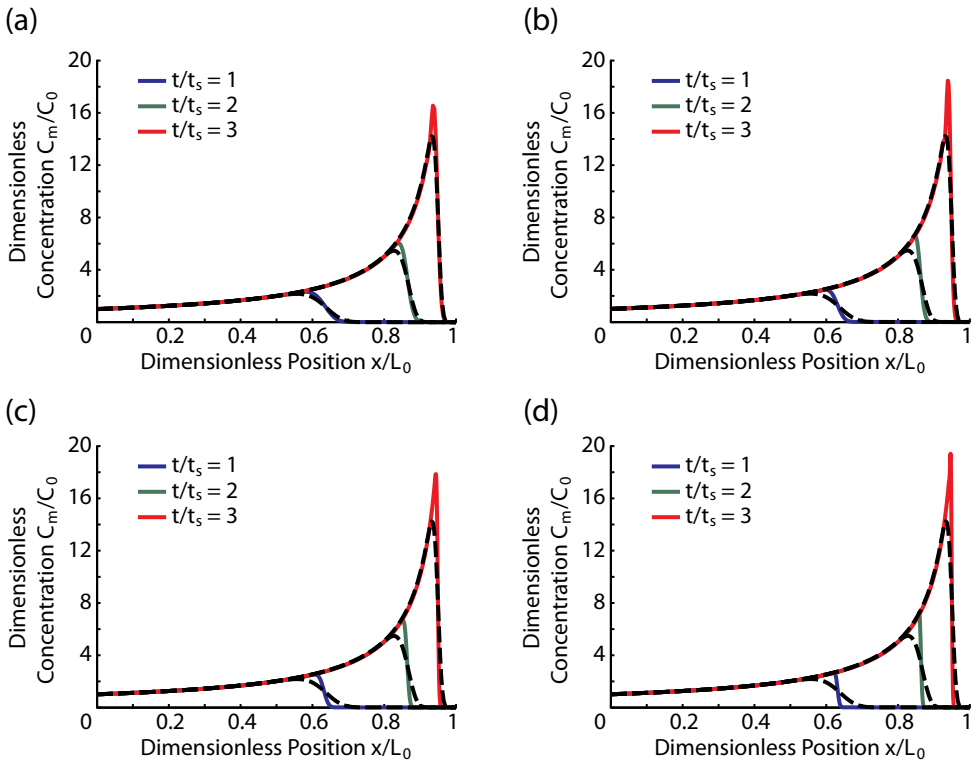

Figure 3.5: Numerical solutions for solute concentration as a function of position at various times for a rectangular (colored lines) and cylindrical (black dotted lines) channel with equivalent cross sectional area, for (a) 1:1 aspect ratio, (b) 2:3 aspect ratio, (c) 1:2 aspect ratio, and (d) 1:3 aspect ratio.

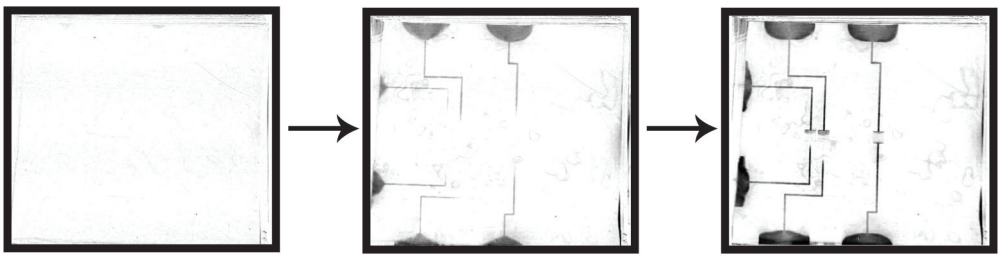

Figure 3.6: Optical images of the template filling with nanoparticle ink at three different times.

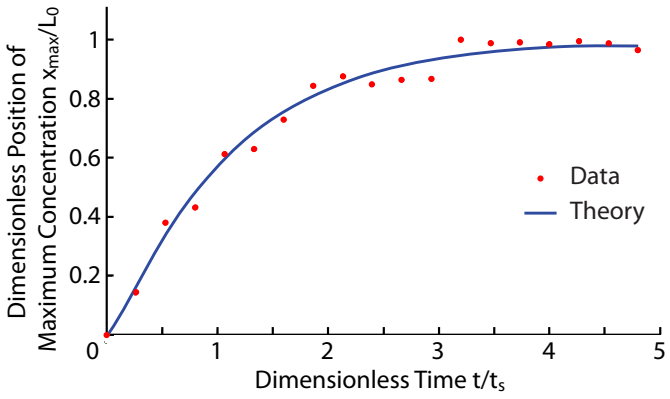

Figure 3.7: A comparison of the experimental results for the position of maximum concentration versus time to the theoretical model.

It is known that the light intensity is related to the nanoparticle concentration, with darker areas containing more nanoparticles. However, the light intensity is not necessarily directly proportional to the solute concentration. Since the location of the maximum light intensity is easily tracked and corresponds identically to the location of the maximum nanoparticle concentration, the location of the maximum light intensity was tracked and plotted as a function of time.

The experimental results were compared to the results from the numerical model developed previously. The model used here was for solute dispersion in a cylindrical channel, chosen because of the computational simplicity as compared to the solution for a rectangular duct. Since the channel had an aspect ratio of nearly 1:1, the error in using this approximation is small. The inputs to the numerical model are all known from the experimental system except for the evaporation rate of the solvent, which is contained in the time constant term. This time constant was found by minimizing the least squared error between the theory and data. For the experimental data here, the time scale was found to be approximately $t_s = 31s$.

The comparison between the theory and the experimental data is shown in Figure 3.7. There is a strong agreement between the two curves, suggesting that the proposed model is indeed an accurate representation of the actual system.

3.6 Viscous Pressure Drop in the Channel

The patterning process consists of a reservoir that is kept at atmospheric conditions and a channel in which flow is driven by evaporation. Viscous losses in the moving fluid create a pressure drop across the length of the channel, resulting in a pressure inside the channel that is lower than the atmospheric pressure seen in the reservoir. These viscous losses are especially important due to the fact that the viscosity of the nanoparticle or polymer ink increases exponentially with increasing solute concentration, enabling potentially high pressure gradients.[105–107] Such pressure drops, coupled with the finite modulus of elasticity of the templates, can lead to a loss in fidelity of patterned features. As will be discussed in Chapter 4, such a loss in patterning fidelity can be especially pronounced when PDMS is used as the template material due to its low Young's modulus.

In this section, the pressure drop in the template is evaluated. The channels are modeled as having a circular cross section using the hydraulic radius as given in Equation 3.38 due to the simplicity of the resulting analysis and the fact that it is a reasonable approximation to the rectangular cross section used in the actual templates.[108] Additionally, the one dimensional model with no diffusion is used as the model for the concentration of solute in the channel, again due to the simplicity of the model and its reasonable level of accuracy. To complete the analysis, the viscosity of the ink must be determined as a function of the concentration, followed by the pressure as a function of position and time. The resulting pressures can be used to evaluate the template distortion using a finite element model of the template.

3.6.1 Viscosity Variation with Solute Concentration

Both nanoparticle and polymer inks are known to vary as a function of solute concentration in an approximately exponential manner.[105–107] However, to increase the accuracy of the model, the viscosity can be measured experimentally as a function of concentration. This is done for cellulose acetate polymer in NMP using a capillary flow viscometer. Briefly, pressurized air is used to drive the fluid to be measured through a capillary of known dimensions. The fluid exiting the capillary is collected in on a balance, allowing the weight of fluid to be monitored as a function of time. The known actuating pressure and the measured mass flow rate can be used to calculate the fluid viscosity using the Hagen-Poiseuille equation.[108]

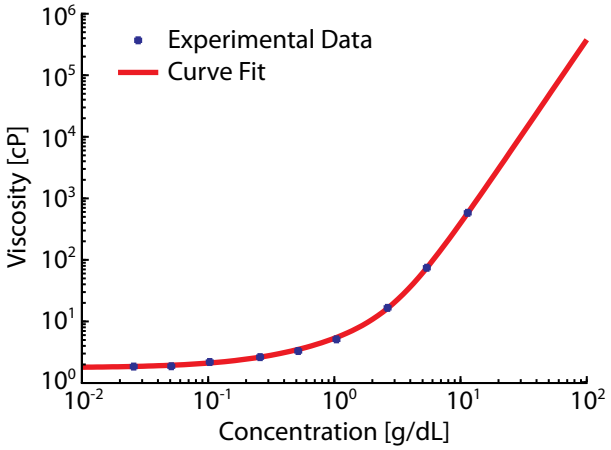

Figure 3.8: Viscosity of cellulose acetate in NMP as a function of concentration.

After calibrating the system by measuring the known viscosity of deionized water, the capillary viscometer was used to measure the viscosity of the ink as a function of solute concentration. First, the clean NMP was measured, resulting in a viscosity of 1.76 cP. This measured viscosity differs from that reported on the datasheet supplied by 3.85%, which is within an acceptable margin of error. Next, the viscosities of various concentrations of cellulose acetate in NMP were measured. These results, which are shown in Figure 3.8, confirm that the viscosity increases sharply with increasing concentration. For use in the determination of the pressure in the microchannel, an empirical relation is developed by performing a least-squares regression on a third-order polynomial. The resulting relation is

$$\eta(C_m) = 0.38C_m^3 - 0.19C_m^2 + 3.36C_m + 1.77 \tag{3.39}$$

where the viscosity η has units of cP.

3.6.2 Pressure Versus Position and Time

With the viscosity as a function of concentration known, a model for the pressure drop due to fluid flow in the channel can be determined. For a cylindrical channel, the average velocity in the channel is shown in Appendix A to be

$$U_{avg} = \frac{R_h^2}{8\eta}\frac{dP}{dz} \tag{3.40}$$

The average velocity in the channel is equivalent to the velocity in the one-dimensional model, given in Equation 3.12. Substituting and solving for the pressure gradient results in

$$\frac{dP}{dz} = \frac{8P_p q"}{AR_h^2}\eta(L-z) \tag{3.41}$$

In terms of the dimensionless variables used previously, this becomes

$$\frac{1}{L}\frac{dP}{d\bar{z}} = \frac{8L}{t_s R_h^2}\eta(1-\bar{z}) \tag{3.42}$$

$$\frac{dP}{d\bar{z}} = \frac{8L^2}{t_s R_h^2}\eta(1-\bar{z}) \tag{3.43}$$

At this point, it is convenient to define a dimensionless pressure as $\bar{P} = P/P_0$ where $P_0 = (8L^2\eta_0)/(R_h^2 t_s)$ and η_0 is the viscosity of the bare solvent. Physically, the scaling factor P_0 represents the pressure loss in the channel that would exist if only clean solvent moved at the maximum flow rate throughout the entire channel. This results in

$$\frac{d\bar{P}}{d\bar{z}} = \frac{\eta(\bar{z})}{\eta_0}(1-\bar{z}) \tag{3.44}$$

The pressure in the channel may be determined by integrating the above pressure gradient using the expression for the viscosity as a function of concentration from Equation 3.39 and concentration as a function of position from Equation 3.31. The resulting pressure as a function of position at various times for an ink with an initial concentration of 1% is shown in Figure 3.9(a). Here, the time is non-dimensionalized based on the time taken to reach the maximum pressure drop in the channel, as given by Equation 3.33. At time $t/t_f = 0$ the pressure in the channel is simply due to flow of clean solvent in the channel, while at time $t/t_f = 1$ the pressure is due to flow of ink with a concentration that increases along the channel length. Intermediate times show a concentration profile resulting from both ink and clean solvent existing in the channel at different locations.

The physical origin of the viscous losses suggests a potential method for reducing the magnitude of the negative pressure in the channels. Given that the pressure gradients are linearly dependent on viscosity and the viscosity is a strong function of concentration, the onset of the high viscosity region of fluid can be delayed until closer to the end of the channel by reducing the initial concentration of the ink. The variation in the maximum pressure drop across the channel is plotted as a function of initial ink concentration

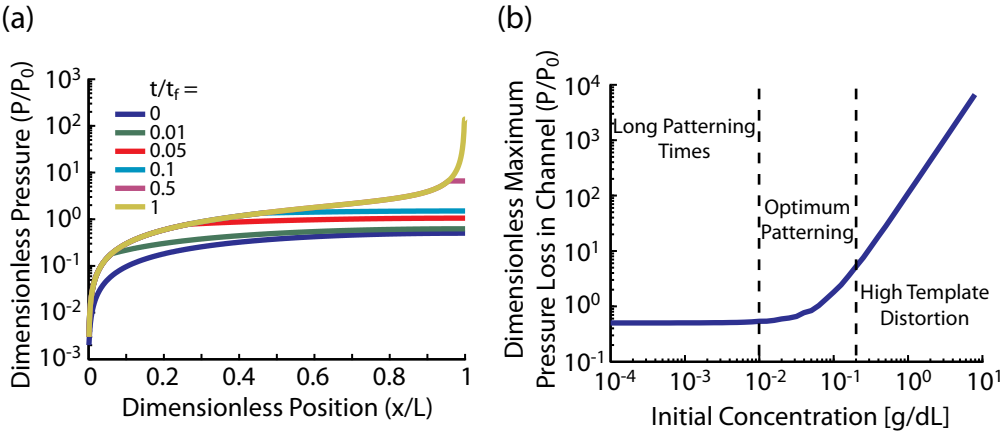

Figure 3.9: (a) Dimensionless pressure loss in the channel as a function of dimensionless position at various times for cellulose acetate in NMP with a 1% initial concentration. (b) Dimensionless pressure loss in the channel as a function of initial concentration for cellulose acetate in NMP, illustrating the trade-off that exists between patterning speed and dimensional distortion.

in Figure 3.9(b). At higher concentrations, the maximum pressure drop increases rapidly with increasing concentration, suggesting that high levels of template distortion could result in this region. At low concentrations, the pressure drop becomes independent of initial concentration, suggesting that any reduction of initial concentration in this region will increase patterning time without any corresponding reduction in template distortion. An optimum range of initial concentrations exists between these two extremes, where an appropriate balance between patterning time and dimensional fidelity can be achieved.

3.6.3 Template Distortion due to Pressure

Pressure differences in the channels will result in some elastic deformation of the template, causing discrepancies between designed and actual dimensions of patterned features. To provide an understanding of this phenomenon, a finite element model of the template is used together with the previously created pressure model to determine the magnitude and shape of this template distortion, which can then be verified by comparing the model to SEM images of actual patterned features.

In the finite element model, the template is approximated using alternating channels containing two different inks which are separated by a spacing equal to the width of the patterned features, as shown in Figure 3.10, which

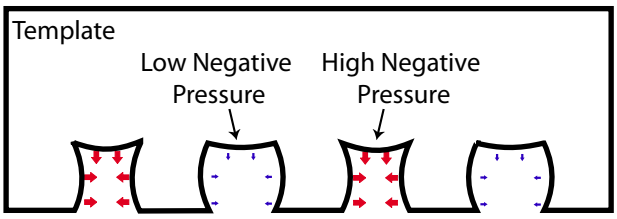

Figure 3.10: A schematic illustration of the finite element model. Alternating channels contain a similar ink with different initial concentrations, which lead to different pressures in the channels. This pressure difference can cause deformations in the channels due to bending of the wall separating the channels.

approximately matches the geometry of the templates used in the subsequent experiments. The inks used are presumed to be of the same materials but with a different initial concentration of solutes, resulting in two negative pressures of different magnitude inside these alternating channels.

A qualitative comparison of the finite element model and the experimental results, given in Figures 3.11(a) and (b), shows excellent agreement. The physical dimensions of the patterned features from the channels containing the more concentrated ink are smaller than those on the template, due to the bending of the walls between adjacent channels caused by the differential negative pressure. Conversely, the dimensions of features from channels containing the lower concentration ink are larger than those on the template, due to bending of the walls away from the channel with the higher pressure.

To quantify the magnitude of the deformation due to the flow of viscous ink in the template, the finite element model was used to find the dimensional distortion of features as a function of the pressure difference between adjacent channels. The result, given in Figure 3.11(c), shows that the dimensional distortion increases proportionally with the pressure difference between the two sets of channels. If the intent of the template is to have the patterned features be the size of the template, care must be taken to ensure that the magnitude of the pressure difference between adjacent channels remains sufficiently low, which can be done by either using ink with matched physical properties or by using inks with a sufficiently low initial concentration.

The validity of the pressure as a function of initial concentration was demonstrated experimentally by patterning two different concentrations of cellulose acetate ink in close proximity to a gold nanoparticle ink, which

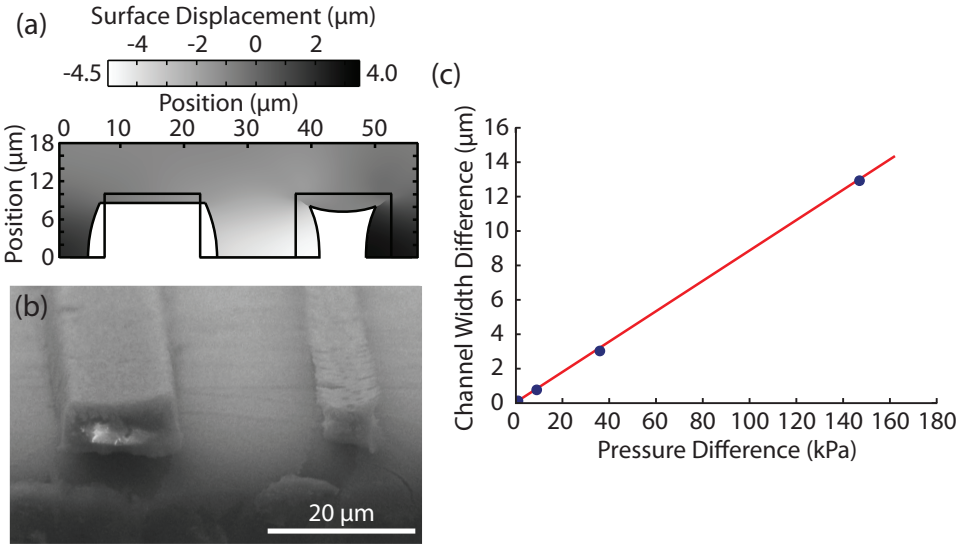

Figure 3.11: (a) Finite element results for template deformation. The deformed surface is 1:1 scale, and the black lines are the undeformed shape. The surface is colored by x-displacement in μm. (b) SEM image of the experimental results using the same conditions as given in the finite element model, showing good qualitative agreement. (c) The channel width difference as a function of pressure difference from the solid model.

was kept at a constant initial concentration, on a polyimide substrate. The results, shown in Figure 3.12, demonstrate that a lower initial concentration of the cellulose acetate ink results in more similar dimensions between the gold and polymer lines, while use of higher concentration ink leads to a greater difference in dimensions between channels containing the two materials, which is as predicted by the above model.

3.7 Analysis of Results

The resulting models of the system provide important insight into the operation of the patterning system. These insights are listed below:

1. **Solute flux is driven mainly by convection.** A comparison between the numerical solution which contains diffusion and the analytical solution which assumes negligible diffusion, as was shown in Figure 3.4, shows that the resulting concentration profiles are nearly identical in most locations. The effect of diffusion is to smooth out steep concentration profiles located at the interface between the solute-containing

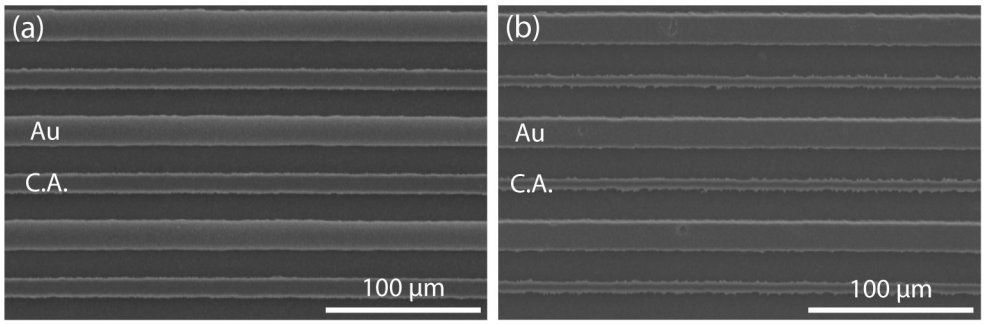

Figure 3.12: SEM micrographs of gold nanoparticle and cellulose acetate polymer lines, with (a) low concentration (0.2%) and (b) high concentration (1.0%) cellulose acetate ink. Higher pressure losses due to more rapid increases in viscosity of the drying polymer ink cause a larger distortion of features patterned with the higher concentration ink.

fluid and the solvent-free fluid. This suggests that the speed of the patterning process can be controlled simply by adjusting the evaporation rate of the solvent, such as by changing the system temperature or solvent vapor pressure in the surrounding environment. Additionally, enhancements to the processing speed of the system can by envisioned by changing the configuration of the template to maximize solvent diffusion through the vapor permeable polymers, lowering the time constant in a manner that is independent of the geometry of the template features.

2. **Diffusion is stronger at the inlet and weaker at the end of the channel.** The concentration gradient that exists at the interface of the fluid containing solute and the fluid without solute is steeper at the end of the channel than toward the inlet to the channel, as seen in Figure 3.4. This is due to the Taylor dispersion of solute being stronger closer to the inlet of the channel, on account of the higher average velocity and thus the larger velocity gradients at this location. This means that solute can efficiently concentrate at the end of the channel, bringing one single location to the saturation concentration while maintaining a strong concentration gradient which can prevent premature clogging in the channel at other locations.

3. **The location at which the maximum concentration is first reached is dependent on the concentration of solvent in the reservoir.** This can be seen clearly in Equation 3.32. The concentra-

tion of the ink should be sufficiently low as to not reach the saturation solute concentration before reaching the end of the channel. However, to maximize patterning speed, higher concentration inks are often desirable.

4. **Solute fills the channel smoothly from the end of the channel toward the inlet.** As the channel dries, there exists a persistent steep concentration gradient immediately prior to the dry location. As a result, the wet length of the channel smoothly and continuously decreases as the solvent dries, as seen in Figure 3.4. This ensures that all of the channel fills uniformly with solvent, preventing formation of any unwanted cracks or defects in the resulting pattern. Additionally, the wet length in the channel decreases quickly at first, gradually and asymptotically approaching zero. This behavior suggests that increased speed in patterning can be obtained by either using additional runway on the length of features which need not be filled with particles, or by increasing the concentration of ink in the reservoir during patterning to decrease the amount of solvent that must be removed from the ink to dry it in a decreased channel length.

5. **The pressure drop along the length of the channel may be controlled by the initial ink concentration.** High pressure drops can lead to distortion of the template, especially for templates with a lower modulus of elasticity. These pressure drops are due to the large increase in viscosity of the polymer and nanoparticle inks with increasing solute concentrations. However, such pressure losses and corresponding feature distortion can be controlled by adjusting and optimizing the initial solvent concentration.

Chapter 4

Advanced Template Materials for High Quality Patterning

A major limiting factor for high-resolution, three-dimensional patterning of polymers and nanoparticles in the process under development here is the templates used for molding the materials. In the current process, a change in the rheology of the ink is accomplished by simple evaporation of the carrier solvent through the template. Polymers with a high vapor permeability are ideal template materials as they allow solvent molecules to diffuse through the template without allowing passage of the solute. Currently, poly(dimethylsiloxane) (PDMS) is used as the template material, due to its common availability. However, while this material has sufficient vapor permeability for the patterning, its low modulus of elasticity and tendency to swell when exposed to solvents limits the attainable resolution, alignment, and structural fidelity. To solve this problem, a highly rigid, chemically robust, optically transparent and vapor-permeable poly(4-methyl-2-pentyne) (PMP) template is developed. This material was cast into templates having both microscale and nanoscale features, and then used to pattern a variety of nanoparticles and polymers. Using this template material, a resolution of better than 350 nm was achieved. The patterned features exhibit high dimensional fidelity with excellent control over all three dimensions.

In this chapter, the limitations of the current PDMS templates will be discussed, motivating the need for a new vapor permeable polymer material. Current vapor permeable polymer materials will be reviewed, and a template material will be selected. The process of synthesizing and casting

the selected polymer to form the required patterning templates will then be described. Finally, results and discussion of the patterning process using this new template material will be presented.

4.1 Limitations of Poly(dimethylsiloxane) Templates

As mentioned previously, the physical properties of PDMS limit the attainable resolution, patterning fidelity, and alignment capability of the patterning process. These limitations are cause by the low Young's modulus of the material and its tendency to swell when exposed to various solvent. The low Young's modulus of PDMS causes high levels of distortion of the features with applied pressure. This pressure includes both the slight pressure used to ensure good conformal contact between the template and the substrate, as well as pressure from gradients formed by evaporation of solvent through the template and the corresponding flow of fluid through the template features. As discussed in Chapter 3, these fluidic pressured can be quite large due to the rapid increase in viscosity of nanoparticle and polymer inks with increasing solute concentration.[105–107] Since the fluid flow is driven by evaporation and mass loss, the pressure inside the template features is less than atmospheric. Therefore, both the externally applied pressure and the internal fluidic pressure both act to diminish the size of features. Additionally, PDMS is known to swell when exposed to various solvents, which can in some cases cause substantial distortion.[92] Like the distortion due to pressure, this swelling also causes features to diminish in size.

The problems associated with the distortion of the PDMS templates can be seen in the resulting patterns created with these templates, as shown in Figure 4.1. The features appear distorted, bowing in on the sides and the top. The dimensions of features are different from those patterned originally in the template, and sufficiently small features tend to pinch shut completely, limiting the ultimate resolution of the process. Poisson expansion of the template also tends to distort the template, limiting alignment capability over large areas. Additionally, since the factor determining the template distortion are different for different materials and solvents, the attainable resolution also varies depending on the specific ink chemistry used. For example, an aqueous solvent was used to pattern chitosan with a resolution of smaller than 5 μm, while patterning cellulose acetate with an organic NMP solvent is limited to a minimum feature size of approximately

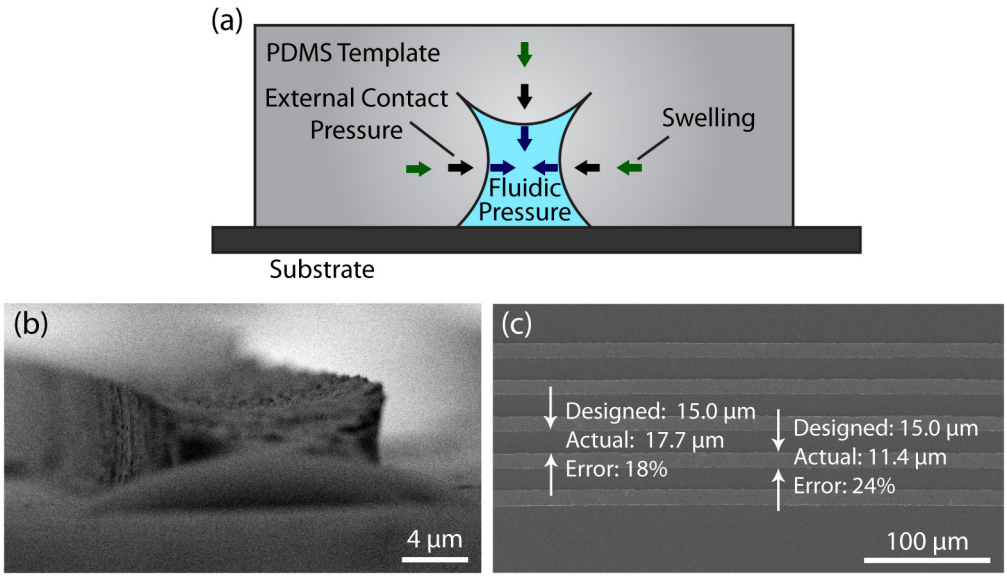

Figure 4.1: (a) The PDMS template is prone to distortion due to fluidic pressure forces, external pressure forces, and swelling by solvents. (b) A side view of gold nanoparticles on a polyimide substrate showing the distortion of the feature. (c) A top view of gold nanoparticles on a polyimide substrate showing the loss in dimensional fidelity due to template distortion.

15 μm due to the danger of smaller features being completely pinched off at some points due to template distortion.

4.2 Material Requirements for Templates

As the patterning process is driven by evaporation of solvents through a vapor permeable template, a high vapor permeability is paramount. The vapor permeability should ideally be as high as possible. However, the material should be non-porous to prevent fouling of the surface with solute, in order to ensure long template lifetimes. However, in addition to vapor permeability, high rigidity is also desired in order to prevent warping and distortion of the template as seen when using PDMS. Since the template is used to pattern a variety of materials dispersed in many different solvents, the template material should be compatible with many different solvents. The material must be able to be formed with microscale and nanoscale features, preferably by replication from a pre-fabricated master, enabling many polymer templates to be created from a single lithographically-created master. Since the evaporation of solvent is often assisted by increased temper-

atures, the template should have good thermal stability with a high glass transition or breakdown temperature. The template must also have sufficiently low surface energy, promoting good release of patterned features from the template. Finally, optical transparency is desired for simplified alignment between the templates and existing features on the substrate.

4.3 Vapor Permeable Polymers as Template Materials

Vapor permeable polymers have been studied extensively for application as membranes in gas separations.[109–111] These vapor permeable polymer materials all possess a high fractional free volume, which allows gas molecules to easily diffuse through the polymer matrix.[109] Of these polymers, those with the highest gas permeabilities are the substituted polyacetylenes,[109] a few examples of which are shown in Figure 4.2. This class of polymers consists of alternating double and single bonds in an all-carbon backbone, similar to poly(acetylene), but with other side chains substituted in at locations which in poly(acetylene) would normally contain only hydrogen. The carbon-to-carbon double bonds prevents rotation of the backbone at these locations, providing rigidity to the polymer. Bulky side groups are then desired for the substitutions, which serves to hinder rotation of the polymer backbone around the single bonds. The inflexible nature of the polymer backbone forces the polymer into rigid, randomly coiled structures, preventing efficient packing and crystallization of the polymer. This poor packing leads to the high fractional free volume in the bulk polymer which provides the high vapor permeability.[109]

The nature of these vapor permeable polymers is still a topic of active research. Using the simple operational principle given above, it stands to reason that larger, bulkier side chains could more efficiently prevent rotation about the single carbon-to-carbon bond and prevent packing of the polymer chains. However, this is not always the case, and, as shown in Figure 4.2 and Table 4.1, a material with a much more substantial side chain does not necessarily result in a more vapor permeable polymer.[112,113]

Currently, the polymers with the highest vapor permeabilities are indan-based polyacetylenes, shown schematically in Figure 4.2. These rigid, glassy polymers contain both an indan group and a phenyl group as substitutions on the polyacetylene backbone, both of which are very bulky.[112] The resulting vapor permeability for common gasses is quite high, as shown in Table

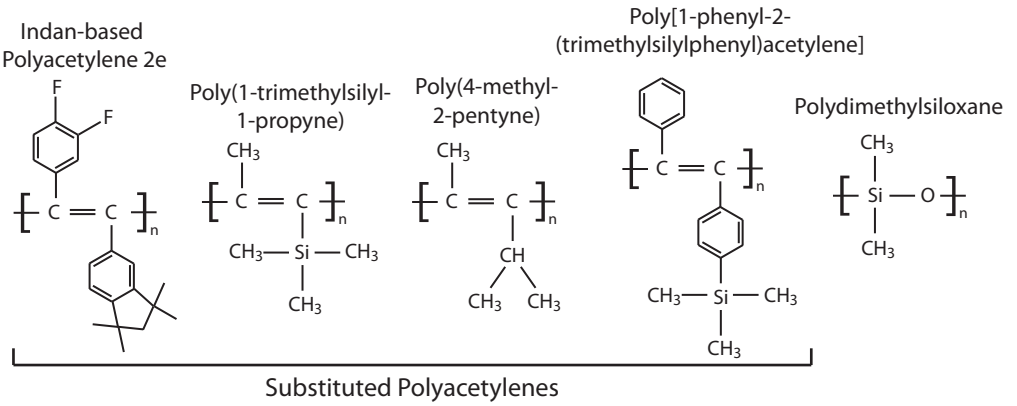

Figure 4.2: Chemical structures of various polymers discussed in the text, listed from left to right in order of decreasing average gas permeability.

	Gas Permeability (Barrer)				
Gas	Indan-Based Polyacetylenes	PTMSP	PMP	PTMSDPA	PDMS
H_2	36800	17000	5800	2600	890
N_2	16600	6300	1300	560	400
O_2	36800	9700	2700	1200	800
CO_2	44200	34000	11000	4900	3800
CH_4	35000	15000	2900	1600	1200
C_2H_6	-	26000	3700	2700	3300
C_3H_8	-	32000	7300	4400	4100
n-C_4H_{10}	-	102000	26000	20000	16000
References	112	114	114	114	115,116

Table 4.1: Permeabilities of various polymers to some common gasses.

4.1. However, since these materials have only been discovered relatively recently, there is still substantial room for improvement in the synthesis procedure as well as much work remaining in characterization of the polymer, limiting their applicability to the current process temporarily.

Other substituted polyacetylenes include poly(1-trimethylsilyl-1-propyne) (PTMSP) and poly(4-methyl-2-pentyne) (PMP), shown schematically in Figure 4.2. It is noted that in both PTMSP and PMP, the side chains can exist in both *cis*- and *trans*- configurations about the carbon-to-carbon double bond. This *cis/trans* isomerism can be controlled using different catalysts during the polymer synthesis.[109] Like the indan-based polyacetylenes, these polymers are rigid and glassy, having high fractional free volumes and possessing very high vapor permeabilities.[111] The struc-

	Solubility			
Solvent	Indan-Based Polyacetylenes	PTMSP	PMP	PDMS
cyclohexane	X	X	X	O
toluene	X	X	O	O
chloroform	X	X	O	O
tetrahydrofuran	X	X	O	O
dimethylformamide	O	O	O	O
methanol	O	O	O	O
n-heptane	-	X	O	O
carbon tetrachloride	-	X	X	O
acetone	-	O	O	O
methyl ethyl ketone	-	O	O	O
n-methylpyrrolidone	-	O	O	O
References	112	117–120	121	92

Table 4.2: Solubility of various vapor permeable polymers in common solvents. X = soluble, O = insoluble, - = no data available.

ture of these materials is similar to the indan-based polyacetylenes, but with different side chain configurations. The resulting vapor permeabilities for some common gasses are shown in Table 4.1. Additionally, the solvent compatibilities for these polymers is given in Table 4.2. While PTMSP contains a higher vapor permeability, PMP is substantially more chemically robust. Additionally, since PMP consists exclusively of carbon and hydrogen atoms, the polymer has a low surface energy that promotes good release of patterned materials from the template, preventing fouling of the surface and extending template lifetimes.[121,122] The polymer has no glass transition temperature, enabling its usage at elevated temperatures, and is optically transparent, allowing registration by optical alignment.

4.4 Poly(4-methyl-2-pentyne) Synthesis, Characterization and Casting

4.4.1 Polymer Synthesis

Poly(4-methyl-2-pentyne) was synthesized following the method of Morisato et al,[121] which in turn follows that developed by Masuda et al.[123] Details of the synthesis procedure are given in Appendix D. Briefly, a monomer solution is prepared by dissolving 4-methyl-2-pentyne in toluene. A separate

catalyst solution is prepared by dissolving niobium pentachloride and triphenyl bismuth in toluene. The catalyst solution is heated, and the monomer solution added dropwise while stirring vigorously. The polymerization reaction occurs by coordination polymerization, whereby units of monomer are added to the growing polymer chain through an organometallic active site. Coordination polymerization is a form of addition polymerization, where no initiator is necessary and no reaction byproduct is formed. It is noted that all processing steps above are done in a nitrogen environment due to the tendency of niobium pentachloride to hydrolyze when in the presence of oxygen. Following polymerization, the gelled polymer is dissolved in solvent and then precipitated and filtered, several times, to remove the catalyst. The filtered polymer is then dissolved in cyclohexane to a concentration of approximately 1% for subsequent processing. The resulting yield of the polymerization reaction and filtering was approximately 63%.

4.4.2 Properties Characterization

Following synthesis, the structure of the synthesized polymer was confirmed using Fourier transform infrared spectroscopy (FT-IR). Some polymer was cast onto a silicon wafer, using the method described below, which was then analyzed. The resulting spectrum, shown in Figure 4.3, matches well to those reported in the literature,[121,123] indicating that the polymer was indeed synthesized correctly. Additionally, the cast PMP polymer had a measured density of 7.3 ± 0.9 g/m^3 and a water contact angle of approximately 105°, which is similar to previous works.[122,123]

The modulus of elasticity of the PMP was determined experimentally by using differential deflection of two cantilever beams, as shown in Figure 4.4. A cantilever beam of the PMP polymer was mounted on a rigid support and was deflected using a second cantilever of polyimide with known modulus of elasticity mounted on a moving stage. The two polymers were not rigidly connected, so only shear forces and no moments are transferred between the two beams. The ratio of the displacement at the point of contact between the two beams to the applied displacement was measured. The deflection of the junction between the two beams is simply the deflection of a cantilever beam with an end load opposite a single fixed support, given by

$$d_{jct} = \frac{F L_t^3}{3 E_t I_t} \tag{4.1}$$

where F is the force transferred between the two beams, L_t is the length of

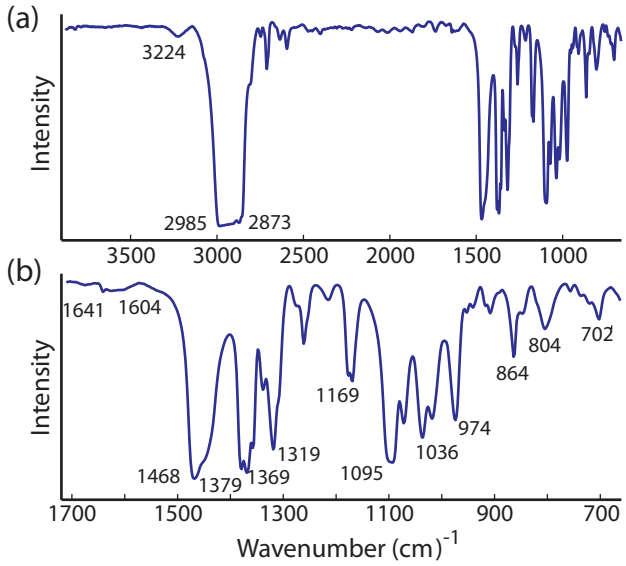

Figure 4.3: Results from the FT-IT spectroscopy on a sample of PMP, showing (a) the full spectrum and (b) a magnified view of the fingerprint region, with the location of peaks labeled.

the beam of material under test, I_t is its moment of inertia, and E_t is the Young's modulus of the material under test.[124] The reference deflection can be found in a similar way, resulting in

$$d_{ref} = d_{jct} + \frac{FL_r^3}{3E_r I_r} \tag{4.2}$$

where the subscript r refers to the reference material. Combining the two equations to eliminate the unknown force and simplifying the resulting expression gives

$$E_t = E_r \left(\frac{d_{ref}}{d_{jct}} - 1\right) \left(\frac{b_r}{b_t}\right) \left(\frac{h_r}{h_t}\right)^3 \left(\frac{L_t}{L_r}\right)^3 \tag{4.3}$$

Here, the deflections can be measured in the experimental setup, and all other properties are known. Using this methodology, the Young's modulus for both PDMS and PMP were measured, with several samples of each material being used at several different deflections. The average value for all the measurements on a given material was used as the Young's modulus value, and the standard deviation of the measurements was used as the uncertainty in the measurement. The modulus of elasticity for the PMP was determined to be 1.6 ± 0.3 GPa. For comparison, the modulus of

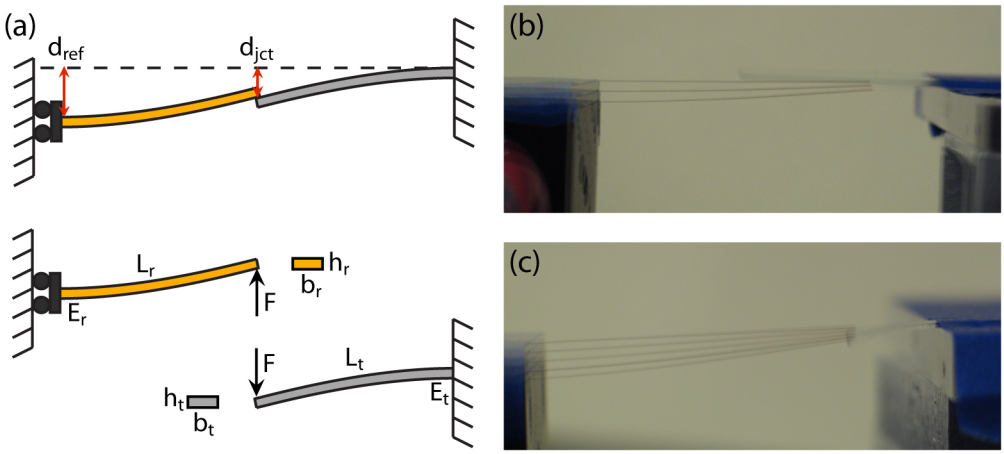

Figure 4.4: An illustration of the method for testing the Young's modulus of polymer films. (a) A schematic of the test setup, wherein one cantilever of known Young's modulus is used to deflect a cantilever of unknown Young's modulus. (b)-(c) Composite image of the beam deflections for (b) PMP and (c) PDMS.

elasticity of the PDMS was measured, using the same method, to be only 950 ± 70 kPa, a difference of three orders of magnitude.

4.4.3 Template Casting

PMP templates were created from the synthesized polymer by solvent casting. It is noted that standard polymer processing methods, such as injection molding or hot embossing, are not possible with PMP due to the lack of a glass transition temperature; the PMP breaks down before softening. Solvent casting is a viable alternative which, similar to injection molding or embossing, allows multiple templates to be created from a single master, reducing the cost per template.

In the solvent casting procedure, a silicon wafer containing the positive of the desired polymer or nanoparticle patterns is first created using standard photolithography. The pattern is then encircled by a metal casting ring, as shown in Figure 4.5. The casting ring must be completely impermeable to solvent liquids and vapors, and metal is chosen due to its high availability and machinability. This casting ring is affixed to the silicon wafer using epoxy. The PMP dissolved in cyclohexane is then poured into the casting ring. A vapor permeable PDMS membrane, which contains metal struts to manage stresses and reduce bending when the PDMS membrane swells when

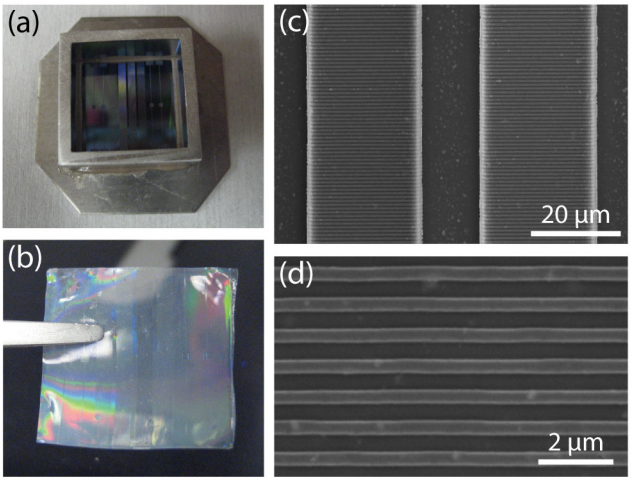

Figure 4.5: (a) A silicon template surrounded by a metal casting ring. (b) A released PMP template, exhibiting low residual stresses and moderate optical transparency. (c) An SEM micrograph of the PMP template, showing both microlines and nanolines. (d) A close-up image of the nanolines of the PMP template.

exposed to solvent vapors, is placed above the metal casting ring. The vapor permeable membrane is necessary to establish a slow, controlled evaporation rate which enables uniform drying of the polymer film and limits residual stresses in the final cast film.[125] The membrane is held in contact with the casting ring using a simple clamping mechanism created from acryllic, which holds the membrane in contact with the casting ring at the edges and allows the back of the PDMS to remain exposed to the environment. The system is placed in a fume hood and the cyclohexane allowed to evaporate completely. When dry, the PDMS membrane is removed, and the cast PMP membrane gentry removed from the casting ring by pulling with tweezers. The PMP films were then mounted on PDMS backings, using only the natural van der Waals forces for adhesion, allowing for easy handling and an even distribution of pressure across the PMP films when pressing into the substrate during patterning.

Optical and scanning electron microscope (SEM) images of the PMP template are shown in Figure 4.5. The dimensions of the template in the lateral and vertical dimensions were characterized by measuring the ratio of the pitch and height of the both micro- and nanolines on the template to those on the master. The dimensions on the template were found to match those on the master to within the margin of error for the measurement, indicating excellent pattern transfer.

4.5 Patterning Results and Analysis

The cast PMP templates were used in the patterning process described previously for patterning both nanoparticles and polymers. To begin, an initial characterization of the process was performed using cellulose acetate dissolved in acetone at room temperature. A direct comparison of the processing capabilities of the PMP template with the current standard PDMS template was made by patterning similar microscale structures on silicon substrates using each of the two different types of template. The process used for both template materials was identical, except that a higher contact pressure was used for the PMP to ensure good contact with the substrate due to its much higher Young's modulus. That is, the PDMS was held in contact with the substrate with approximately 7 kPa of pressure and PMP was held with approximately 28 kPa of pressure. The results of the patterning are shown in Figure 4.6. Feature definition is greatly improved using the PMP templates because the template is much better able to retain its shape under the pressures applied to the template during patterning, on account of the higher Young's modulus of the material. The patterning fidelity is improved insofar as the patterns created with the PMP template much better match to the designed patterns on the master. In the cross-section, while the features patterned with the PDMS template show some bowing of the walls and the top of the features, the features patterned with the PMP template have very vertical sidewalls and flat tops.

High resolution and multi-scale patterning was also demonstrated using the PMP template material. A master was fabricated which contained 25 μm wide and 2 μm tall lines at a pitch of 50 μm, between which were nanolines with 336 nm width, 840 nm pitch, and 283 nm depth. This master was created by performing standard photolithography on top of a nanopatterned silicon stamp purchased from LightSmyth Technologies. After patterning, micro and nanolines were observed to be successfully patterned over a large area. The results are shown in Figure 4.7. Both types of lines are patterned simultaneously, despite their very different lateral and vertical dimensions. The dimensions of patterned lines match those of the template to within our measurement uncertainty, indicating proper pattern transfer.

Following initial characterization of the patterning process using cellulose acetate, silver and gold nanoparticles were patterned. The silver nanoparticles were encapsulated in a hexanethiol monolayer and suspended in toluene, while the gold nanoparticles are encapsulated in a hexanethiol monolayer and suspended in alpha-terpineol. The silver nanoparticles were

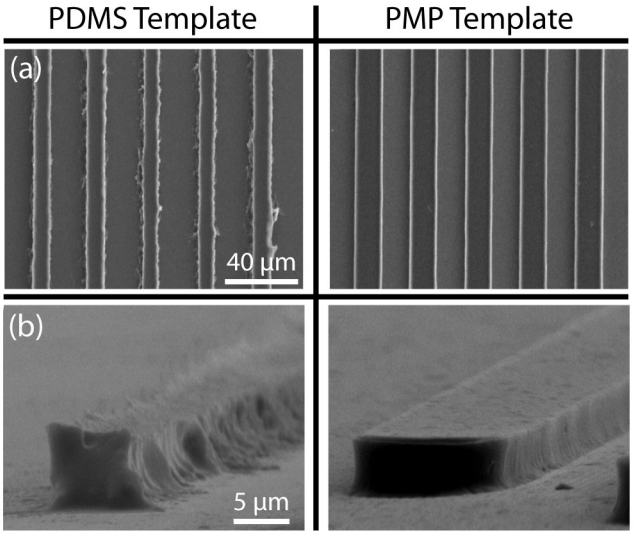

Figure 4.6: A comparison of cellulose acetate patterns on a silicon substrate created using PDMS and PMP templates. (a) A top view of patterned microlines, showing that lines created with PMP templates are much smoother and straighter, with dimensions true to those on the original template. (b) A side view of patterned microlines, showing that lines created with PMP templates have smoother, more vertical sides and flat tops.

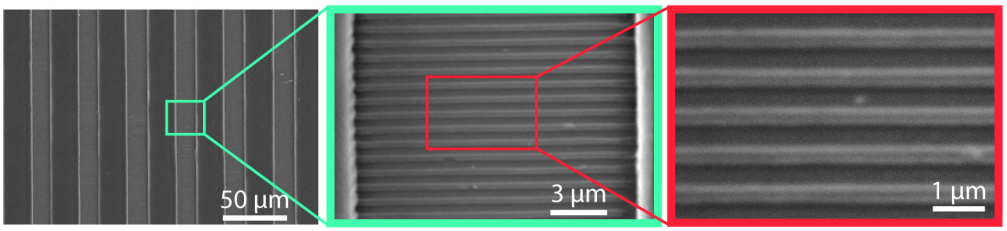

Figure 4.7: SEM micrographs of high resolution cellulose acetate lines on silicon patterned using a PMP template.

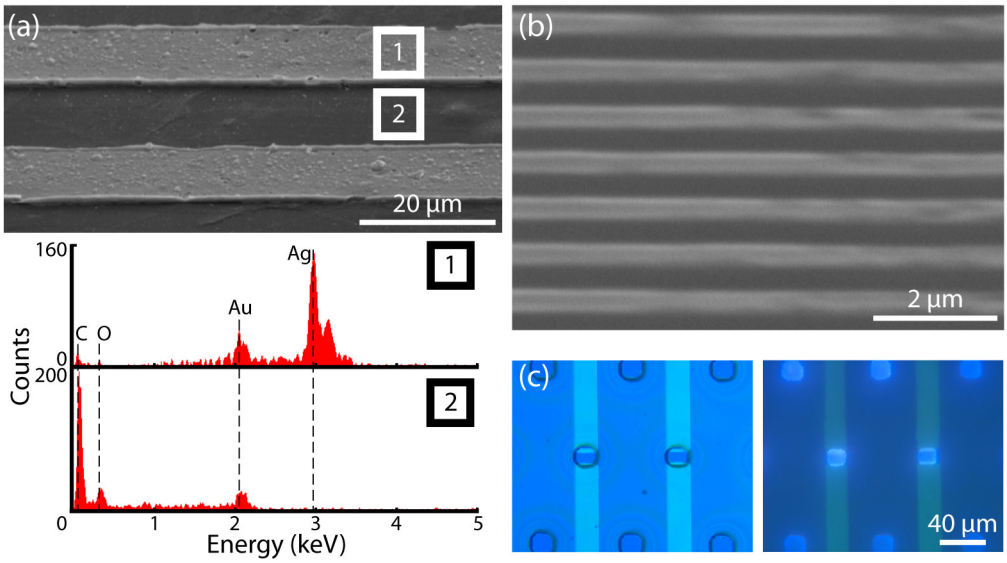

Figure 4.8: (a) An SEM micrograph (top) and EDX data (bottom) for silver nanoparticles patterned on a polyimide substrate. The boxed numbers on the SEM image indicate the positions where the EDX data was acquired. (b) An SEM micrograph of gold nanoparticles patterned into nanoline configurations on silicon. (c) (left) A cellulose acetate sheet on silicon, patterned with alignment to existing gold electrodes. (right) Zinc oxide nanoparticle patterns created using a lift-off method described previously in Chapter 2.

patterned into microlines on a polyimide substrate at room temperature. A thin layer of gold was sputtered on the resulting patterns to allow for SEM imaging of the lines on the polymer substrate, and energy-dispersive x-ray spectroscopy (EDX) was used to characterize the patterning. The results are shown in Figure 4.8. Strong peaks of silver and gold are seen in the patterned areas, resulting from the nanoparticles and the thin layer of gold used for imaging, with small peaks of carbon and oxygen resulting from the hexanethiol monolayer and polyimide substrate. Only carbon, oxygen, and gold are detected between the patterned lines, and no trace of silver is observed. This analysis indicates that no residual layer is formed between patterned lines in the PMP template, which in turn proves that a good seal formed between the PMP and the substrate despite the increase in Young's modulus of the polymer as compared to PDMS templates.

Gold nanoparticles were patterned on a silicon substrate into nanolines having a width of 314 nm and a pitch of 810 nm, as shown in Figure 4.8. The patterning was done at a temperature of 70°C to facilitate evaporation

of the solvent. The results were similar to those of the cellulose acetate patterns created previously. However, the heights of the gold nanoparticle features show some slight variation along the length of lines, which could be due to oxidation of the hexanethiol monoloayer on the particles and some reflow resulting from the corresponding reduction in volume. The ratio of the height of the gold nanolines to the measured height of the template used in patterning was 0.85 ± 0.05, indicating that some volume shrinkage did indeed occur. Since this volume reduction occurs while the template is still in place, the side walls remain straight and only the vertical dimension is reduced. The non-uniformity of the height is suspected to be the result of a Plateau-Rayleigh instability that forms as the vertical dimension is reduced. The distance between peaks of this waviness were measured, and it was found that the wavelength was 1.4 ± 0.5 μm. This is similar to the calculated wavelength at which instabilities would grow fastest, which is calculated to be 1.38 μm for lines of these dimensions.[126]

Finally, the ability to create multi-level patterning was demonstrated by patterning zinc oxide (ZnO) nanoparticles on top of previously defined gold electrodes, using a mechanical lift-off process described previously in Chapter 2. ZnO nanoparticle patterns were made by first patterning a perforated cellulose acetate sheet using the method described above, depositing ZnO nanoparticles into the patterned perforations using the natural evaporation of a sessile droplet, and removing the weakly-adhered cellulose acetate sheet mechanically using crepe paper masking tape, leaving the nanoparticle patterns behind. The alignment between the PMP template and the gold electrodes was done using a press consisting of precision vertical and horizontal alignment stages together with an optical microscope with a long working distance. The alignment was done through the optically transparent PMP template, which was mounted on PDMS and adhered to glass by van der Waals forces. Unlike the process described previously, the more rigid PMP template was used as the template material, rather than the rubbery PDMS, allowing the template to be aligned to the substrate much more easily and eliminating the Poisson expansion of the template with applied pressure. The patterned cellulose acetate sheet and the final ZnO nanoparticle patterns are shown in Figure 4.8, showing that good alignment was achieved.

4.6 Future Directions

The above work proves that vapor permeability and rigidity can be decoupled, ensuring that a robust template which will not bend or distort under pressure can be created for use in permeation-based patterning. However, other substituted polyacetylenes beyond just PMP should be examined for use as a template for patterning. Indan-based polyacetylenes have higher vapor permeabilities and, depending on the specific chemical arrangement, can have greater solvent compatibility than the PMP. The surface chemistry of these polymers may or may not be better in terms of solvent wettability and release properties, and should be investigated further.

Additionally, the masters used for creating the PMP templates, while operable, are not ideal. The adhesion between the template and the master is strong, and can lead to damage of the template or the master after creation of several templates. Masters with lower adhesion may therefore lead to longer lifetimes and therefore more templates created per master, reducing the cost per template and thus the cost per pattern. Therefore, methods of creating masters from different materials with weaker adhesion to the cast template material should be investigated.

Similarly, the process for creating the masters by solvent casting are currently very slow. Such a slow evaporation is required to prevent high residual stresses in the templates. However, the long processing time causes a higher cost per template. Optimization of the solvent casting procedure can therefore lead to higher throughput template creation while maintaining high quality feature reproductions.

Chapter 5

A Continuous, Roll-to-Roll Patterning Process

Systems capable of creating sensors and electronics in a continuous, roll-to-roll manner have received much attention recently. As demonstrated in the graphic arts, these systems are capable of creating products rapidly, in large volumes, over large areas, and in a scalable manner. These factors all lead to a reduction in the ultimate cost of the product.

In the process described in previous chapters, high resolution and high fidelity patterns are created in a stamp-and-repeat process. This process is particularly beneficial because it is completely additive, with no etching steps required after patterning, and can be done in standard atmospheric conditions. As a result, the process is amenable to conversion to a roll-to-roll process. Such a conversion could result in several additional benefits for the system. First, throughput is increased as the substrate handling is integrated with the patterning, increasing the utilization of the patterning step. The integration of the material handling and patterning also simplifies the substrate handling, reducing the system cost. Continuous patterns can be created from a carefully constructed belt containing no seams, enhancing the area of the substrate utilized for patterning and reducing waste. Long patterning runs are possible, as the system is easily automated and requires a low amount of operator input.

This chapter will discuss the development of a continuous, roll-to-roll process. The proposed system will be described, and important design considerations for such a system will be discussed. A prototype system will

be shown along with patterning results from such a system, demonstrating the proof-of-concept for the proposed roll-to-roll system.

5.1 Process Description

The concept for a roll-to-roll process using the patterning method described in previous chapters is shown in Figure 5.1. Here, the patterns are created on the substrate using a patterned vapor-permeable polymer. However, instead of a stamp, a continuous belt is used. A flexible substrate onto which the patterns are to be made is rolled over a substrate roller, where it is brought into contact with the patterned belt. The belt features are filled with solvent by maintining a solvent meniscus at the point of contact between the belt and the substrate. As the belt makes contact, excess solvent is excluded from underneath the belt, with any residual solvent layer evaporating through the vapor permeable polymer belt and leaving no residual layer behind. The nanoparticle or polymer ink is then introduced to ink reservoirs in the template, which may either be on the side or through the back of the belt. The solvent is then evaporated through the vapor permeable belt, causing a negative pressure that forces the ink to flow into the belt features. Further evaporation of solvent causes the solute to become concentrated inside the belt features. When the solute fills the features completely and the solvent is completely evaporated, the belt is rolled off of the substrate, leaving the patterned solute on the substrate. The belt is then cleaned to ensure that any residual solute is removed from the surface of the belt, dried to remove solvent vapors from the interior of the belt, and returned to the substrate for additional patterning.

This design was chosen due to the high level of adaptability. Belts are easily created with many different types of patterns and designs, as they can be cast directly from masters on rigid substrates created using traditional photolithography. Therefore, the system is easily changed to new configurations during the prototyping phase. This is in contrast to other system designs, such as patterned rollers, are substantially more difficult to create. It is noted that other system designs may be better for an actual manufacturing setting, where such high levels of adaptability are not necessary.

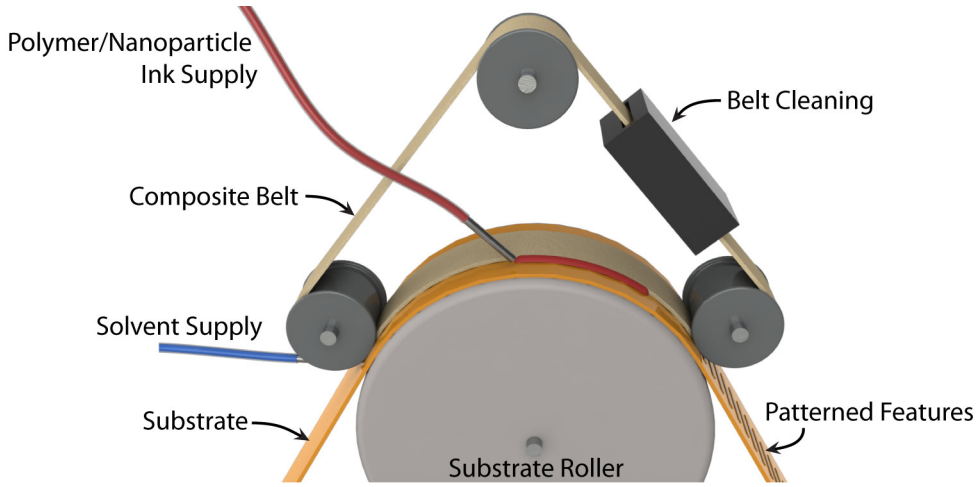

Figure 5.1: A schematic of the roll-to-roll patterning concept. A belt is rolled into contact with a substrate in the presence of solvent, filling the belt features. A nanoparticle or polymer ink is introduced to open ends of features, and evaporation of solvent through the vapor-permeable belt causes the features to fill with solute. When dry, the belt is rolled off from the substrate, where it is cleaned, dried, and returned for continued patterning.

5.2 Design of Belts for Roll-to-Roll Patterning

The requirements of the belts used in the roll-to-roll patterning process are similar to the requirements for the templates in the stamp-and-repeat process discussed in Chapter 4. This includes high vapor permeability, high chemical and thermal stability, optical transparency, low surface energy, and high rigidity. However, in addition to these requirements, the belts must also be sufficiently mechanically robust in order to handle the tension required to supply the contact pressure between the belt and the substrate and the repeated bending as the belt travels over rollers a large number of times.

Considering the set of vapor permeable polymers examined in Chapter 4, none of these materials satisfy all of the requirements for a roll-to-roll belt. That is, these materials are typically not mechanically robust enough to handle the necessary tension and bending conditions seen in such a belt. However, by combining these materials with fibers of a more mechanically robust material, all requirements can be satisfied. The fibers carry the tension required in the belt without interfering with the patterning or vapor permeability, and the vapor permeable polymer rides on the fibers, providing

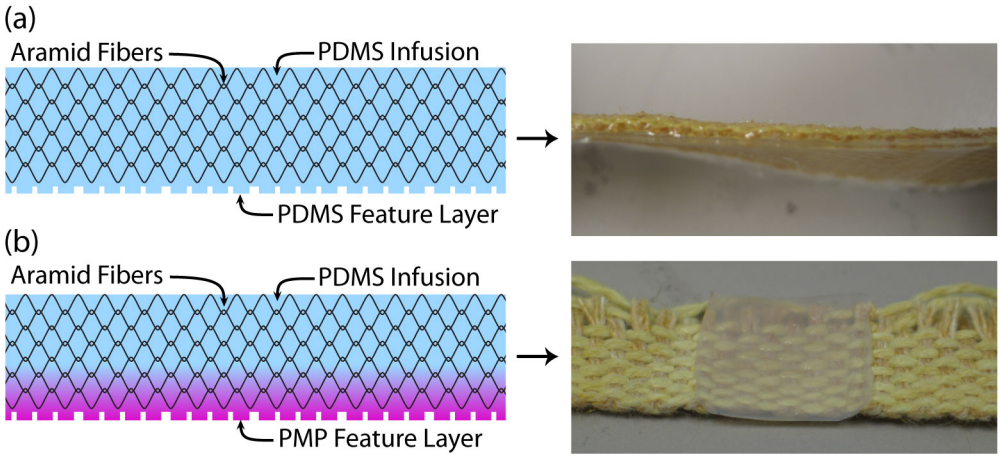

Figure 5.2: Schematic diagrams and photographs of (a) the PDMS-aramid fiber composite belt, and (b) the PMP-PDMS-aramid fiber composite belt.

the patterning capability.

Two types of vapor permeable belts were made, using both the PDMS and the PMP polymers described in Chapter 4. These belts are shown in Figure 5.2. The master for the PDMS template was made using standard photolithography. The master was then coated with a 10:1 mixture of PDMS prepolymer and crosslinker, which was reduced to an approximately 200 μm thin layer by blowing with compressed air followed by a 1h rest to ensure a uniform polymer film. The polymer was then partially crosslinked by heating on a hotplate at 60 °C for approximately 10 min, or until the polymer was highly viscous but not yet solid. A woven aramid fiber was coated with a thin layer of PDMS, which quickly soaked into the aramid fibers by capillary action. This PDMS-aramid composite was then pressed into the partially-cured PDMS on the master, and allowed to cure fully on the hotplate at a temperature of 75 °C for approximately 2 h. When cured, the PDMS was removed from the silicon wafer master and excess PDMS was cut from the edges of the aramid fiber.

The PMP belt was made in a slightly different manner. The PMP feature layer was created by casting on a silicon wafer master using a metal casting ring and PDMS gasket, as described in Chapter 4. When fully dry, the PMP feature layer was removed from the master by pulling gently with tweezers. Excess PMP was cut from the edges of the template with scissors. Both the back of the PMP feature layer and a woven aramid fiber was then painted with PMP dissolved in cyclohexane, and the feature layer was affixed to the aramid fibers by pressing briefly, followed by allowing the solvent to

dry at room temperature for 1 h with no externally applied pressure. The back of the fiber network was then painted with a 10:1 mixture of PDMS prepolymer and crosslinker, which allows for better stress handling in the belt and a longer belt lifetime. The PDMS was cured on a hotplate at 75 °C for around 2 h.

5.3 Prototype Design

A schematic of the prototype system is shown in Figure 5.3, and the actual system is shown in Figure 5.4. The full system is approximated by a discrete section of belt. The substrate is attached to the substrate roller with tape, simulating the intimate contact between the two and ensuring no slippage even though the full substrate handling system is lacking. The substrate roller is affixed to a stationary frame through a bearing. The actuation of the substrate roller is done by pulling on a wire tether wrapped around the substrate roller. The belt is attached to the substrate roller by a pin through the center of the belt. The pin joint forces the belt to make contact with the substrate roller at that location and provides an anchor for the applied tension to the belt. However, this pin joint can not carry any moments, simulating the condition that would exist in the belt at that location. It is noted that while stresses are concentrated at the center of the belt around the pin joint, these stresses will distribute across the width of the belt far from the pin joint. The patterned area of the belt is therefore separated from the pin joint by a distance sufficient to adequately distribute these stresses. The opposite end of the belt is sewn into a loop, into which a steel dowel rod is placed. Weights are applied to the steel dowel rod, which are used to apply the desired tension to the belt. Again, the location of the weights are separated from the patterned area of the belt sufficiently to distribute any uneven stresses.

The patterning process is simulated by rolling the belt onto the substrate in the presence of clean solvent, patterning the solute from an appropriate ink while the system is stationary, and then removing the belt by rolling it off of the substrate. The filling is performed by turning the substrate roller by pulling on the tether while at the same time using a syringe to supply clean solvent to the point of contact between the belt and the substrate. When the area of interest is filled, the rotation of the substrate roller is stopped and a syringe is used to apply ink to fluid reservoirs in the belt. Evaporation of solvent draws the ink into the belt features and concentrates

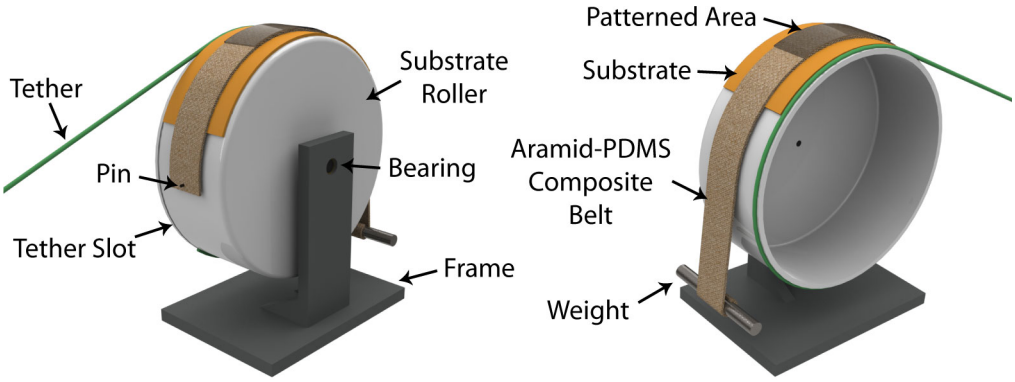

Figure 5.3: A schematic of the prototype roll-to-roll patterning assembly. The substrate is attached to the substrate roller, and the belt pinned to the same. The belt is tensioned using a weight, and the rotation of the substrate roller controlled by moving an anchor (not shown) attached to a tether wound around the roller.

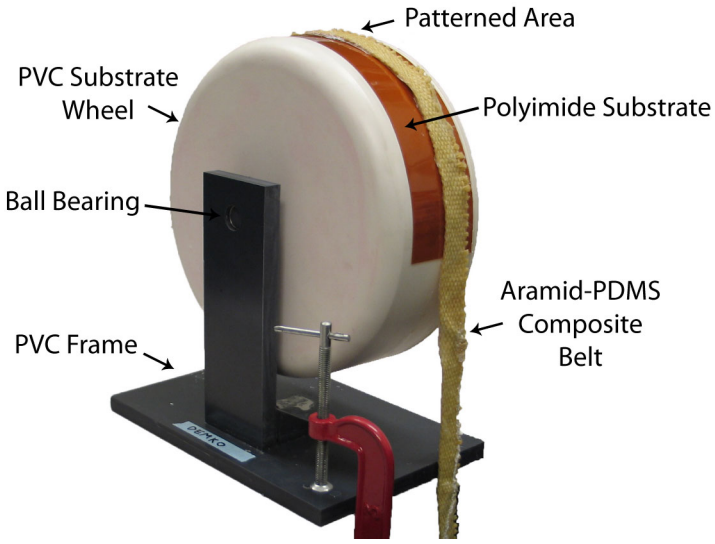

Figure 5.4: A photograph of the actual prototype roll-to-roll patterning assembly.

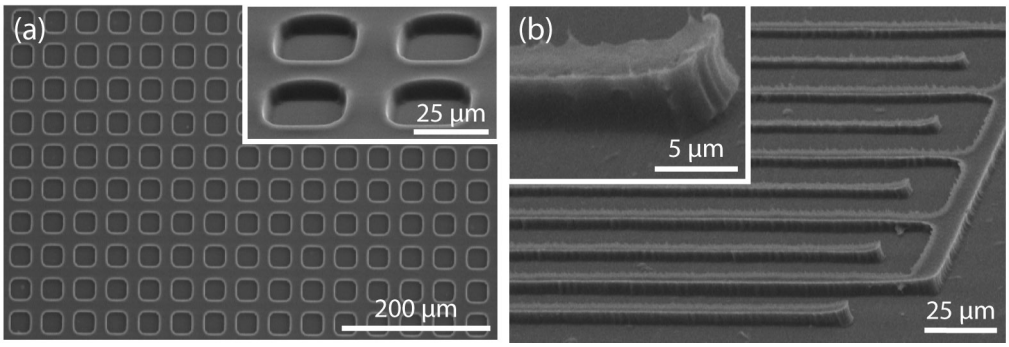

Figure 5.5: SEM micrographs of cellulose acetate on polyimide created using a PDMS-aramid fiber composite belt.

the solvent. When the system is completely dry, the belt is removed by turning the substrate roller in the opposite direction by allowing the tether to wind around the substrate wheel. The belt detaches from the substrate and the patterned substrate is removed from the roller.

5.4 Patterning Results

The results of patterning with the prototype system are shown for the PDMS belt in Figure 5.5 and for the PMP belt in Figure 5.6. The PDMS belt is used to create features with quality similar to that of the stamp-and-repeat process. Some distortion of features is seen due to the low Young's modulus of the material coupled with the pressure applied between the belt and the substrate as well as the tendency of this material to swell when exposed to solvents. Any additional distortion caused by the tension applied to the belt is minimal, due to the tension forces being carried mostly by the more rigid aramid fibers rather than the flexible PDMS.

The belt containing PMP is also used to successfully create features having improved quality as compared to those created using the PDMS belt. This improvement in quality is due to the higher Young's modulus of the PMP. However, results over large areas are still in need of improvement, due to several challenges that remain in creating and using the PMP-aramid fiber composite belts. The current method of attaching the PMP to the aramid fibers can cause the PMP layer to warp and distort locally. This distortion, together with the high Young's modulus of the material, prevents the belt from contacting the substrate in all areas. This causes patterns to be transferred only in limited areas while also increasing the

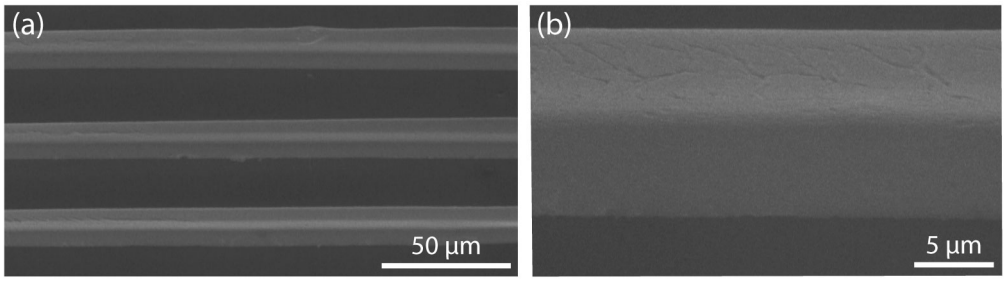

Figure 5.6: SEM micrographs of cellulose acetate on polyimide created using a PMP-PDMS-aramid fiber composite belt, each taken with a 45° tilt to show the height of lines.

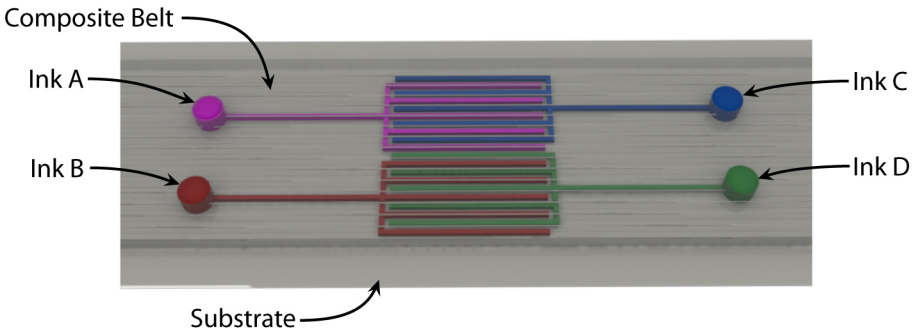

Figure 5.7: A schematic image of a next generation belt. The vapor permeable polymer is integrated with fibers along the axial direction. Template features are connected to ink reservoirs in the back of the belt, each of which can be filled with a different ink.

likelihood of air becoming trapped under the template, interfering with the evaporation-driven fluid flow and ending template filling prematurely. However, some patterns are able to be created over small areas, indicating that such patterning is indeed possible if such problems with the belt can be addressed.

5.5 Future Directions

The prototype system developed here is far from a complete roll-to-roll system as would be used in a manufacturing setting. Further development of such a system would require design of the complete system including a closed belt path, variable tensioning across the width of the belt, a belt cleaning and drying system, and an ink and solvent delivery system. The belts themselves also require substantial development to enable continuous

patterns along the length of the belt and to increase the mechanical robustness. An example of such an improved belt system is shown in Figure 5.7. First, a better system for integrating proper amounts of aramid fibers, in the proper configurations, into the PDMS or PMP belts must be developed. Next, a better system for loading ink into the belts should be developed, which can be done by loading ink into dedicated reservoirs in the back of the belts. Such changes to the belts would, of course, require corresponding changes in the overall system, including the ink handling and belt cleaning processes.

Chapter 6

Applications

As a practical demonstration of the developed patterning process for manufacturing, two applications were developed. First, low temperature metallization was achieved using gold nanoparticles. These nanoparticles were pattered using the methods described previously, and then sintered at low temperatures to form conductive traces. Next, an ultraviolet light sensor was created from zinc oxide nanoparticles patterned between two electrodes. The high surface area of the nanoparticles enables the high sensitivity of the resulting sensor. This chapter discusses the development of each of these two applications, including results and analysis from each of the manufactured devices.

6.1 Low-Temperature Metallization using Gold Nanoparticles

6.1.1 Introduction

As discussed in Chapter 1, the high surface to volume ratio of nanoparticles can lead to changes in their physical properties, including the melting temperature of the material. This melting point depression is due to the large proportion of the total number of atoms in the crystal that exist at the surface. These surface atoms contain many unsatisfied bonds, causing these atoms to exist in a higher energy state then atoms in the interior of the crystal. For a material in which a large proportion of the atoms exist in this higher energy state, less energy is needed to transition the material

from a solid to a liquid phase. Therefore, if nanoparticles with a sufficiently small size are packed closely together, these particles can be sintered together with the addition of heat. That is, the additional energy enables the atoms in the material to become more mobile and form bonds with adjacent nanoparticles to reduce their surface area and thus achieve a lower energy state.

This melting point depression can be determined theoretically by applying the principle of conservation of energy to the phase transition of a nanoparticle. This is done, to a first order approximation, in Appendix E. The result is known as the Gibbs-Thomson equation, and is given as

$$T_m = T_{m,\infty}\left[1 - \frac{2(\gamma_s - \gamma_l)}{\rho r_p \Delta H_{m,\infty}}\right] \tag{6.1}$$

where T_m is the melting temperature of the nanoparticle, $T_{m,\infty}$ is the bulk melting temperature, γ_s and γ_l are the surface energies of the solid and liquid phases, respectively, ρ is the density of the material, $\Delta H_{m,\infty}$ is the enthalpy of the bulk phase transition, and r_p is the radius of the spherical particle. The melting temperature is plotted as a function of particle diameter in Figure 6.1. As a result, the calculated melting temperature of the particles is significantly less then the bulk melting temperature for particles with a diameter of less than 4 nm.[127,128] Such thermodynamic models have been determined to be experimentally accurate, at least to a first order approximation.[127]

The model of melting and sintering of gold nanoparticles is complicated by the presence of other chemistry at the surface of the particles. Thiol monolayers are often present on the surface of the gold particles either as a byproduct of nanoparticle synthesis or intentionally for ease of dispersion in organic solvents.[129] These thiol monolayers must be removed prior to sintering the particles, as shown in Figure 6.1. This is done by oxidizing the thiol, causing adjacent molecules to combine and form a disulfide. This disulfide byproduct must then be removed from the system, allowing the bare nanoparticles to sinter together.[130] Many different thiols have been investigated for use in coating gold nanoparticles. While short-chain thiols are easily oxidized and the disulfide byproducts removed more easily, the long-term stability of the nanoparticles in organic solvent is poor. Longer-chain thiols improve stability, but at the expense of more difficult oxidation of the thiols as well as removal of the reaction byproducts.[49,131]

Gold nanoparticles have previously been used for low-temperature metallization with inkjet printing, electrohydrodynamic jet printing, nanoim-

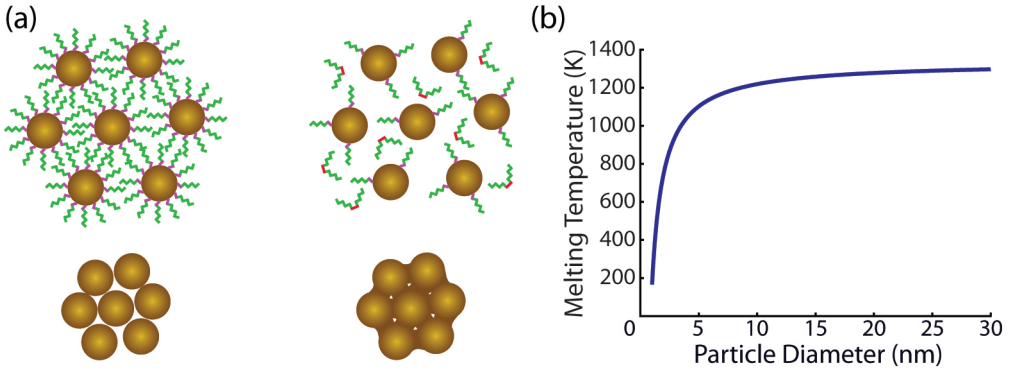

Figure 6.1: (a) The particle sintering process. The gold nanoparticles are initially coated in a hexanethiol monolayer, consisting of a carbon chain (green) and a gold to sulfur bond (purple). When heated, the gold to sulfur bond breaks and adjacent thiols form a disulfide bond (red) and diffuse away from the nanoparticles. The gold particles are then free to join together. (b) The melting temperature of a gold nanoparticle as a function of the particle diameter, as calculated from Equation 6.1.

print lithography, and gravure printing.[7,49,132–134] However, these previous patterning technologies all suffer from either low resolution, low patterning fidelity, low throughput, or a residual layer which must be etched away after patterning. Patterning gold nanoparticles with the current method allows all of these problems to be overcome.

6.1.2 Experimental Methods

Gold nanoparticles encapsulated in a hexanethiol monolayer were synthesized using a two-phase reduction method following the method of Brust et al.[129] The resulting nanoparticles were approximately 2-4 nm in diameter. The ink was diluted to 3.5 wt% using alpha-terpineol as the solvent.

The nanoparticles were patterend using the process described in Chapter 2. Briefly, a polyimide, glass, or silicon substrate was coated with clean alpha-terpineol and positioned below the patterned PDMS elastomer template. The fresh solvent was patterned by pressing with the PDMS template. The pressure used was just enough to completely conform the elastomer mold to the substrate, and did not exceed 14 kPa. The nanoparticle ink was then added to designated filling ports at the ends of the channels. The temperature of the system was raised to 75°C to evaporate the solvent through the PDMS template. When the ink was completely dried in the microchannel, the system was cooled and the polymer template removed.

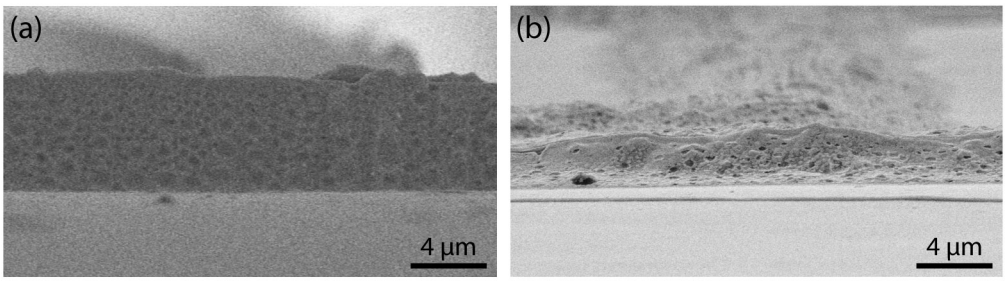

Figure 6.2: SEM micrographs of the gold nanoparticle lines (a) before and (b) after sintering.

Following patterning, the particles are then sintered by heating on a hot plate at 220 °C in atmospheric conditions for 8 h, which allows oxidation of the thiols. The electrical resistance of the particles was measured using an electrical probe station with a digital multimeter.

6.1.3 Results and Analysis

The nanoparticle lines before and after sintering are shown in Figure 6.2. The dimensions of the patterned lines before sintering are approximately 11 μm in the horizontal dimension and 6 μm in the vertical dimension. The particles still contain thiol monolayers at this point and, as such, are not electrically conductive. After sintering, the average height of the sintered gold particles was approximately 2.5 μm. The feature heights exhibited a small amount of waviness over short distances, but the average height of the traces was constant over the entire area. The profile of the sintered gold traces was significantly different from that of the unsintered particles. The reflow of the gold during sintering changed the shape from an approximately rectangular cross-section to a dome shape. After the reflow, the average line width had expanded to around 16 μm.

Electrical characterization of the gold likes was performed by measuring the electrical resistance as a function of distance, as seen in Figure 6.3. The resulting measurements show that resistance is linearly proportional to the distance, even over large areas, indicating that both the conductivity and the cross-sectional area of the sintered gold are constant over the entire printed area. The cross-sectional area of the gold wires was approximated by using a circular segment with the same average height, width, and contact angle as measured from the experiment. Using the measured resistance per unit length and the calculated cross-sectional area of the gold traces, the

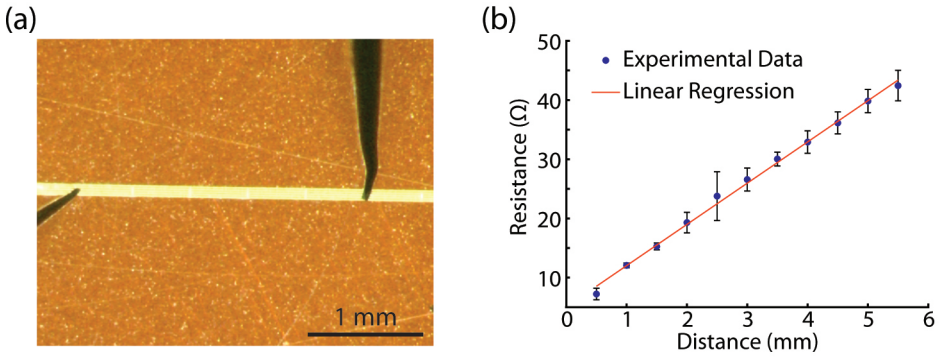

Figure 6.3: (a) Sintered gold lines on polyimide, with electrical probes for measuring resistance. (b) Resistance as a function of distance for the gold on polyimide.

average resistivity of the lines was measured to be $6.7x10^{-7}$ Ωm. The lines are therefore approximately 4% of the conductivity of bulk gold. This value is slightly lower than other values reported in the literature for thermally-annealed gold nanoparticles, which may be caused by the larger height of the printed features and the corresponding difficulty for the oxidation of the hexanethiol monolayer and the migration of the disulfide byproduct out from the sintered gold.[7,49,91,131,135,136]

6.2 An Ultraviolet Light Sensor using Zinc Oxide Nanoparticles

6.2.1 Introduction

Zinc oxide is a wide bandgap semiconductor that absorbs light with energy greater than or equal to its 3.3 eV bandgap. This makes the material photosensitive to ultraviolet (UV) light. However, unlike other wide bandgap semiconductors, the charge carriers created by such photoelectric generation cause a substantial change in the surface chemistry of the semiconductor in addition to increasing the mobile charge density. The surface of zinc oxide normally contains adsorbed oxygen molecules, caused by capture of a free electron from the semiconductor. The presence of these adsorbed oxygen molecules causes a depletion layer to exist at the surface, lowering the conduction area of the material. When holes are generated near the surface of the semiconductor, they cause the oxygen to desorb from the surface. The oxygen is then free to diffuse away from the surface, decreasing the width

of the depletion region and increasing the conduction area. The combination of the change in surface states with the generation of additional mobile charge carriers causes the very high sensitivity of zinc oxide to UV light when the material is configured such that it has a high surface area.[10]

Since much of the change of conductivity is caused by changes at the surface of the material, it follows that using configurations of zinc oxide with more surface area can lead to increases in sensitivity. Thin films consisting of bulk materials with large numbers of grain boundaries, nanowires, and nanoparticles have all been successfully used to increase the surface area and sensitivity of the corresponding UV sensors.[10,137,138] Of these, nanoparticles offer the highest surface to volume ratio, and can be synthesized in batch processes separately from the fabrication of the sensor and then patterned using solution processing.[10] However, most zinc oxide nanoparticle UV sensors are created either without any patterning, such as by spin-coating over large areas, or using simple and low-resolution patterning methods, such as screen printing.[10,139,140] Some higher resolution patterning of zinc oxide has been done by inkjet printing or micromolding in capillaries, but the current methods are not able to produce isolated features at sufficiently high resolution and throughput.[51,96] By patterning these nanoparticles with the current method, higher quality patterns can be formed. This enables the creation of sensors with a smaller form factor which can be better integrated into sensing platforms having multiple sensing elements or other electronics in close proximity.

6.2.2 Experimental Methods

A UV light sensor was created by patterning a 400 μm^2 square of zinc oxide nanoparticles between two gold electrodes on a silicon dioxide substrate. A schematic and optical micrograph of the fabricated sensor are shown in Figure 6.4.

The basic process for patterning the zinc oxide nanoparticles was described in Chapter 2. However, some additional steps are required to create the gold electrodes on the substrate and to align the nanoparticle patterns to gold electrodes. The gold electrodes were created by conventional photolithography. 100 nm of thermal oxide was grown on a lightly doped p-type silicon wafer and photoresist was spin-coated. After photolithography, 5 nm of chrome and 25 nm of gold were deposited by thermal evaporation, followed by lift-off. Following electrode deposition, a cellulose acetate template was patterned on the electrodes. The substrate containing the electrodes

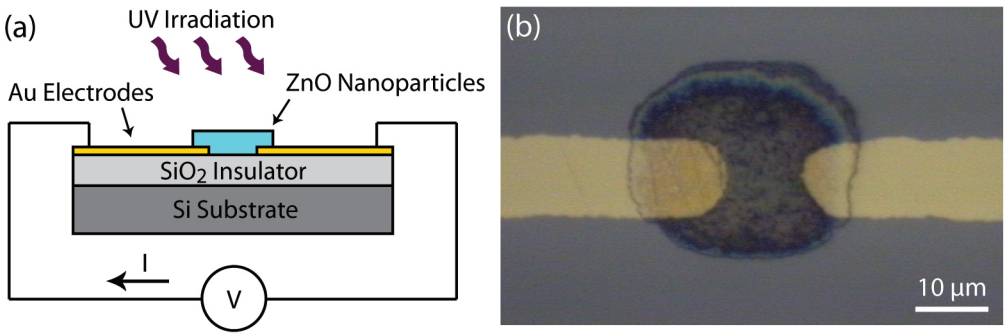

Figure 6.4: (a) A schematic of the ultraviolet light sensor. (b) An optical micrograph of the sensor, showing zinc oxide nanoparticles patterned between two gold electrodes.

was coated with clean solvent (acetone) and a PDMS mold was aligned to the electrodes using a CCD microscope with a long working distance and a press consisting of precision horizontal alignment stages. Cellulose acetate dissolved in acetone to a 1% concentration was introduced to the edge of the PDMS mold, and solvent was evaporated through the PDMS mold at room temperature to pattern the polymer. Once the cellulose acetate pattern was made, the PDMS template was removed and a droplet of zinc oxide nanoparticles in water at a 1 wt% concentration was placed on the template. The solvent was allowed to dry at room temperature, causing the nanoparticles to deposit into holes in the polymer template. When dry, the template was removed using crepe paper masking tape.

The resulting sensor was characterized using a UV lamp (UVP, UVGL-25) capable of creating UV light at 365 nm and 254 nm with an intensity of 720 and 760 μW/cm^2, respectively, at a distance of 7.6 cm from the light source. A Keithly 2400 Sourcemeter was used to supply a constant voltage and measure the current through sensor. A constant bias of 20 V was applied to the sensor to ensure a very clear signal to noise ratio of both the short and long wavelength light so the selectivity of the sensor could be adequately characterized.

The selectivity of the sensor to the two wavelengths of light was measured by affixing the light source at a distance above the sample to irradiate the sensor with an intensity of 71 mW/cm^2. The light was repeatedly turned on and off, using both wavelengths of light, and the current through the sensor monitored. Assuming that the transient response is caused either by carrier generation and recombination events[25] or a first-order oxidation or reduction reaction,[141] the rise can be modeled as an exponential given by

$$I = I_0 \left[1 + \exp\left(\frac{-t}{\tau}\right)\right] \tag{6.2}$$

and the fall by

$$I = I_0 \exp\left(\frac{-t}{\tau}\right) \tag{6.3}$$

where I is the current as a function of time, I_0 is the maximum current, and τ is the time constant for the rise or decay.

The sensitivity to various intensities of light at 254 nm wavelength was characterized by varying the distance from the lamp to the sensor. The current through the sensor was measured as a function of this distance. The variation in the intensity of light reaching the sensor is expected to vary as the view factor from the cylindrical light source to the point sensor. Therefore, a curve was fit to the data of the sensor current to the distance of the sensor to the lamp according the equation

$$I = a_1 * \left(\frac{1}{x - a_2}\right)^{a_3} \tag{6.4}$$

where I is the current, x is the distance from the light to the sensor, and the fitting parameters a_1 , a_2 and a_3 fit the sensitivity of the sensor, lensing effects from the wavelength filter in front of the lamp, and the non-linearity of the sensor, respectively.[142]

6.2.3 Results and Analysis

The patterns were successfully created on the gold electrodes, as seen in Figure 6.4. However, due to the low Young's modulus of the PDMS mold and corresponding large Poisson effect, the cellulose acetate patterns do not align to the gold electrodes over large distances. That is, the zinc oxide patterns in the vicinity of the alignment marks are well aligned to the gold electrodes, which become increasingly misaligned to the electrodes with increasing distance from the alignment marks. This problem can be solved by using more rigid PMP molds in patterning, as was done in Chapter 4.

The selectivity of the sensor to various wavelengths of UV light was then characterized. The resulting current through the sensor as a function of time for different wavelengths is shown in Figure 6.5. The 365 nm light created a 25 μA response with a rising time constant of 0.9 s and a falling time constant of 5.8 s. The 254 nm light created a 12.9 mA response with a rising time constant of 93 s and a falling time constant of 244 s. The

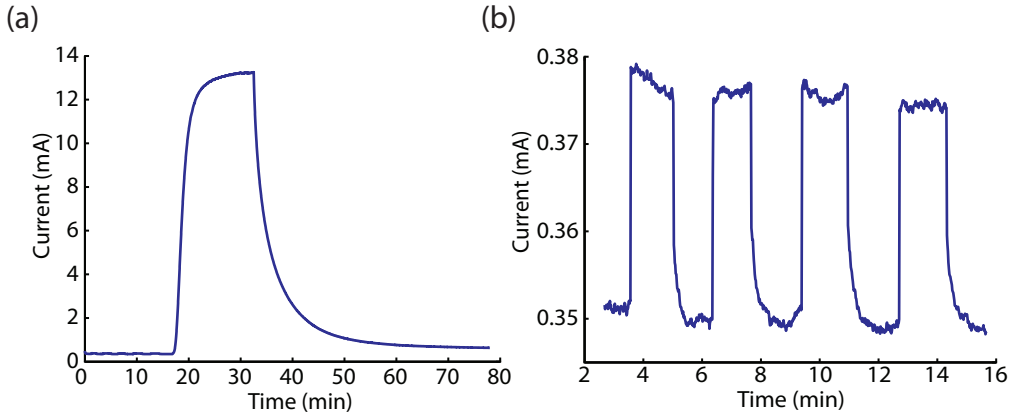

Figure 6.5: (a) The current response of the sensor under a constant bias of 20V when flashing 365 nm light (0-16 mins) and 254 nm light (after 18 mins) at an intensity of 71 mW/cm^2. (b) A close-up of the response to 365 nm light from part (a).

fast and low-amplitude response to UV light at 365 nm is consistent with lowering of the energy barrier at the Schottky contact caused by promotion of electrons to interface traps by sub-bandgap energy light. Light at 254 nm caused a much slower and larger amplitude response, consistent with creation of electrons in the conduction band and holes in the valence band and the corresponding reduction of adsorbed oxygen on the surface of the semiconductor, causing the depletion region at the edges of particles to shrink and the bulk resistance of the nanoparticle network to drop.[140,141,143,144] The strength of the signal for the 254 nm wavelength light was more than 500 times greater than that of the 365 nm wavelength light at a similar intensity, showing excellent wavelength selectivity.

The sensitivity of the sensor was measured by varying the distance from the light source to the sensor. The current through the sensor as a function of distance from the light source as well as the current through the sensor as a function of incident light intensity are shown in Figure 6.6. The data was fit to the theoretical current as a function of distance as given in Equation 6.4 using a least-squares regression. The data and theory curves achieved a coefficient of determination of 0.9999, indicating an excellent fit. The curve fit showed that, for this sensor

$$I \propto \omega^{0.65} \tag{6.5}$$

where ω is the light intensity at the sensor. This power-law relationship

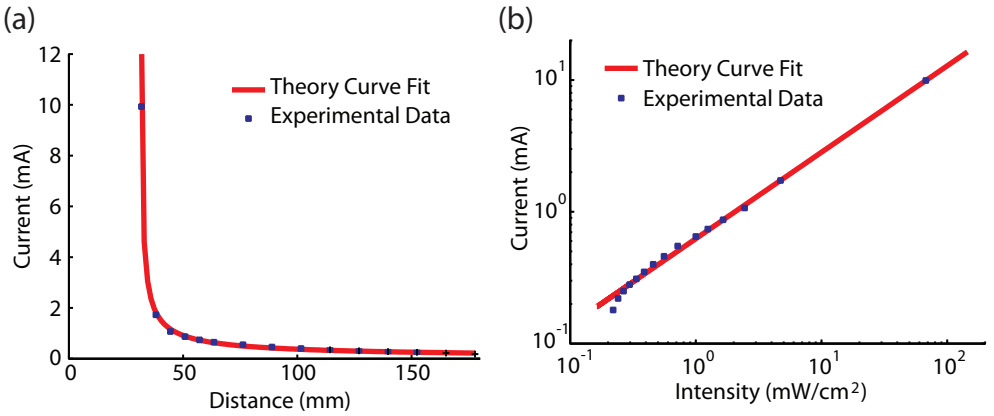

Figure 6.6: The experimental data and theory curve-fit for sensor current as a function of (a) physical distance of the sensor from the light source, and (b) intensity of light reaching the sensor.

and the calculated non-linearity is consistent with similar zinc oxide UV sensors,[145] and is due to the dynamics of generation, trapping, and recombination of electrons and holes in the semiconductor material.[146] The sensitivity of the sensor at any given intensity is calculated as the slope of this curve at the given location. An absolute sensitivity (defined as current per unit of incident radiation intensity) of 0.388 A cm^2/W was obtained at an intensity of 71 mW/cm^2, a value less than other similar sensors seen in the literature, especially considering the higher voltages used in the detection here. However, considering a relative sensitivity independent of geometry (defined as current per unit of radiation energy), a sensitivity of 9.707×10^4 A/W was obtained, a value higher substantially than similar sensors in the literature.[141,145,147] The high level of sensitivity in this sensor is believed to be due to the lack of use of any ligands, coatings, or additional non-volatile surfactants in the sensor fabrication. Ligands are often incorporated into UV sensors intentionally to reduce dark current and on-off ratios, but introduction of these ligands may adversely affect sensitivity.[139,148]. Other manufacturing techniques for UV sensors require use of ligands in the solution processing of the nanoparticles, which can be difficult to fully remove after patterning is complete.[141,147] Remaining ligands could adversely affect the sensor sensitivity, a problem which is absent in the current manufacturing method. The current sensor could therefore achieve comparable or higher absolute sensitivity by increasing the area of the sensor while maintaining the high quality of fabricated nanoparticle films.

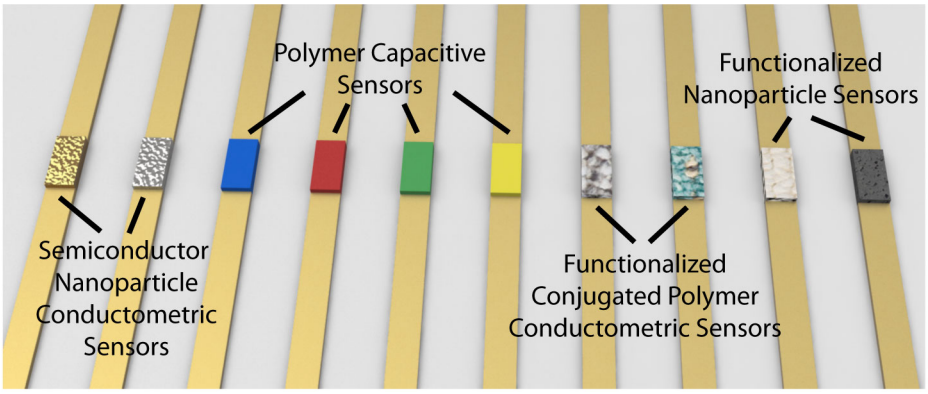

Figure 6.7: A schematic of a multiplexed gas or chemical sensor, incorporating multiple different materials patterned in close proximity and aligned to previously defined electrodes.

6.3 Future Directions

Current work on developing electronics and sensing applications using the current process has been extremely limited. Using an expanded material set, more sensors and electronics applications can be realized. However, in addition to simply using different materials, the unique capability of this process in patterning multiple materials using a single template can be used to pattern multiple sensors in close proximity, creating a multiplexed sensor system, as shown in Figure 6.7. Application of such a manufacturing process to these multiplexed gas or chemical sensors can increase the throughput of the device creation by eliminating patterning steps and therefore lowering the overall cost of the device.

Bibliography

1. Alivisatos, A. P. Perspectives on the physical chemistry of semiconductor nanocrystals. *Journal of Physical Chemistry* **100,** 13226–13239 (1996).
2. Kittel, C. *Introduction to Solid State Physics* Third Edition (John Wiley & Sons, Hoboken, NJ, 2005).
3. Datta, S. *Quantum Transport: Atom to Transistor* (Cambridge University Press, Cambridge, UK, 2005).
4. Kamat, P. V. Photophysical, photochemical and photocatalytic aspects of metal nanoparticles. *Journal of Physical Chemistry B* **106,** 7729–7744 (2002).
5. Shipway, A. N., Katz, E. & Willner, I. Nanoparticle arrays on surfaces for electronic, optical, and sensor applications. *Chemphyschem* **1,** 18–52 (2000).
6. Rivest, J. B., Fong, L.-K., Jain, P. K., Toney, M. F. & Alivisatos, A. P. Size Dependence of a Temperature-Induced Solid-Solid Phase Transition in Copper(I) Sulfide. *Journal of Physical Chemistry Letters* **2,** 2402–2406 (2011).
7. Ko, S. H. *et al.* Direct nanoimprinting of metal nanoparticles for nanoscale electronics fabrication. *Nano Letters* **7,** 1869–1877 (2007).
8. Johnson, B. F. G. Nanoparticles in catalysis. *Topics in Catalysis* **24,** 147–159 (2003).
9. Savage, N. & Diallo, M. S. Nanomaterials and water purification: Opportunities and challenges. *Journal of Nanoparticle Research* **7,** 331–342 (2005).

10. Jin, Y., Wang, J., Sun, B., Blakesley, J. C. & Greenham, N. C. Solution-processed ultraviolet photodetedtors based on colloidal ZnO nanoparticles. *Nano Letters* **8,** 1649–1653 (2008).

11. De lacy Costello, B. P. J., Ewen, R. J., Ratcliffe, N. M. & Richards, M. Highly sensitive room temperature sensors based on the UV-LED activation of zinc oxide nanoparticles. *Sensors and Actuators B-Chemical* **134,** 945–952 (2008).

12. Stenger-Smith, J. D. Intrinsically electrically conducting polymers. Synthesis, characterization, and their applications. *Progress in Polymer Science* **23,** 57–79 (1998).

13. Naumann, R. J. *Introduction to the Physics and Chemistry of Materials* (CRC Press, Boca Raton, FL, 2009).

14. Chiang, C. K. *et al.* Electrical-Conductivity in Doped Polyacetylene. *Physical Review Letters* **39,** 1098–1101 (1977).

15. Huang, W. S., Angelopoulos, M., White, J. R. & Park, J. M. Metallization of Printed-Circuit Boards using Conducting Polyaniline. *Molecular Crystals and Liquid Crystals* **189,** 227–235 (1990).

16. Dimitrakopoulos, C. D. & Malenfant, P. R. L. Organic thin film transistors for large area electronics. *Advanced Materials* **14,** 99–117 (2002).

17. Burroughes, J. H. *et al.* Light-Emitting-Diodes Based on Conjugated Polymers. *Nature* **347,** 539–541 (1990).

18. Pearce, T. C., Gardner, J. W., Friel, S., Bartlett, P. N. & Blair, N. Electronic Nose for Monitoring the Flavor of Beers. *Analyst* **118,** 371–377 (1993).

19. Kaneto, K., Kaneko, M., Min, Y. & Macdiarmid, A. G. Artificial Muscle - Electromechanical Actuators using Polyaniline Films. *Synthetic Metals* **71,** 2211–2212 (1995).

20. Saxena, V., Plum, T. J., Jessing, J. R. & Baker, R. J. Design and fabrication of a MEMS capacitive chemical sensor system. *2006 IEEE Workshop on Microelectronics and Electron Devices* (2006).

21. Bietsch, A., Zhang, J. Y., Hegner, M., Lang, H. P. & Gerber, C. Rapid functionalization of cantilever array sensors by inkjet printing. *Nanotechnology* **15,** 873–880 (2004).

22. Liu, C. Recent developments in polymer MEMS. *Advanced Materials* **19,** 3783–3790 (2007).

23. Liu, Y., Cui, T. H. & Varahramyan, K. All-polymer capacitor fabricated with inkjet printing technique. *Solid-State Electronics* **47,** 1543–1548 (2003).

24. Erbil, H. Y., Demirel, A. L., Avci, Y. & Mert, O. Transformation of a simple plastic into a superhydrophobic surface. *Science* **299,** 1377–1380 (2003).

25. Sze, S. M. & Ng, K. K. *Physics of Semiconductor Devices* Third Edition (John Wiley & Sons, Hoboken, NJ, 2007).

26. Park, I., Li, Z., Pisano, A. P. & Williams, R. S. Top-down fabricated silicon nanowire sensors for real-time chemical detection. **21,** 015501 (2010).

27. Senturia, S. D. *Microsystem Design* (Springer, New York, NY, 2001).

28. Li, T.-L. & Hsu, S. L.-C. Preparation and Properties of Thermally Conductive Photosensitive Polyimide/Boron Nitride Nanocomposites. *Journal of Applied Polymer Science* **121,** 916–922 (2011).

29. Damean, N., Parviz, B. A., Lee, J. N., Odom, T. & Whitesides, G. M. Composite ferromagnetic photoresist for the fabrication of microelectromechanical systems. *Journal of Micromechanics and Microengineering* **15,** 29–34 (2005).

30. Ofir, Y. *pat.* 7846642 (2010).

31. Zhang, A. P. *et al.* Fabrication of submicron structures in nanoparticle/polymer composite by holographic lithography and reactive ion etching. *Applied Physics Letters* **93,** 203509 (2008).

32. Xia, D. Y. & Brueck, S. R. J. A facile approach to directed assembly of patterns of nanoparticles using interference lithography and spin coating. *Nano Letters* **4,** 1295–1299 (2004).

33. Choi, S., Stassi, S., Pisano, A. P. & Zohdi, T. I. Coffee-Ring Effect-Based Three Dimensional Patterning of Micro/Nanoparticle Assembly with a Single Droplet. *Langmuir* **26,** 11690–11698 (2010).

34. Xia, D. Y. & Brueck, S. R. J. Fabrication of enclosed nanochannels using silica nanoparticles. *Journal of Vacuum Science & Technology B* **23,** 2694–2699 (2005).

35. Molnar, G. *et al.* A combined top-down/bottom-up approach for the nanoscale patterning of spin-crossover coordination polymers. *Advanced Materials* **19,** 2163–2167 (2007).

36. Mohammed, J. S., DeCoster, M. A. & McShane, M. J. Fabrication of interdigitated micropatterns of self-assembled polymer nanofilms containing cell-adhesive materials. *Langmuir* **22,** 2738–2746 (2006).

37. Takamatsu, S., Takahata, T., Matsumoto, K. & Shimoyama, I. Micropatterning of a conductive polymer and an insulation polymer using the Parylene lift-off method for electrochromic displays. *Journal of Micromechanics and Microengineering* **21,** 075021 (2011).

38. Xia, D. Y., Li, D., Luo, Y. & Brueck, S. R. J. An approach to lithographically defined self-assembled nanoparticle films. *Advanced Materials* **18,** 930–933 (2006).

39. Winkleman, A. *et al.* Patterning micron-sized features in a cross-linked poly(acrylic acid) film by a wet etching process. *Soft Matter* **3,** 108–116 (2007).

40. Wijshoff, H. The dynamics of the piezo inkjet printhead operation. *Physics Reports-Review Section of Physics Letters* **491,** 77–177 (2010).

41. Le, H. P. Progress and trends in ink-jet printing technology. *Journal of Imaging Science and Technology* **42,** 49–62 (1998).

42. Derby, B. Inkjet Printing of Functional and Structural Materials: Fluid Property Requirements, Feature Stability, and Resolution. *Annual Review of Materials Research, Vol 40* **40,** 395–414 (2010).

43. Hebner, T. R., Wu, C. C., Marcy, D., Lu, M. H. & Sturm, J. C. Ink-jet printing of doped polymers for organic light emitting devices. *Applied Physics Letters* **72,** 519–521 (1998).

44. Shimoda, T., Morii, K., Seki, S. & Kiguchi, H. Inkjet printing of light-emitting polymer displays. *MRS Bulletin* **28,** 821–827 (2003).

45. Sirringhaus, H., Bird, M., Richards, T. & Zhao, N. Charge Transport Physics of Conjugated Polymer Field-Effect Transistors. *Advanced Materials* **22,** 3893–3898 (2010).

46. Hoth, C. N., Choulis, S. A., Schilinsky, P. & Brabec, C. J. High photovoltaic performance of inkjet printed polymer: Fullerene blends. *Advanced Materials* **19,** 3973–3978 (2007).

47. Setti, L. *et al.* An HRP-based amperometric biosensor fabricated by thermal inkjet printing. *Sensors and Actuators B-Chemical* **126,** 252–257 (2007).

48. Mabrook, M. F., Pearson, C. & Petty, M. C. Inkjet-printed polypyrrole thin films for vapour sensing. *Sensors and Actuators B-Chemical* **115,** 547–551 (2006).

49. Huang, D., Liao, F., Molesa, S., Redinger, D. & Subramanian, V. Plastic-compatible low resistance printable gold nanoparticle conductors for flexible electronics. *Journal of the Electrochemical Society* **150,** G412–G417 (2003).

50. Liu, C.-T., Lee, W.-H. & Shih, T.-L. Synthesis of ZnO Nanoparticles to Fabricate a Mask-Free Thin-Film Transistor by Inkjet Printing. *Journal of Nanotechnology* **2012,** 710908 (2012).

51. Wu, Y., Tamaki, T., Volotinen, T., Lova, L. B. & Rao, K. V. Enhanced Photoresponse of Inkjet-Printed ZnO Thin Films Capped with CdS Nanoparticles. *Journal of Physical Chemistry Letters* **1,** 89–92 (2010).

52. Conedera, V., Yoboue, P., Mesnilgrente, F., Fabre, N. & Menini, P. Manufacturability of gas sensor with ZnO nanoparticles suspension deposited by ink jet printing. *Proceedings of the SPIE - The International Society for Optical Engineering* **7590** (2010).

53. Bernacka-Wojcik, I. *et al.* Inkjet printed and "doctor blade" TiO(2) photodetectors for DNA biosensors. *Biosensors & bioelectronics* **25,** 1229–1234 (2010).

54. Brookfield, J. M. *et al. pat.* 6969146 (2004).

55. Yun, Y. H., Kim, J. D., Lee, B. K., Cho, Y. W. & Lee, H. Y. Polymer Inkjet Printing: Construction of Three-Dimensional Structures at Micro-Scale by Repeated Lamination. *Macromolecular Research* **17,** 197–202 (2009).

56. Sirringhaus, H. *et al.* High-resolution inkjet printing of all-polymer transistor circuits. *Science* **290,** 2123–2126 (2000).

57. S., L. R. F. R. On the equilibrium of liquid conducting masses charged with electricity. *Philosophical Magazine* **5,** 184–186 (1884).

58. Cooley, J. F. *pat.* 692631 (1902).

59. Morton, W. J. *pat.* 705691 (1902).

60. Teo, W. E. & Ramakrishna, S. A review on electrospinning design and nanofibre assemblies. **17,** R89–R106 (2006).

61. Park, J.-U. *et al.* High-resolution electrohydrodynamic jet printing. *Nature Materials* **6,** 782–789 (2007).

62. Chang, C., Limkrailassiri, K. & Lin, L. Continuous near-field electrospinning for large area deposition of orderly nanofiber patterns. *Applied Physics Letters* **93,** 123111 (2008).

63. Sun, D. H., Chang, C., Li, S. & Lin, L. W. Near-field electrospinning. *Nano Letters* **6,** 839–842 (2006).

64. Lee, D.-Y., Shin, Y.-S., Park, S.-E., Yu, T.-U. & Hwang, J. Electrohydrodynamic printing of silver nanoparticles by using a focused nanocolloid jet. *Applied Physics Letters* **90,** 081905 (2007).

65. Kapur, N. *et al.* A Review of Gravure Coating Systems. *Convertech & e-Print* **1,** 56–60 (2011).

66. Puetz, J. & Aegerter, M. A. Direct gravure printing of indium tin oxide nanoparticle patterns on polymer foils. *Thin Solid Films* **516,** 4495–4501 (2008).

67. Pudas, M., Halonen, N., Granat, P. & Vahakangas, J. Gravure printing of conductive particulate polymer inks on flexible substrates. *Progress in Organic Coatings* **54,** 310–316 (2005).

68. Hambsch, M. *et al.* Uniformity of fully gravure printed organic field-effect transistors. *Materials Science and Engineering B-Advanced Functional Solid-State Materials* **170,** 93–98 (2010).

69. Makela, T., Haatainen, T., Majander, P. & Ahopelto, J. Continuous roll to roll nanoimprinting of inherently conducting polyaniline. *Microelectronic Engineering* **84,** 877–879 (2007).

70. Sung, D., de la Fuente Vornbrock, A. & Subramanian, V. Scaling and Optimization of Gravure-Printed Silver Nanoparticle Lines for Printed Electronics. *Ieee Transactions on Components and Packaging Technologies* **33,** 105–114 (2010).

71. Gonzalez-Macia, L., Morrin, A., Smyth, M. R. & Killard, A. J. Advanced printing and deposition methodologies for the fabrication of biosensors and biodevices. *Analyst* **135,** 845–867 (2010).

72. Aernouts, T. *et al.* Printable anodes for flexible organic solar cell modules. *Thin Solid Films* **451,** 22–25 (2004).

73. Verilhac, J.-M. *et al.* Step toward robust and reliable amorphous polymer field-effect transistors and logic functions made by the use of roll to roll compatible printing processes. *Organic Electronics* **11,** 456–462 (2010).

74. Birnstock, J. *et al.* Screen-printed passive matrix displays based on light-emitting polymers. *Applied Physics Letters* **78,** 3905–3907 (2001).

75. Krebs, F. C. *et al.* A complete process for production of flexible large area polymer solar cells entirely using screen printing-First public demonstration. *Solar Energy Materials and Solar Cells* **93,** 422–441 (2009).

76. Llobet, E. *et al.* Screen-printed nanoparticle tin oxide films for high-yield sensor microsystems. *Sensors and Actuators B-Chemical* **96,** 94–104 (2003).

77. Harting, M., Zhang, J., Gamota, D. R. & Britton, D. T. Fully printed silicon field effect transistors. *Applied Physics Letters* **94,** 193509 (2009).

78. Parashkov, R., Becker, E., Riedl, T., Johannes, H. H. & Kowalsky, W. Large area electronics using printing, methods. *Proceedings of the IEEE* **93,** 1321–1329 (2005).

79. Kerp, H., Arola, D., Cruz, B., Eijk, P. V. & Shaikh, A. in *Proceedings of the 24th European Photovoltaic Solar Energy Conference* (Hamburg, Germany, 2009), 1499–1501.

80. Chou, S. Y., Krauss, P. R. & Renstrom, P. J. Imprint of Sub-25 Nm Vias and Trenches in Polymers. *Applied Physics Letters* **67,** 3114–3116 (1995).

81. Kemme, S. *Microoptics and Nanooptics Fabrication* 128–147 (CRC Press, Boca Raton, FL, 2009).

82. Balla, T., Spearing, S. M. & Monk, A. An assessment of the process capabilities of nanoimprint lithography. *Journal of Physics D-Applied Physics* **41,** 174001 (2008).

83. Menard, E. *et al.* Micro- and nanopatterning techniques for organic electronic and optoelectronic systems. *Chemical reviews* **107,** 1117–1160 (2007).

84. Austin, M. D. & Chou, S. Y. Fabrication of 70 nm channel length polymer organic thin-film transistors using nanoimprint lithography. *Applied Physics Letters* **81,** 4431–4433 (2002).

85. Li, M. T., Wang, J. A., Zhuang, L. & Chou, S. Y. Fabrication of circular optical structures with a 20 nm minimum feature size using nanoimprint lithography. *Applied Physics Letters* **76,** 673–675 (2000).

86. Koev, S. T. *et al.* Chitosan: an integrative biomaterial for lab-on-a-chip devices. *Lab on a Chip* **10,** 3026–3042 (2010).

87. Nie, Z. & Kumacheva, E. Patterning surfaces with functional polymers. *Nature Materials* **7,** 277–290 (2008).

88. Hirai, Y. *et al.* High aspect pattern fabrication by nano imprint lithography using fine diamond mold. *Japanese Journal of Applied Physics Part 1-Regular Papers Short Notes & Review Papers* **42,** 3863–3866 (2003).

89. Wang, Q., Hiroshima, H., Atobe, H. & Youn, S.-W. Residual layer uniformity using complementary patterns to compensate for pattern density variation in UV nanoimprint lithography. *Journal of Vacuum Science & Technology B* **28,** C6M125–C6M129 (2010).

90. Lazzarino, F., Gourgon, C., Schiavone, P. & Perret, C. Mold deformation in nanoimprint lithography. *Journal of Vacuum Science & Technology B* **22,** 3318–3322 (2004).

91. Park, I. *et al.* Nanoscale patterning and electronics on flexible substrate by direct nanoimprinting of metallic nanoparticles. *Advanced Materials* **20,** 489–496 (2008).

92. Lee, J. N., Park, C. & Whitesides, G. M. Solvent compatibility of poly(dimethylsiloxane)-based microfluidic devices. *Analytical Chemistry* **75** (2003).

93. Kim, E., Xia, Y. N. & Whitesides, G. M. Polymer Microstructures Formed by Molding in Capillaries. *Nature* **376,** 581–584 (1995).

94. Donthu, S. K. *et al.* Near-field scanning optical microscopy of ZnO nanopatterns fabricated by micromolding in capillaries. *Journal of Applied Physics* **98,** 024304 (2005).

95. Bluemel, A. *et al.* Micromolding in capillaries and microtransfer printing of silver nanoparticles as soft-lithographic approach for the fabrication of source/drain electrodes in organic field-effect transistors. *Organic Electronics* **8,** 389–395 (2007).

96. Richter, T. V. *et al.* Room temperature vacuum-induced ligand removal and patterning of ZnO nanoparticles: from semiconducting films towards printed electronics. *Journal of Materials Chemistry* **20,** 874–879 (2010).

97. Martin, C. R. & Aksay, I. A. Microchannel molding: A soft lithography-inspired approach to micrometer-scale patterning. *Journal of Materials Research* **20,** 1995–2003 (2005).

98. Kim, E., Xia, Y. N., Zhao, X. M. & Whitesides, G. M. Solvent-assisted microcontact molding: A convenient method for fabricating three-dimensional structures on surfaces of polymers. *Advanced Materials* **9,** 651–654 (1997).

99. Kim, Y. S., Suh, K. Y. & Lee, H. H. Fabrication of three-dimensional microstructures by soft molding. *Applied Physics Letters* **79,** 2285–2287 (2001).

100. Kim, Y. S., Park, J. & Lee, H. H. Three-dimensional pattern transfer and nanolithography: modified soft molding. *Applied Physics Letters* **81,** 1011–1013 (2002).

101. Randall, G. C. & Doyle, P. S. Permeation-driven flow in poly(dimethylsiloxane) microfluidic devices. *Proceedings of the National Academy of Sciences of the United States of America* **102,** 10813–10818 (2005).

102. Bhardwaj, R., Fang, X., Somasundaran, P. & Attinger, D. Self-Assembly of Colloidal Particles from Evaporating Droplets: Role of DLVO Interactions and Proposition of a Phase Diagram. *Langmuir* **26,** 7833–7842 (2010).

103. Deegan, R. D. *et al.* Capillary flow as the cause of ring stains from dried liquid drops. *Nature* **389,** 827–829 (1997).

104. Vrij, A. Possible Mechanism for Spontaneous Rupture of Thin Free Liquid Films. *Discussions of the Faraday Society,* 23–33 (1966).

105. Thomas, D. K. & Thomas, T. A. J. Viscosity-Concentration Relationships in Solutions of High Polymers. *Journal of Applied Polymer Science* **3,** 129–131 (1960).

106. Mooney, M. The Viscosity of a Concentrated Suspension of Spherical Particles. *Journal of Colloid Science* **6,** 162–170 (1951).

107. Chen, C.-N., Huang, C.-T., Tseng, W. J. & Wei, M.-H. Dispersion and rheology of surfactant-mediated silver nanoparticle suspensions. *Applied Surface Science* **257,** 650–655 (2010).

108. White, F. M. *Viscous Fluid Flow* 109–117 (McGraw-Hill, New York, 2006).

109. Budd, P. M. & McKeown, N. B. Highly permeable polymers for gas separation membranes. *Polymer Chemistry* **1,** 63–68 (2010).

110. Nagai, K., Masuda, T., Nakagawa, T., Freeman, B. D. & Pinnau, I. Poly[1-(trimethylsilyl)-1-propyne] and related polymers: synthesis, properties and functions. *Progress in Polymer Science* **26,** 721–798 (2001).

111. Robeson, L. M. Polymer membranes for gas separation. *Current Opinion in Solid State & Materials Science* **4,** 549–552 (1999).

112. Hu, Y., Shiotsuki, M., Sanda, F., Freeman, B. D. & Masuda, T. Synthesis and Properties of Indan-Based Polyacetylenes That Feature the Highest Gas Permeability among All the Existing Polymers. *Macromolecules* **41,** 8525–8532 (2008).

113. Pinnau, I., Morisato, A. & He, Z. J. Influence of side-chain length on the gas permeation properties of poly(2-alkylacetylenes). *Macromolecules* **37,** 2823–2828 (2004).

114. Toy, L. G. *et al.* Pure-gas and vapor permeation and sorption properties of poly[1-phenyl-2-[p-(trimethylsilyl)phenyl]acetylene] (PTMSDPA). *Macromolecules* **33,** 2516–2524 (2000).

115. Merkel, T. C., Bondar, V. I., Nagai, K., Freeman, B. D. & Pinnau, I. Gas sorption, diffusion, and permeation in poly(dimethylsiloxane). *Journal of Polymer Science Part B-Polymer Physics* **38** (2000).

116. Raharjo, R. D., Freeman, B. D., Paul, D. R., Sarti, G. C. & Sanders, E. S. Pure and mixed gas CH4 and n-C4H10 permeability and diffusivity in poly (dimethylsiloxane). *Journal of Membrane Science* **306,** 75–92 (2007).

117. Bi, J. *et al.* Effects of solvent in the casting of poly(1-trimethylsilyl-1-propyne) membranes. *Radiation Physics and Chemistry* **58,** 563–566 (2000).

118. Claes, S. *et al.* Crosslinked poly[1-(trimethylsilyl)-1-propyne] membranes: Characterization and pervaporation of aqueous tetrahydrofuran mixtures. *Journal of Membrane Science* **389,** 459–469 (2012).

119. Feron, P. H. M., Volkov, V. V., Khotimsky, V. S. & Teplyakov, V. V. *pat.* 7591878 (2009).

120. Volkov, A. V. *et al.* High permeable PTMSP/PAN composite membranes for solvent nanofiltration. *Journal of Membrane Science* **333,** 88–93 (2009).

121. Morisato, A. & Pinnau, I. Synthesis and gas permeation properties of poly(4-methyl-2-pentyne). *Journal of Membrane Science* **121,** 243–250 (1996).

122. Shao, L., Samseth, J. & Hagg, M.-B. Crosslinking and stabilization of high fractional free volume polymers for gas separation. *International Journal of Greenhouse Gas Control* **2,** 492–501 (2008).

123. Masuda, T., Kawasaki, M., Okano, Y. & Higashimura, T. Polymerization of Aliphatic Acetylenes - Polymerization of Methylpentynes by Transition-Metal Catalysts - Monomer Structure, Reactivity, and Polymer Properties. *Polymer Journal* **14,** 371–377 (1982).

124. Gere, J. M. *Mechanics of Materials* Sixth, 906 (Thomson, Belmont, CA, 2004).

125. Croll, S. G. Internal-Stress in a Solvent-Cast Thermoplastic Coating. *Journal of Coatings Technology* **50,** 33–38 (1978).

126. De Gennes, P.-G., Brochard-Wyart, F. & Quere, D. *Capillarity and Wetting Phenomena* (Springer, New York, NY, 2004).

127. Buffat, P. & Borel, J. P. Size Effect on Melting Temperature of Gold Particles. *Physical Review A* **13,** 2287–2298 (1976).

128. Guisbiers, G., Kazan, M., Overschelde, O. V., Wautelet, M. & Pereira, S. Mechanical and thermal properties of metallic and semiconductive nanostructures. *Journal of Physical Chemistry C* **112,** 4097–4103 (2008).

129. Brust, M., Walker, M., Bethell, D., Schiffrin, D. J. & Whyman, R. Synthesis of Thiol-Derivatized Gold Nanoparticles in a 2-Phase Liquid-Liquid System. *Journal of the Chemical Society-Chemical Communications,* 801–802 (1994).

130. Moon, S. Y., ichiro Tanaka, S. & Sekino, T. Crystal Growth of Thiol-Stabilized Gold Nanoparticles by Heat-Induced Coalescence. *Nanoscale Research Letters* **5,** 813–817 (2010).

131. Wu, Y., Li, Y., Liu, P., Gardner, S. & Ong, B. S. Studies of gold nanoparticles as precursors to printed conductive features for thin-film transistors. *Chemistry of Materials* **18,** 4627–4632 (2006).

132. Samarasinghe, S. R., Pastoriza-Santos, I., Edirisinghe, M. J., Reece, M. J. & Liz-Marzan, L. M. Printing gold nanoparticles with an electrohydrodynamic direct-write device. *Gold Bulletin* **39,** 48–53 (2006).

133. Wang, K. & Stark, J. P. W. Deposition of colloidal gold nanoparticles by fully pulsed-voltage-controlled electrohydrodynamic atomisation. *Journal of Nanoparticle Research* **12,** 707–711 (2010).

134. Kraus, T. *et al.* Nanoparticle printing with single-particle resolution. *Nature Nanotechnology* **2,** 570–576 (2007).

135. Bieri, N. R., Chung, J., Haferl, S. E., Poulikakos, D. & Grigoropoulos, C. P. Microstructuring by printing and laser curing of nanoparticle solutions. *Applied Physics Letters* **82,** 3529–3531 (2003).

136. Cui, W. *et al.* Gold nanoparticle ink suitable for electric-conductive pattern fabrication using in ink-jet printing technology. *Colloids and Surfaces A - Physicochemical and Engineering Aspects* **358,** 35–41 (2010).

137. Xu, J. Q., Pan, Q. Y., Shun, Y. A. & Tian, Z. Z. Grain size control and gas sensing properties of ZnO gas sensor. *Sensors and Actuators B-Chemical* **66,** 277–279 (2000).

138. Ra, Y.-W., Choi, K.-S., Kim, J.-H., Hahn, Y.-B. & Im, Y.-H. Fabrication of ZnO nanowires using nanoscale spacer lithography for gas sensors. *Small* **4,** 1105–1109 (2008).

139. Qin, L., Shing, C. & Sawyer, S. Metal-Semiconductor-Metal Ultraviolet Photodetectors Based on Zinc-Oxide Colloidal Nanoparticles. *IEEE Electron Device Letters* **32,** 51–53 (2011).

140. Jun, J. H., Seong, H., Cho, K., Moon, B. M. & Kim, S. Ultraviolet photodetectors based on ZnO nanoparticles. *Ceramics International* **35,** 2797–2801 (2009).

141. Jin, Y. Z., Wang, J. P., Sun, B. Q., Blakesley, J. C. & Greenham, N. C. Solution-processed ultraviolet photodetedtors based on colloidal ZnO nanoparticles. *Nano Letters* **8,** 1649–1653 (2008).

142. Incropera, F. P. & Dewitt, D. P. *Introduction to Heat Transfer* 682 (Wiley, New York, NY, 1996).

143. Keem, K. *et al.* Photocurrent in ZnO nanowires grown from Au electrodes. *Applied Physics Letters* **84,** 4376–4378 (2004).

144. Li, Q. H., Gao, T., Wang, Y. G. & Wang, T. H. Adsorption and desorption of oxygen probed from ZnO nanowire films by photocurrent measurements. *Applied Physics Letters* **86,** 123117 (2005).

145. Bhat, S. V., Vivekchand, S. R. C., Govindaraj, A. & Rao, C. N. R. Photoluminescence and photoconducting properties of ZnO nanoparticles. *Solid State Communications,* 510–514 (2009).

146. Kind, H., Yan, H. Q., Messer, B., Law, M. & Yang, P. D. Nanowire ultraviolet photodetectors and optical switches. *Advanced Materials* **14,** 158–160 (2002).

147. Carrey, J. *et al.* Photoconductivity of self-assembled ZnO nanoparticles synthesized by organometallic chemistry. *Semiconductor Science and Technology* **23,** 025003 (2008).

148. Qin, L. Q., Shing, C., Sawyer, S. & Dutta, P. S. Enhanced ultraviolet sensitivity of zinc oxide nanoparticle photoconductors by surface passivation. *Optical Materials* **33,** 359–362 (2011).

149. Gill, W. N. & Sankaras.R. Exact Analysis of Unsteady Convective Diffusion. *Proceedings of the Royal Society of London Series A- Mathematical and Physical Sciences* **316,** 341–350 (1970).

150. Doshi, M. R., Daiya, P. M. & Gill, W. N. 3 Dimensional Laminar Dispersion in Open and Closed Rectangular Conduits. *Chemical Engineering Science* **33,** 795–804 (1978).

Appendices

Appendix A

An Analysis of Taylor Dispersion in a Cylindrical Duct

In this appendix, the effective diffusion constant for solute dispersion in a cylindrical duct is determined. This is done in order to enable use of the simplified, one-dimensional model for flow and solute concentrations in the template during nanoparticle or polymer patterning that is developed in Chapter 3. The derivation follows the method previously developed by Gill et al.[149] A steady flow of fluid containing solute is analyzed in three dimensions and the cross-sectional averaged solute density is then used to determine the effective diffusivity that must be used to accurately predict solute concentrations in a one-dimensional model.

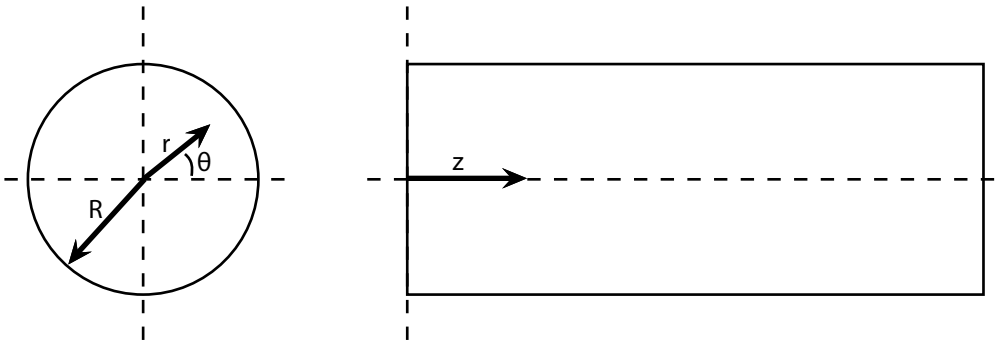

Figure A.1: An illustration of the cylindrical domain, with dimensions and coordinates defined.

A.1 Fluid Flow in a Cylindrical Duct

The velocity distribution $u_z(r)$ of fluid flowing through a cylindrical duct of radius R is desired. This domain is shown in Figure A.1. The axial coordinate is z, and the coordinates in the cross section are described by the radial position r and the angle θ. The governing equations for this low Reynolds number flow describe a balance between pressure P and viscosity η, given by

$$\frac{\partial P}{\partial z} = \eta \nabla^2 u_z \tag{A.1}$$

$$\frac{\partial P}{\partial r} = 0 \tag{A.2}$$

$$\frac{1}{r}\frac{\partial P}{\partial \theta} = 0 \tag{A.3}$$

These three equations can be reduced into a single momentum equation given by

$$\frac{dP}{dz} = \eta \nabla^2 u_z \tag{A.4}$$

The boundary conditions for this flow are

$$u_z = 0 \qquad \text{at } r = R \tag{A.5}$$

$$u_z = \text{ finite} \qquad \text{at } r = 0 \tag{A.6}$$

For this flow, cylindrical symmetry allows the above equation to be written as

$$\frac{dP}{dz} = \eta \frac{1}{r}\frac{\partial}{\partial r}\left(r\frac{\partial u_z}{\partial r}\right) \tag{A.7}$$

Integrating this equation twice with respect to r gives

$$u_z = \frac{1}{4\eta}\frac{dP}{dz}r^2 + C_1 \ln r + C_2 \tag{A.8}$$

where C_1 and C_2 are constants of integration. These constants can be determined by applying the boundary conditions, Equations A.5 and A.6. This results in

$$u_z = \frac{1}{4\eta}\frac{dP}{dz}\left(r^2 - R^2\right) \tag{A.9}$$

This solution can be written in terms of the maximum velocity in the flow, U_m, which results in

$$u_z = U_m \left(1 - \frac{r^2}{R^2}\right) \tag{A.10}$$

It is also useful to find the average velocity of fluid in the channel, U_{avg}. This is done using

$$U_{avg} = \frac{1}{\pi R^2} \int_0^R u_z 2\pi r dr \tag{A.11}$$

Performing the integration results in

$$U_{avg} = \frac{U_m}{2} \tag{A.12}$$

A.2 Solute Dispersion a Cylindrical Duct

The effective diffusion constant for an equivalent one dimensional model is found by observing the dispersion of solute injected instantaneously at time $t = 0$. The concentration of solute as a function of location in the conduit and elapsed time, $C(t, r, z)$, is therefore desired. A mass balance on the system considering both convection and diffusion of particles results in a governing equation that can be written as

$$\frac{\partial C}{\partial t} + u_z \frac{\partial C}{\partial z} = D \left[\frac{1}{r}\frac{\partial}{\partial r}\left(r\frac{\partial C}{\partial r}\right) + \frac{\partial^2 C}{\partial z^2}\right] \tag{A.13}$$

where D is the diffusion coefficient for the solute. The initial condition is given by a pulse of solute, injected at the left side of the channel at z=0 and at time t=0, and may be described by

$$C(0, r, z) = \delta(z) C_0 \tag{A.14}$$

where $\delta(\zeta)$ is the Dirac delta function and C_0 is the constant initial concentration. The boundary conditions are obtained by noting the symmetry of the system about the origin, and by requiring that there be zero flux of particles through the wall and that the concentration of particles far from the source along the axial direction be zero. The boundary conditions are therefore given by

$$\left.\frac{\partial C}{\partial r}\right|_{r=0,R} = 0 \tag{A.15}$$

$$\lim_{r\to 0} C = \text{ finite} \tag{A.16}$$

$$\lim_{z\to\infty} C = \lim_{z\to\infty} \frac{\partial C}{\partial z} = 0 \tag{A.17}$$

In the subsequent analysis, it will be necessary to calculate the mean concentration of particles, $C_m(t,z)$, which may be defined by

$$C_m = \frac{1}{\pi R^2}\int_0^R C 2\pi r dr \tag{A.18}$$

Additionally, it will be useful to expand the concentration of solute in a Taylor series about the mean concentration with respect to the distance along the length of the channel. This expansion is given by

$$C = \sum_{n=0}^{\infty} f_n \frac{\partial^n C_m}{\partial z^n} \tag{A.19}$$

where $f_n(t,r)$ is the n$^{\text{th}}$ coefficient of the Taylor series expansion.

A generalized dispersion equation is found by averaging the convective diffusion equation, Equation A.13, over the cross sectional area of the duct, resulting in

$$\frac{1}{\pi R^2}\int_0^R \left(\frac{\partial C}{\partial t} + u_z\frac{\partial C}{\partial z}\right) 2\pi r dr = \frac{D}{\pi R^2}\int_0^R \left[\frac{1}{r}\frac{\partial}{\partial r}\left(r\frac{\partial C}{\partial r}\right) + \frac{\partial^2 C}{\partial z^2}\right] 2\pi r dr \tag{A.20}$$

$$\frac{\partial C_m}{\partial t} + \frac{1}{\pi R^2}\int_0^R \left(\frac{\partial}{\partial z}C u_z\right) 2\pi r dr = \frac{D}{\pi R^2}\left(2\pi r\frac{\partial C}{\partial r}\right)\Bigg|_0^R + D\frac{\partial^2 C_m}{\partial z^2} \tag{A.21}$$

$$\frac{\partial C_m}{\partial t} + \frac{2}{R^2}\int_0^R \left(\frac{\partial}{\partial z}C u_z\right) r dr = D\frac{\partial^2 C_m}{\partial z^2} \tag{A.22}$$

$$\frac{\partial C_m}{\partial t} = D\frac{\partial^2 C_m}{\partial z^2} - \frac{2}{R^2}\frac{\partial}{\partial z}\int_0^R C u_z r dr \tag{A.23}$$

Substituting the expression for the concentration expanded about the mean, Equation A.19, results in

$$\frac{\partial C_m}{\partial t} = D\frac{\partial^2 C_m}{\partial z^2} - \frac{2}{R^2}\frac{\partial}{\partial z}\int_0^R \sum_{n=0}^{\infty}\left(f_n\frac{\partial^n C_m}{\partial z^n}\right) u_z r dr \tag{A.24}$$

$$\frac{\partial C_m}{\partial t} = D\frac{\partial^2 C_m}{\partial z^2} - \frac{2}{R^2}\int_0^R \sum_{n=0}^{\infty}\left(f_n \frac{\partial^{n+1} C_m}{\partial z^{n+1}}\right) u_z r dr \tag{A.25}$$

$$\frac{\partial C_m}{\partial t} = D\frac{\partial^2 C_m}{\partial z^2} - \frac{2}{R^2}\int_0^R \sum_{n=1}^{\infty}\left[\left(f_{n-1} \frac{\partial^{n} C_m}{\partial z^{n}}\right) u_z\right] r dr \tag{A.26}$$

$$\frac{\partial C_m}{\partial t} = \sum_{n=1}^{\infty}\left[-\frac{2}{R^2}\int_0^R \left(f_{n-1} \frac{\partial^{n} C_m}{\partial z^{n}}\right) u_z r dr + D\frac{\partial^n C_m}{\partial z^n}\delta_{n2}\right] \tag{A.27}$$

$$\frac{\partial C_m}{\partial t} = \sum_{n=1}^{\infty}\left[-\frac{2}{R^2}\int_0^R \left(f_{n-1} u_z\right) r dr + D\delta_{n2}\right] \frac{\partial^n C_m}{\partial z^n} \tag{A.28}$$

where δ_{mn} is the Kronecker delta. This result can be put in the form

$$\frac{\partial C_m}{\partial t} = \sum_{n=1}^{\infty} k_n \frac{\partial^n C_m}{\partial z^n} \tag{A.29}$$

where

$$k_n = -\frac{2}{R^2}\int_0^R \left(f_{n-1} u_z\right) r dr + D\delta_{n2} \tag{A.30}$$

The values of k_n are the coefficients that relate the time derivative of the mean concentration to the spatial derivatives. The second coefficient, k_2, which relates the time derivative to the second spatial derivative, acts like a diffusion coefficient. This is the desired effective diffusion coefficient for the mean concentration which can be used in the one dimensional model. This effective diffusion coefficient accounts for the shear enhanced diffusion present in the three dimensional system, allowing accurate prediction of particle concentrations in the simplified model.

An equation for f_n, required for calculation of the various values of k_n, can be found by substituting the expanded form of the concentration function, Equation A.19, into the convective diffusion equation, Equation A.13. This results in

$$\begin{aligned} &\frac{\partial}{\partial t}\left(\sum_{n=0}^{\infty} f_n \frac{\partial^n C_m}{\partial z^n}\right) + u_z \frac{\partial}{\partial z}\left(\sum_{n=0}^{\infty} f_n \frac{\partial^n C_m}{\partial z^n}\right) = \\ &D\sum_{n=0}^{\infty}\left(\frac{1}{r}\frac{\partial}{\partial r}\left[r\frac{\partial}{\partial r}\left(f_n \frac{\partial^n C_m}{\partial z^n}\right)\right] + \frac{\partial^2}{\partial z^2}\left[f_n \frac{\partial^n C_m}{\partial z^n}\right]\right) \end{aligned} \tag{A.31}$$

$$\sum_{n=0}^{\infty}\left(\frac{\partial f_n}{\partial t}\frac{\partial^n C_m}{\partial z^n}+f_n\frac{\partial^n}{\partial z^n}\frac{\partial C_m}{\partial t}\right)+u_z f_n\frac{\partial^{n+1}C_m}{\partial z^{n+1}}= D\sum_{n=0}^{\infty}\left(\frac{1}{r}\frac{\partial}{\partial r}\left[r\frac{\partial}{\partial r}\left(f_n\frac{\partial^n C_m}{\partial z^n}\right)\right]+f_n\frac{\partial^{n+2}C_m}{\partial z^{n+2}}\right) \tag{A.32}$$

Using the expression for the time derivative of the mean concentration as given in Equation A.29 results in

$$\sum_{n=0}^{\infty}\left[\frac{\partial f_n}{\partial t}\frac{\partial^n C_m}{\partial z^n}+f_n\frac{\partial^n}{\partial z^n}\sum_{j=1}^{\infty}\left(k_j\frac{\partial^j C_m}{\partial z^j}\right)+u_z f_n\frac{\partial^{n+1}C_m}{\partial z^{n+1}}\right]= D\sum_{n=0}^{\infty}\left(\frac{1}{r}\frac{\partial}{\partial r}\left[r\frac{\partial}{\partial r}\left(f_n\frac{\partial^n C_m}{\partial z^n}\right)\right]+f_n\frac{\partial^{n+2}C_m}{\partial z^{n+2}}\right) \tag{A.33}$$

$$\sum_{n=0}^{\infty}\left[\frac{\partial f_n}{\partial t}\frac{\partial^n C_m}{\partial z^n}+f_n\sum_{j=1}^{\infty}\left(k_j\frac{\partial^{j+n} C_m}{\partial z^{j+n}}\right)+u_z f_n\frac{\partial^{n+1}C_m}{\partial z^{n+1}}\right]= D\sum_{n=0}^{\infty}\left(\frac{1}{r}\frac{\partial}{\partial r}\left[r\frac{\partial}{\partial r}\left(f_n\frac{\partial^n C_m}{\partial z^n}\right)\right]+f_n\frac{\partial^{n+2}C_m}{\partial z^{n+2}}\right) \tag{A.34}$$

The equation for the function f_n is then found by equating the coefficients of derivatives having equivalent order. This results in

$$\frac{\partial f_n}{\partial t}+\sum_{j=1}^{\infty}k_j f_{n-j}+u_z f_{n-1}=D\left[\frac{1}{r}\frac{\partial}{\partial r}\left(r\frac{\partial f_n}{\partial r}\right)+f_{n-2}\right] \tag{A.35}$$

The boundary conditions for this equation are found by substituting the expanded form of the concentration, Equation A.19, into the boundary condition on the original convective diffusion equation, Equation A.15. This results in

$$\left.\frac{\partial f_n}{\partial r}\right|_{r=0,R}=0 \tag{A.36}$$

The initial condition is found in a similar manner, by substituting Equation A.19 into Equation A.14, resulting in

$$\left.\sum_{n=0}^{\infty}f_n(t,r)\frac{\partial^n C_m}{\partial z^n}\right|_{t=0}=\delta(z)C_0 \tag{A.37}$$

At time $t = 0$, the mean concentration is simply C_0 for $z = 0$ and is equal to zero otherwise. Therefore

$$\sum_{n=0}^{\infty} f_n(t,r) \frac{\partial^n}{\partial z^n} C_0 \delta(z) \bigg|_{t=0} = \delta(z) C_0 \tag{A.38}$$

$$f_n(0,r) = 1 \tag{A.39}$$

At this point, Equation A.35 can be solved for f_0. The equation for f_0 is reduced to

$$\frac{\partial f_0}{\partial t} = D \frac{1}{r} \frac{\partial}{\partial r} \left(r \frac{\partial f_0}{\partial r} \right) \tag{A.40}$$

This equation can be solved using separation of variables. After solving and applying the boundary conditions from Equation A.36, the expression for f_0 is

$$f_0 = \sum_{m=0}^{\infty} A_m J_0(\mu_m r) \exp(-D\mu_m^2 t) \tag{A.41}$$

where J_0 is the Bessel function of order zero, A_m is a constant of integration, and μ_m is the mth eigenvalue. Applying the initial condition of Equation A.39 results in the determination that

$$A_m = \begin{cases} 1 & \text{for } m = 0 \\ 0 & \text{for } m \neq 0 \end{cases} \tag{A.42}$$

Therefore, the expression for f_0 reduces to

$$f_0 = 1 \tag{A.43}$$

With f_0 determined, k_1 can be found. The expression for k_1 is reduced from Equation A.30, resulting in

$$k_1 = -\frac{2}{R^2} \int_0^R U(r) r dr \tag{A.44}$$

Substituting for the velocity from Equation A.10 and performing the integration results in

$$k_1 = -\frac{2}{R^2} \int_0^R U_m \left(1 - \frac{r^2}{R^2} \right) r dr \tag{A.45}$$

$$k_1 = -\frac{U_m}{2} \tag{A.46}$$

With k_1 determined, an expression for f_1 may now be sought. Again returning to the fundamental equation for f_n, Equation A.35, and reducing the equation to solve for f_1, the result is obtained that

$$\frac{\partial f_1}{\partial t} + k_1 + u_z = D\left[\frac{1}{r}\frac{\partial}{\partial r}\left(r\frac{\partial f_0}{\partial r}\right)\right] \tag{A.47}$$

$$\frac{\partial f_1}{\partial t} - \frac{U_m}{2} + U_m\left(1 - \frac{r^2}{R^2}\right) = D\left[\frac{1}{r}\frac{\partial}{\partial r}\left(r\frac{\partial f_0}{\partial r}\right)\right] \tag{A.48}$$

The solution to this equation, which satisfies boundary condition of Equation A.36, is given by

$$f_1 = \frac{U_m}{D}\left(\frac{r^2}{8} - \frac{r^4}{16R^2} - \frac{R^2}{24}\right) + \sum_{m=0}^{\infty} B_m J_0(\lambda_m r)\exp(-D\lambda_m^2 t) \tag{A.49}$$

where the eigenvalues λ_m and constants B_m can be determined by applying boundary and initial conditions, Equations A.36 and A.39. However, a detailed solution for this variable is not necessary here since only the steady state solution is of relevance to the current work. With the form of f_1 determined, the dispersion coefficient k_2 can now be found. From Equation A.30,

$$k_2 = -\frac{2}{R^2}\int_0^R u_z f_1 r dr + D \tag{A.50}$$

$$\begin{aligned} k_2 = D - \frac{2}{R^2}\int_0^R U_m\left(1 - \frac{r^2}{R^2}\right) \\ \times\left[\frac{U_m}{D}\left(\frac{r^2}{8} - \frac{r^4}{16R^2} - \frac{R^2}{24}\right) + \sum_{m=0}^{\infty} B_m J_0(\lambda_m r)\exp(-D\lambda_m^2 t)\right] r dr \end{aligned} \tag{A.51}$$

The dispersion coefficient of interest is that of the steady-state flow, as $t \to \infty$. As a result, the expression for the dispersion coefficient can be simplified to

$$k_2 = D - \frac{2}{R^2}\int_0^R U_m\left(1 - \frac{r^2}{R^2}\right)\left[\frac{U_m}{D}\left(\frac{r^2}{8} - \frac{r^4}{16R^2} - \frac{R^2}{24}\right)\right] r dr \tag{A.52}$$

$$k_2 = D - \frac{2U_m^2}{DR^2}\int_0^R \left(1 - \frac{r^2}{R^2}\right)\left(\frac{r^2}{8} - \frac{r^4}{16R^2} - \frac{R^2}{24}\right) r dr \tag{A.53}$$

$$k_2 = D + \frac{R^2 U_m^2}{192D} \tag{A.54}$$

This is the required effective diffusion coefficient. In terms of the average velocity of fluid in the cylinder, this can be written as

$$k_2 = D\left(1 + \frac{R^2 U_{avg}^2}{48D^2}\right) \tag{A.55}$$

Appendix B

An Analysis of Taylor Dispersion in a Rectangular Duct

In this appendix, the effective diffusion constant for solute dispersion in a rectangular duct is determined. This is done in order to enable use of the simplified, one-dimensional model for flow and solute concentrations in the template during nanoparticle or polymer patterning as developed in Chapter 3. The derivation follows the method of Doshi et al.[150] A steady flow of fluid containing solute is analyzed in three dimensions and the cross-sectional averaged solute density is then used to determine the effective diffusivity that must be used to accurately predict solute concentrations in a one-dimensional model.

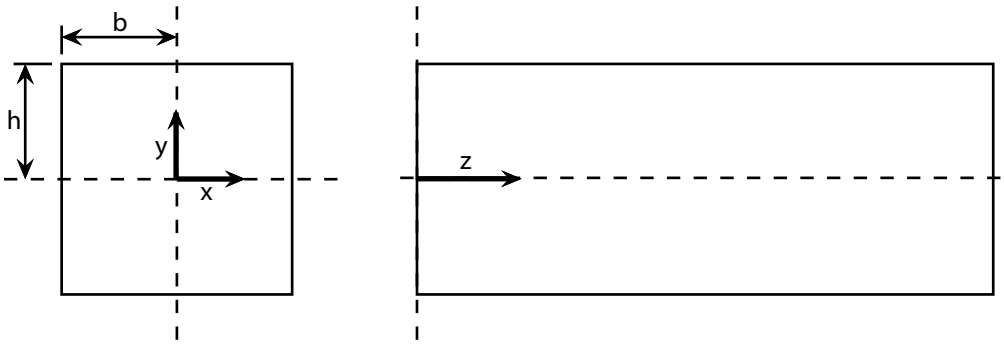

Figure B.1: An illustration of the rectangular domain, with dimensions and coordinates defined.

B.1 Fluid Flow in a Rectangular Duct

The velocity distribution $u_z(x, y)$ of fluid flowing through a rectangular duct with dimensions given by $2b$ and $2h$ is desired. This domain is shown in Figure B.1. Here, x and y are the coordinates describing position within the cross section of the conduit, while z is the coordinate describing the position along the length of the duct. The governing equations for this low Reynolds number flow describe a balance between pressure P and viscosity η, given by

$$\frac{\partial P}{\partial z} = \eta \nabla^2 u_z \tag{B.1}$$

$$\frac{\partial P}{\partial x} = 0 \tag{B.2}$$

$$\frac{\partial P}{\partial y} = 0 \tag{B.3}$$

These three equations can be reduced into a single momentum equation given by

$$\frac{dP}{dz} = \eta \nabla^2 u_z \tag{B.4}$$

The boundary conditions for this flow are

$$u_z = 0 \qquad \text{at } x = -b, b \tag{B.5}$$

$$u_z = 0 \qquad \text{at } y = -h, h \tag{B.6}$$

For this flow, the governing equation is then written in Cartesian coordinates as

$$\frac{1}{\eta}\frac{dP}{dz} = \frac{\partial^2 u_z}{\partial x^2} + \frac{\partial^2 u_z}{\partial y^2} \tag{B.7}$$

The fundamental equation for the flow of fluid in a rectangular duct can be solved by splitting the expression for u_z into two parts, such that

$$u_z = g_1(y) + g_2(x, y) \tag{B.8}$$

Using this, the equation fundamental equation can be split into two separate equations, given by

$$\frac{1}{\eta}\frac{dP}{dz} = \frac{\partial^2 g_1}{\partial y^2} \tag{B.9}$$

$$0 = \frac{\partial^2 g_2}{\partial x^2} + \frac{\partial^2 g_2}{\partial y^2} \tag{B.10}$$

where the boundary conditions are given by

$$g_1(y) = 0 \quad \text{at } y = -h,\, h \tag{B.11}$$

$$g_2(x, y) = 0 \quad \text{at } y = -h,\, h \tag{B.12}$$

$$g_2(x, y) = -g_1(y) \quad \text{at } x = -b,\, b \tag{B.13}$$

It is also noted that, given the symmetry of the equation and boundary conditions, it must be the case that

$$\left.\frac{\partial g_2}{\partial y}\right|_{y=0} = \left.\frac{\partial g_2}{\partial x}\right|_{x=0} = 0 \tag{B.14}$$

The equation for $g_1(y)$ can be solved by simple integration, which, after applying the boundary conditions from Equation B.11, results in

$$g_1(y) = \frac{h^2}{2\eta}\frac{dP}{dz}\left(\frac{y^2}{h^2} - 1\right) \tag{B.15}$$

The equation for $g_2(x, y)$ can be solved using the method of separation of variables. Let $g_2(x, y) = d(x)e(y)$, such that the equation for $g_2(x, y)$ can be written as

$$e\frac{\partial^2 d}{\partial x^2} + d\frac{\partial^2 e}{\partial y^2} = 0 \tag{B.16}$$

$$\frac{1}{d}\frac{\partial^2 d}{\partial x^2} = -\frac{1}{e}\frac{\partial^2 e}{\partial y^2} \tag{B.17}$$

Since each side of the equation is a function of a separate independent variable, each expression must be equal to a constant. In order for the boundary conditions to be satisfied, the constant must be positive. Therefore, the equation can be rewritten as

$$\frac{1}{d}\frac{\partial^2 d}{\partial x^2} = \lambda^2 \tag{B.18}$$

$$\frac{1}{e}\frac{\partial^2 e}{\partial y^2} = -\lambda^2 \tag{B.19}$$

Each of these equations can be solved by simple integration. The result is that

$$d(x) = C_1 \exp(-\lambda x) + C_2 \exp(\lambda x) \tag{B.20}$$

$$e(y) = C_3 \cos(\lambda x) + C_4 \sin(\lambda y) \tag{B.21}$$

Using the boundary conditions from Equation B.14, it can be seen that $C_1 = C_2$ and $C_4 = 0$. The equation for $g_2(x, y)$ can therefore be written as

$$g_2(x, y) = C_5 \cos(\lambda y) \cosh(\lambda x) \tag{B.22}$$

Applying the boundary condition of Equation B.12 results in

$$\lambda_m = \frac{(2m+1)\pi}{2h} \tag{B.23}$$

such that

$$g_2(x, y) = \sum_{n=0}^{\infty} A_m \cos(\lambda_m y) \cosh(\lambda_m x) \tag{B.24}$$

where A_m is the mth integration constant corresponding to the mth eigenvalue λ_m. Applying the boundary condition of Equation B.13, using the expression from Equation B.15, results in

$$-\frac{h^2}{2\eta}\frac{dP}{dz}(y^2 - 1) = \sum_{m=0}^{\infty} A_m \cos(\lambda_m y) \cosh(\lambda_m b) \tag{B.25}$$

The principle of orthogonality of the cosine function can be used to solve for the coefficients F_n. Therefore

$$\begin{aligned} -\int_{-h}^{h} \frac{h^2}{2\eta}\frac{dP}{dz}\left(\frac{y^2}{h^2} - 1\right)\cos(\lambda_m y)dy = \\ \int_{-h}^{h} \sum_{m=0}^{\infty} A_m \cos(\lambda_n y)\cos(\lambda_m y)\cosh(\lambda_m b)dy \end{aligned} \tag{B.26}$$

$$A_m h = \frac{h^2}{2\eta}\frac{dP}{dz}\frac{1}{\cosh(\lambda_m b)}\frac{32(-1)^m h}{\pi^3(2m+1)^3} \tag{B.27}$$

$$A_m = \frac{h^2}{2\eta}\frac{dP}{dz}\frac{1}{\cosh(\lambda_m b)}\frac{32(-1)^m}{\pi^3(2m+1)^3} \tag{B.28}$$

The equation for u_z can therefore be assembled, resulting in

$$u_z = \frac{h^2}{2\eta}\frac{dP}{dz}\times$$
$$\left[\frac{y^2}{h^2} - 1 + \frac{32}{\pi^3}\sum_{m=0}^{\infty}\frac{(-1)^m}{(2m+1)^3}\frac{\cosh\left(\frac{(2m+1)\pi}{2h}x\right)}{\cosh\left(\frac{(2m+1)\pi}{2h}b\right)}\cos\left(\frac{(2m+1)\pi}{2h}y\right)\right] \tag{B.29}$$

In terms of a characteristic velocity U_m given by $U_m = \frac{h^2}{2\eta}\frac{dP}{dz}$, this can be written as

$$u_z = U_m\left[1 - \frac{y^2}{h^2} - \frac{32}{\pi^3}\sum_{m=0}^{\infty}\frac{(-1)^m}{(2m+1)^3}\frac{\cosh\left(\frac{(2m+1)\pi}{2h}x\right)}{\cosh\left(\frac{(2m+1)\pi}{2h}b\right)}\cos\left(\frac{(2m+1)\pi}{2h}y\right)\right] \tag{B.30}$$

It is useful to also find the average velocity of fluid in the channel. This is done using

$$U_{avg} = \frac{1}{4bh}\int_{-h}^{h}\int_{-b}^{b} u_z dx dy \tag{B.31}$$

Performing the integration results in

$$U_{avg} = \frac{1}{4bh}\left[\frac{8bhU_m}{3} - \sum_{m=0}^{\infty}\frac{512h^2U_m}{\pi^5(2m+1)^5}\tanh\left(\frac{(2m+1)\pi b}{2h}\right)\right] \tag{B.32}$$

In terms of the aspect ratio $\alpha = h/b$, the average velocity can be expressed as

$$U_{avg} = \frac{2U_m}{3} - \sum_{m=0}^{\infty}\frac{128\alpha U_m}{\pi^5(2m+1)^5}\tanh\left(\frac{(2m+1)\pi}{2\alpha}\right) \tag{B.33}$$

For square ducts, where $\alpha = 1$, the average velocity reduces to

$$U_{avg} = 0.281U_m \tag{B.34}$$

B.2 Solute Dispersion in a Rectangular Duct

The effective diffusion constant for an equivalent one dimensional model is found by observing the dispersion of solute injected instantaneously at time $t = 0$. The concentration of solute as a function of location in the conduit and elapsed time, $C(t, x, y, z)$, is therefore desired. A mass balance on the system considering both convection and diffusion of particles results in a governing equation that can be written as

$$\frac{\partial C}{\partial t} + u_z \frac{\partial C}{\partial z} = D\left(\frac{\partial^2 C}{\partial x^2} + \frac{\partial^2 C}{\partial y^2} + \frac{\partial^2 C}{\partial z^2}\right) \tag{B.35}$$

where D is the diffusion coefficient for the solute. The initial condition is given by a pulse of solute, injected at the left side of the channel at z=0 and at time t=0, and may be described by

$$C(0, x, y, z) = \delta(z) C_0 \tag{B.36}$$

where C_0 is the constant initial concentration. The boundary conditions are obtained by noting the symmetry of the system about the origin, and by requiring that there be zero flux of particles through the wall and that the concentration of particles far from the source along the axial direction be zero. These boundary conditions are therefore given by

$$\left.\frac{\partial C}{\partial x}\right|_{x=0,b} = 0 \tag{B.37}$$

$$\left.\frac{\partial C}{\partial y}\right|_{y=0,h} = 0 \tag{B.38}$$

$$\lim_{z\to\infty} C = \lim_{z\to\infty} \frac{\partial C}{\partial z} = 0 \tag{B.39}$$

In the subsequent analysis, it will be necessary to calculate the mean concentration of particles, $C_m(t, z)$, which may be defined by

$$C_m = \frac{1}{4bh} \int_{-h}^{h} \int_{-b}^{b} C dx dy \tag{B.40}$$

Additionally, it will be useful to expand the concentration of solute in a Taylor series about the mean concentration with respect to the distance along the length of the channel. This expansion is given by

$$C = \sum_{n=0}^{\infty} f_n \frac{\partial^n C_m}{\partial z^n} \tag{B.41}$$

where $f_n(t,x,y)$ is the $\mathrm{n^{th}}$ coefficient of the Taylor series expansion.

A generalized dispersion equation is found by averaging the convective diffusion equation, Equation B.35, over the cross sectional area of the duct, resulting in

$$\begin{aligned}\frac{1}{4bh}\int_{-h}^{h}\int_{-b}^{b}\left(\frac{\partial C}{\partial t}+u_z\frac{\partial C}{\partial z}\right)dxdy=\\ \frac{D}{4bh}\int_{-h}^{h}\int_{-b}^{b}\left(\frac{\partial^2 C}{\partial x^2}+\frac{\partial^2 C}{\partial y^2}+\frac{\partial^2 C}{\partial z^2}\right)dxdy\end{aligned} \tag{B.42}$$

$$\begin{aligned}\frac{\partial C_m}{\partial t}+\frac{1}{4bh}\int_{-h}^{h}\int_{-b}^{b}\left(\frac{\partial}{\partial z}Cu_z\right)dxdy=\\ \frac{D}{4bh}\left(\int_{-h}^{h}\frac{\partial C}{\partial x}\bigg|_{-b}^{b}dy+\int_{-b}^{b}\frac{\partial C}{\partial y}\bigg|_{-h}^{h}dx\right)+D\frac{\partial^2 C_m}{\partial z^2}\end{aligned} \tag{B.43}$$

$$\frac{\partial C_m}{\partial t}+\frac{1}{4bh}\int_{-h}^{h}\int_{-b}^{b}\left(\frac{\partial}{\partial z}Cu_z\right)dxdy=D\frac{\partial^2 C_m}{\partial z^2} \tag{B.44}$$

$$\frac{\partial C_m}{\partial t}=D\frac{\partial^2 C_m}{\partial z^2}-\frac{1}{4bh}\frac{\partial}{\partial z}\int_{-h}^{h}\int_{-b}^{b}Cu_z dxdy \tag{B.45}$$

Substituting the expression for the concentration expanded about the mean, Equation B.41, results in

$$\frac{\partial C_m}{\partial t}=D\frac{\partial^2 C_m}{\partial z^2}-\frac{1}{4bh}\frac{\partial}{\partial z}\int_{-h}^{h}\int_{-b}^{b}\sum_{n=0}^{\infty}\left(f_n\frac{\partial^n C_m}{\partial z^n}\right)u_z dxdy \tag{B.46}$$

$$\frac{\partial C_m}{\partial t}=D\frac{\partial^2 C_m}{\partial z^2}-\frac{1}{4bh}\int_{-h}^{h}\int_{-b}^{b}\sum_{n=0}^{\infty}\left(f_n\frac{\partial^{n+1} C_m}{\partial z^{n+1}}\right)u_z dxdy \tag{B.47}$$

$$\frac{\partial C_m}{\partial t}=D\frac{\partial^2 C_m}{\partial z^2}-\frac{1}{4bh}\int_{-h}^{h}\int_{-b}^{b}\sum_{n=1}^{\infty}\left[\left(f_{n-1}\frac{\partial^n C_m}{\partial z^n}\right)u_z\right]dxdy \tag{B.48}$$

$$\frac{\partial C_m}{\partial t}=\sum_{n=1}^{\infty}\left(-\frac{1}{4bh}\int_{-h}^{h}\int_{-b}^{b}\left[\left(f_{n-1}\frac{\partial^n C_m}{\partial z^n}\right)u_z\right]dxdy+D\frac{\partial^n C_m}{\partial z^n}\delta_{n2}\right) \tag{B.49}$$

$$\frac{\partial C_m}{\partial t} = \sum_{n=1}^{\infty} \left[-\frac{1}{4bh} \int_{-h}^{h} \int_{-b}^{b} (f_{n-1} u_z)\, dxdy + D\delta_{n2} \right] \frac{\partial^n C_m}{\partial z^n} \tag{B.50}$$

This result can be put in the form

$$\frac{\partial C_m}{\partial t} = \sum_{n=1}^{\infty} k_n \frac{\partial^n C_m}{\partial z^n} \tag{B.51}$$

where

$$k_n = -\frac{1}{4bh} \int_{-h}^{h} \int_{-b}^{b} (f_{n-1} u_z)\, dxdy + D\delta_{n2} \tag{B.52}$$

The values of k_n are the coefficients that relate the time derivative of the mean concentration to the spatial derivatives. The second coefficient, k_2, which relates the time derivative to the second spatial derivative, acts like a diffusion coefficient. This is the desired effective diffusion coefficient for the mean concentration which can be used in the one dimensional model. This effective diffusion coefficient accounts for the shear enhanced diffusion present in the three dimensional system, allowing accurate prediction of particle concentrations in the simplified model.

An equation for f_n can be found by substituting the expanded form of the concentration function, Equation B.41, into the convective diffusion equation, Equation B.35. This results in

$$\begin{aligned} \frac{\partial}{\partial t} \left(\sum_{n=0}^{\infty} f_n \frac{\partial^n C_m}{\partial z^n} \right) + u_z \frac{\partial}{\partial z} \left(\sum_{n=0}^{\infty} f_n \frac{\partial^n C_m}{\partial z^n} \right) = \\ D \sum_{n=0}^{\infty} \left[\frac{\partial^2}{\partial x^2} \left(f_n \frac{\partial^n C_m}{\partial z^n} \right) + \frac{\partial^2}{\partial y^2} \left(f_n \frac{\partial^n C_m}{\partial z^n} \right) + \frac{\partial^2}{\partial z^2} \left(f_n \frac{\partial^n C_m}{\partial z^n} \right) \right] \end{aligned} \tag{B.53}$$

$$\begin{aligned} \sum_{n=0}^{\infty} \left(\frac{\partial f_n}{\partial t} \frac{\partial^n C_m}{\partial z^n} + f_n \frac{\partial^n}{\partial z^n} \frac{\partial C_m}{\partial t} \right) + u_z \left(\sum_{n=0}^{\infty} f_n \frac{\partial^{n+1} C_m}{\partial z^{n+1}} \right) = \\ D \sum_{n=0}^{\infty} \left(\frac{\partial^2 f_n}{\partial x^2} \frac{\partial^n C_m}{\partial z^n} + \frac{\partial^2 f_n}{\partial y^2} \frac{\partial^n C_m}{\partial z^n} + f_n \frac{\partial^{n+2} C_m}{\partial z^{n+2}} \right) \end{aligned} \tag{B.54}$$

Using the expression for the time derivative of the mean concentration as given in Equation B.51 results in

$$\sum_{n=0}^{\infty}\left[\frac{\partial f_n}{\partial t}\frac{\partial^n C_m}{\partial z^n}+f_n\frac{\partial^n}{\partial z^n}\left(\sum_{j=1}^{\infty}k_j\frac{\partial^j C_m}{\partial z^j}\right)\right]+u_z\left(\sum_{n=0}^{\infty}f_n\frac{\partial^{n+1}C_m}{\partial z^{n+1}}\right)= D\sum_{n=0}^{\infty}\left(\frac{\partial^2 f_n}{\partial x^2}\frac{\partial^n C_m}{\partial z^n}+\frac{\partial^2 f_n}{\partial y^2}\frac{\partial^n C_m}{\partial z^n}+f_n\frac{\partial^{n+2}C_m}{\partial z^{n+2}}\right) \tag{B.55}$$

$$\sum_{n=0}^{\infty}\left[\frac{\partial f_n}{\partial t}\frac{\partial^n C_m}{\partial z^n}+f_n\left(\sum_{j=1}^{\infty}k_j\frac{\partial^{j+n}C_m}{\partial z^{j+n}}\right)+u_z f_n\frac{\partial^{n+1}C_m}{\partial z^{n+1}}\right]= D\sum_{n=0}^{\infty}\left(\frac{\partial^2 f_n}{\partial x^2}\frac{\partial^n C_m}{\partial z^n}+\frac{\partial^2 f_n}{\partial y^2}\frac{\partial^n C_m}{\partial z^n}+f_n\frac{\partial^{n+2}C_m}{\partial z^{n+2}}\right) \tag{B.56}$$

The equation for the function f_n is then found by equating the coefficients of derivatives having equivalent order. This results in

$$\frac{\partial f_n}{\partial t}+\sum_{j=1}^{\infty}k_j f_{n-j}+u_z f_{n-1}=D\left(\frac{\partial^2 f_n}{\partial x^2}+\frac{\partial^2 f_n}{\partial y^2}+f_{n-2}\right) \tag{B.57}$$

The boundary conditions for this equation are found by substituting the expanded form of the concentration, Equation B.41, into the boundary conditions on the original convective diffusion equation, Equations B.37 and B.38. This results in

$$\left.\frac{\partial f_n}{\partial x}\right|_{x=0,b}=0 \tag{B.58}$$

$$\left.\frac{\partial f_n}{\partial y}\right|_{y=0,h}=0 \tag{B.59}$$

The initial condition is found in a similar manner, by substituting Equation B.41 into Equation B.36, resulting in

$$\left.\sum_{n=0}^{\infty}f_n\frac{\partial^n C_m}{\partial z^n}\right|_{t=0}=\delta(z)C_0 \tag{B.60}$$

At time $t=0$, the mean concentration is simply C_0 for $z=0$ and is equal to zero otherwise. Therefore

$$\left.\sum_{n=0}^{\infty}f_n\frac{\partial^n}{\partial z^n}C_0\delta(z)\right|_{t=0}=\delta(z)C_0 \tag{B.61}$$

$$f_n(0, x, y) = 1 \tag{B.62}$$

At this point, Equation B.57 can be solved for f_0. The equation for f_0 is reduced to

$$\frac{\partial f_0}{\partial t} = D\left(\frac{\partial^2 f_0}{\partial x^2} + \frac{\partial^2 f_0}{\partial y^2}\right) \tag{B.63}$$

This equation can be solved using separation of variables. After solving and applying the boundary conditions from Equations B.58 and B.59, the expression for f_0 becomes

$$f_0 = \sum_{m=0}^{\infty}\sum_{n=0}^{\infty} A_{mn}\cos\left(\frac{n\pi x}{b}\right)\cos\left(\frac{m\pi y}{h}\right)\exp\left[-tD\pi^2\left(\frac{m^2}{h^2}+\frac{n^2}{b^2}\right)\right] \tag{B.64}$$

where A_{mn} is the integration constant corresponding to the mth and nth eigenvalues. Applying the initial condition of Equation B.62 results in the determination that

$$A_{mn} = \begin{cases} 1 & \text{for } n = m = 0 \\ 0 & \text{otherwise} \end{cases} \tag{B.65}$$

Therefore, the expression for f_0 reduces to

$$f_0 = 1 \tag{B.66}$$

With f_0 determined, k_1 can be found. The expression for k_1 is reduced from Equation B.52, resulting in

$$k_1 = -\frac{1}{4bh}\int_{-h}^{h}\int_{-b}^{b} u_z dx dy \tag{B.67}$$

Substituting for the velocity from Equation B.30 and performing the integration results in

$$k_1 = -U_m\left[\frac{2}{3} - \frac{128}{\pi^5}\frac{h}{b}\sum_{j=0}^{\infty}\frac{1}{(2j+1)^5}\tanh\left(\frac{(2j+1)\pi b}{2h}\right)\right] \tag{B.68}$$

With k_1 determined, an expression for f_1 may now be sought. Again returning to the fundamental equation for f_n, Equation B.57, and reducing the equation to solve for f_1, the result is obtained that

$$\frac{\partial f_1}{\partial t} + k_1 + u_z = D\left(\frac{\partial^2 f_1}{\partial x^2} + \frac{\partial^2 f_1}{\partial y^2}\right) \tag{B.69}$$

The solution to this equation, which satisfies boundary conditions of Equation B.58 and B.59, is given by

$$f_1 = \sum_{m=0}^{\infty}\sum_{n=0}^{\infty} B_{mn}\cos\left(\frac{n\pi y}{h}\right)\cos\left(\frac{m\pi x}{b}\right)\left(1-\exp\left[-\pi^2 tD\left(\frac{m^2}{b^2}+\frac{n^2}{h^2}\right)\right]\right) \tag{B.70}$$

The constants B_{mn} can be found using the orthogonality properties of the cosine function such that the solution for f_1, Equation B.70, satisfies the governing differential equation, Equation B.69. Therefore

$$\frac{k_1+u_z}{D} = \sum_{m=0}^{\infty}\sum_{n=0}^{\infty} B_{mn}\left(-\frac{m^2\pi^2}{b^2}-\frac{n^2\pi^2}{h^2}\right)\cos\left(\frac{n\pi y}{h}\right)\cos\left(\frac{m\pi x}{b}\right) \tag{B.71}$$

Applying the concept of orthogonality results in

$$\int_{-h}^{h}\int_{-b}^{b}\frac{k_1+u_z}{D}\cos\left(\frac{q\pi y}{h}\right)\cos\left(\frac{r\pi x}{b}\right)dxdy = \int_{-h}^{h}\int_{-b}^{b}\sum_{m=0}^{\infty}\sum_{n=0}^{\infty} B_{mn}$$
$$\left(-\frac{m^2\pi^2}{b^2}-\frac{n^2\pi^2}{h^2}\right)\cos\left(\frac{n\pi y}{h}\right)\cos\left(\frac{m\pi x}{b}\right)\cos\left(\frac{q\pi y}{h}\right)\cos\left(\frac{r\pi x}{b}\right)dxdy \tag{B.72}$$

$$-B_{mn}\left(\frac{m^2\pi^2}{b^2}-\frac{n^2\pi^2}{h^2}\right)hb = \int_{-h}^{h}\int_{-b}^{b}\frac{k_1+u_z}{D}\cos\left(\frac{n\pi y}{h}\right)\cos\left(\frac{m\pi x}{b}\right)dxdy \tag{B.73}$$

Equation B.73 can be used to solve for B_{mn} for all cases except when $m = n = 0$. In this case, Equation B.40 can be combined with Equation B.41 to form another condition that can be used to solve for B_{00}

$$C_m = \frac{1}{4bh}\int_{-h}^{h}\int_{-b}^{b}\sum_{n=0}^{\infty} f_n\frac{\partial^n C_m}{\partial z^n}dxdy \tag{B.74}$$

$$\frac{\partial^n C_m}{\partial z^n}\delta_{n0} = \frac{1}{4bh}\sum_{n=0}^{\infty}\left(\int_{-h}^{h}\int_{-b}^{b} f_n dxdy\frac{\partial^n C_m}{\partial z^n}\right) \tag{B.75}$$

Equating like orders of derivatives results in the equation

$$\frac{1}{4bh}\int_{-h}^{h}\int_{-b}^{b} f_n dxdy = \delta_{n0} \tag{B.76}$$

With $n = 1$, this gives

$$\frac{1}{4bh}\int_{-h}^{h}\int_{-b}^{b} f_1 dxdy = 0 \tag{B.77}$$

It therefore follows that

$$B_{00} = 0 \tag{B.78}$$

The resulting expressions for B_{mn} are

$$B_{00} = 0 \tag{B.79}$$

$$B_{0n} = \frac{4(-1)^n h^2 U_m}{\pi^4 n^4 D} + \frac{256(-1)^{n+1} U_m bh}{\pi^7 D n^2}\sum_{j=0}^{\infty}\frac{\tanh\left[\frac{(2j+1)\pi b}{2h}\right]}{(2j+1)^3(2n+2j+1)(2n-2j-1)} \tag{B.80}$$

$$B_{m0} = \frac{256(-1)^{m+1} U_m h^3}{\pi^7 D b m^2}\sum_{j=0}^{\infty}\frac{\tanh\left[\frac{(2j+1)\pi b}{2h}\right]}{(2j+1)^2(2j-1)[(2j+1)^2 + 4m^2h^2/b^2]} \tag{B.81}$$

$$B_{mn} = \frac{512(-1)^{m+n+1} U_m bh^3}{\pi^7 D[b^2m^2 + n^2h^2]} \times \sum_{j=0}^{\infty}\frac{\tanh\left[\frac{(2j+1)\pi b}{2h}\right]}{(2j+1)(2n+2j+1)(2n-2j-1)[(2j+1)^2 + 4m^2h^2/b^2]} \tag{B.82}$$

The effective diffusion coefficient k_2 can now be determined from Equation B.52, with $n = 2$, resulting in

$$k_2 = -\frac{1}{4bh}\int_{-h}^{h}\int_{-b}^{b}(f_1 u_z)\, dxdy + D \tag{B.83}$$

$$k_2 - D = -\frac{1}{4bh}\sum_{m=0}^{\infty}\sum_{n=0}^{\infty} B_{mn}\left(1-\exp\left[-\pi^2 tD\left(\frac{m^2}{b^2}+\frac{n^2}{h^2}\right)\right]\right) \int_{-h}^{h}\int_{-b}^{b}\cos\left(\frac{n\pi y}{h}\right)\cos\left(\frac{m\pi x}{b}\right)u_z dxdy \tag{B.84}$$

For $m \neq 0$ and $n \neq 0$, the integral can be evaluated as

$$\int_{-h}^{h}\int_{-b}^{b} u_z \cos\left(\frac{n\pi y}{h}\right)\cos\left(\frac{m\pi x}{b}\right)dxdy = \frac{512(-1)^{m+n}h^2U_m}{\pi^5} \times\sum_{j=0}^{\infty}\left(\frac{\tanh\left[\frac{(2j+1)b\pi}{2h}\right]}{[(2j+1)^2+4m^2h^2/b^2](2n+2j+1)(2n-2j-1)(2j+1)}\right) \tag{B.85}$$

$$\int_{-h}^{h}\int_{-b}^{b} u_z \cos\left(\frac{n\pi y}{h}\right)\cos\left(\frac{m\pi x}{b}\right)dxdy = -B_{mn}\frac{\pi^2 D(b^2m^2+n^2h^2)}{bh} \tag{B.86}$$

For $m = 0$ and $n \neq 0$, the integral can be evaluated as

$$\int_{-h}^{h}\int_{-b}^{b} u_z \cos\left(\frac{n\pi y}{h}\right)\cos\left(\frac{m\pi x}{b}\right)dxdy = -\frac{8(-1)^n U_m bh}{\pi^2 n^2}+ \frac{512(-1)^n h^2 U_m}{\pi^5}\sum_{j=0}^{\infty}\left(\frac{\tanh\left[\frac{(2j+1)b\pi}{2h}\right]}{(2j+1)^3(2n+2j+1)(2n-2j-1)}\right) \tag{B.87}$$

$$\int_{-h}^{h}\int_{-b}^{b} u_z \cos\left(\frac{n\pi y}{h}\right)\cos\left(\frac{m\pi x}{b}\right)dxdy = -B_{0n}\frac{2\pi^2 Dn^2 b}{h} \tag{B.88}$$

For $m \neq 0$ and $n = 0$, the integral can be evaluated as

$$\int_{-h}^{h}\int_{-b}^{b} u_z \cos\left(\frac{n\pi y}{h}\right)\cos\left(\frac{m\pi x}{b}\right)dxdy = -\frac{512(-1)^m h^2 U_m}{\pi^5} \times\sum_{j=0}^{\infty}\left(\frac{\tanh\left[\frac{(2j+1)b\pi}{2h}\right]}{[(2j+1)^2+4m^2h^2/b^2](2j+1)^3}\right) \tag{B.89}$$

$$\int_{-h}^{h}\int_{-b}^{b} u_z \cos\left(\frac{n\pi y}{h}\right)\cos\left(\frac{m\pi x}{b}\right)dxdy = -B_{m0}\frac{2\pi^2 Dm^2 h}{b} \tag{B.90}$$

From here, an expression for k_2 can be assembled, resulting in

$$\begin{aligned} k_2 - D = \frac{1}{4bh}\sum_{m=0}^{\infty}\sum_{n=0}^{\infty} B_{mn}\left(1-\exp\left[-\pi^2 tD\left(\frac{m^2}{b^2}+\frac{n^2}{h^2}\right)\right]\right) \\ \left(B_{mn}\frac{\pi^2 D(h^2m^2+n^2b^2)}{bh}(1+\delta_{m0}+\delta_{n0})\right) \end{aligned} \tag{B.91}$$

$$\begin{aligned} k_2 = D\left[1+\frac{\pi^2}{4}\sum_{m=0}^{\infty}\sum_{n=0}^{\infty} B_{mn}^2\left(\frac{m^2}{b^2}+\frac{n^2}{h^2}\right)(1+\delta_{m0}+\delta_{n0})\right. \\ \left.\times\left(1-\exp\left[-\pi^2 tD\left(\frac{m^2}{b^2}+\frac{n^2}{h^2}\right)\right]\right)\right] \end{aligned} \tag{B.92}$$

This is the dispersion coefficient. For a square duct, in terms of the average velocity of fluid in the cylinder, this can also be written as

$$\begin{aligned} k_2 = D\left[1+\frac{\pi^2}{4}\sum_{m=0}^{\infty}\sum_{n=0}^{\infty} C_{nm}^2\left(\frac{m^2}{b^2}+\frac{n^2}{h^2}\right)(1+\delta_{m0}+\delta_{n0})\right. \\ \left.\times\left(1-\exp\left[-\pi^2 tD\left(\frac{m^2}{b^2}+\frac{n^2}{h^2}\right)\right]\right)\right] \end{aligned} \tag{B.93}$$

where

$$C_{00} = 0 \tag{B.94}$$

$$\begin{aligned} C_{0n} = \frac{4(-1)^n h^2 U_{avg}}{0.281\pi^4 n^4 D} + \frac{256(-1)^{n+1}U_{avg}bh}{0.281\pi^7 Dn^2} \\ \times\sum_{j=0}^{\infty}\frac{\tanh\left[\frac{(2j+1)\pi b}{2h}\right]}{(2j+1)^3(2n+2j+1)(2n-2j-1)} \end{aligned} \tag{B.95}$$

$$C_{m0} = \frac{256(-1)^{m+1}U_{avg}h^3}{0.281\pi^7 Dbm^2}\sum_{j=0}^{\infty}\frac{\tanh\left[\frac{(2j+1)\pi b}{2h}\right]}{(2j+1)^2(2j-1)[(2j+1)^2+4m^2h^2/b^2]} \tag{B.96}$$

$$C_{nm} = \frac{512(-1)^{m+n+1} U_{avg} b h^3}{0.281 \pi^7 D[b^2 m^2 + n^2 h^2]} \times \sum_{j=0}^{\infty} \frac{\tanh\left[\frac{(2j+1)\pi b}{2h}\right]}{(2j+1)(2n+2j+1)(2n-2j-1)[(2j+1)^2 + 4m^2 h^2/b^2]} \tag{B.97}$$

Appendix C

An Analytical Solution for Solute Dispersion in a Channel with No Diffusion

C.1 Filling Stage

In the case where diffusion is neglected ($k_2 = 0$), an analytical solution to the governing equations for concentration as a function of position and time in the one dimensional model is possible. For the solute filling process, the Equation 3.16 reduces to

$$\frac{\partial \bar{C}_m}{\partial \bar{t}} = \frac{\partial \bar{C}_m}{\partial \bar{z}}(\bar{z} - 1) + \bar{C}_m \tag{C.1}$$

while the boundary and initial conditions are the same as in Equations 3.17, 3.18, and 3.19.

First, the solution to the asymptotic steady state solution, C_{m-ss}, must be found. As $t \to \infty$, Equation C.1 reduces to

$$0 = \frac{\partial \bar{C}_{m-ss}}{\partial \bar{z}}(\bar{z} - 1) + \bar{C}_{m-ss} \tag{C.2}$$

with boundary condition given by

$$\bar{C}_{m-ss}(t, z = 0) = 1 \tag{C.3}$$

The solution can be found by simple integration. Therefore

$$\frac{\partial \bar{C}_{m-ss}}{\partial \bar{z}} = \frac{\bar{C}_{m-ss}}{1-\bar{z}} \tag{C.4}$$

$$\int \frac{1}{\bar{C}_{m-ss}} d\bar{C}_{m-ss} = \int \frac{1}{1-\bar{z}} dz \tag{C.5}$$

$$\ln \bar{C}_{m-ss} = -\ln(1-\bar{z}) + C_1 \tag{C.6}$$

where C_1 is a constant of integration. Applying the boundary condition and simplifying gives

$$\bar{C}_{m-ss} = \frac{1}{1-\bar{z}} \tag{C.7}$$

With the asymptotic steady state solution determined, the transient solution may be found by considering the physical operation of the system in the case where diffusion is negligible. That is, consider an arbitrary volume of fluid entering the channel at an arbitrary time. The mass of solute in this volume of fluid is fixed as the volume travels through the channel, since there is no diffusion to cause particles to migrate in or out of the control volume. The volume travels through the channel as dictated by the velocity of the fluid in the channel, but becomes less as solute is evaporated through the vapor permeable polymer template. Since the velocity and evaporation rates are not functions of time, it must be true that all such volumes entering at any time behave the same way, including a volume of fluid entering in the limit as time $t \to \infty$. Thus, the concentration for any such volume must trace the steady state concentration profile. Now, consider the first volume of fluid to enter the channel, starting at time $t = 0$. The distance that this volume of fluid travels is given by simply integrating the velocity.

$$v = \frac{\partial z}{\partial t} = \frac{q'' P_p}{A}(L_0 - z) \tag{C.8}$$

$$\int_0^d \frac{1}{L_0 - z} dz = \int_0^t \frac{q'' P_p}{A} dt \tag{C.9}$$

$$-\ln \frac{L_0 - d}{L_0} = \frac{q'' P_p}{A} t \tag{C.10}$$

$$\frac{L_0 - d}{L_0} = \exp\left(-\frac{t}{t_s}\right) \tag{C.11}$$

$$d = L_0 \left[1 - \exp\left(-\frac{t}{t_s}\right)\right] \tag{C.12}$$

In dimensionless form, this is

$$\frac{d}{L_0} = [1 - \exp(-\bar{t})] \tag{C.13}$$

To the left of this position, there are particles in the fluid. To the right, there are no particles. Therefore, the final solution is given by the steady state solution modified by a unit step function, given by

$$\bar{C}_m = \frac{1}{1-\bar{z}} u[1 - \exp(-\bar{t}) - \bar{z}] \tag{C.14}$$

The solution can be confirmed by substituting into Equation C.1. This results in

$$\begin{aligned} \frac{1}{1-\bar{z}}\delta[1-\exp(-\bar{t})-\bar{z}]\exp(-\bar{t}) = \\ \left[\frac{1}{(1-\bar{z})^2}u[1-\exp(-\bar{t})-\bar{z}] - \frac{1}{1-\bar{z}}\delta[1-\exp(-\bar{t})-\bar{z}]\right](\bar{z}-1) \\ +\frac{1}{1-\bar{z}}u[1-\exp(-\bar{t})-\bar{z}] \end{aligned} \tag{C.15}$$

$$\begin{aligned} \frac{1}{1-\bar{z}}\delta[1-\exp(-\bar{t})-\bar{z}]\exp(-\bar{t}) = \\ \left[-\frac{1}{1-\bar{z}}u[1-\exp(-\bar{t})-\bar{z}] + \delta[1-\exp(-\bar{t})-\bar{z}]\right] \\ +\frac{1}{1-\bar{z}}u[1-\exp(-\bar{t})-\bar{z}] \end{aligned} \tag{C.16}$$

$$\frac{1}{1-\bar{z}}\delta(1-\exp(-\bar{t})-\bar{z})\exp(-\bar{t}) = \delta(1-\exp(-\bar{t})-\bar{z}) \tag{C.17}$$

$$[1-\bar{z}-\exp(-\bar{t})]\delta(1-\exp(-\bar{t})-\bar{z}) = 0 \tag{C.18}$$

To check the equality of the above equation, let

$$y = 1 - \bar{z} - \exp(-\bar{t}) \tag{C.19}$$

The equation then becomes

$$y\delta(y) = 0 \tag{C.20}$$

The equation is clearly satisfied for $y \neq 0$. For the case of $y = 0$, consider the integral of the above expression across the region an arbitrary distance ϵ on either side of $y = 0$. Integration by parts gives

$$\int_{-\epsilon}^{\epsilon} y\delta(y)dy = yu(y)\Big|_{-\epsilon}^{\epsilon} - \int_{-\epsilon}^{\epsilon} u(y)dy \tag{C.21}$$

$$\int_{-\epsilon}^{\epsilon} y\delta(y)dy = \epsilon - \int_{0}^{\epsilon} 1dy \tag{C.22}$$

$$\int_{-\epsilon}^{\epsilon} y\delta(y)dy = \epsilon - \epsilon \tag{C.23}$$

$$\int_{-\epsilon}^{\epsilon} y\delta(y)dy = 0 \tag{C.24}$$

Therefore, the equality holds even at $y = 0$. Since the equality therefore holds at all values of y, the proposed solution is indeed correct.

C.2 Drying Stage

The filling stage continues as described above until the channel fills completely with solute at some area. Once this maximum concentration is reached, the drying stage begins. This transition occurs at a time t_f that can be determined by equating concentration in the filling stage solution to the saturation concentration of solute, denoted symbolically as C_f. This maximum concentration is achieved at a position of L_f, which is different from the length of the channel L_0 as a result of the zero diffusion assumption as well as the assumption that there is no evaporative flux through the end of the channel. Using these values in Equation C.1 gives

$$\frac{C_f}{C_0} = \frac{1}{1 - \frac{L_f}{L_0}} u\left(1 - \exp\left(-\frac{t_f}{t_s}\right) - \frac{L_f}{L_0}\right) \tag{C.25}$$

Equating the coefficient of the unit step function to the dimensionless final concentration gives

$$L_f = L_0\left(1 - \frac{C_0}{C_f}\right) \tag{C.26}$$

Equating the argument of the unit step function to zero gives the time at which the channel transitions to the drying phase, which results in

$$1 - \exp\left(-\frac{t_f}{t_s}\right) - \frac{L_f}{L_0} = 0 \tag{C.27}$$

$$t_f = t_s \ln\left[\frac{1}{1 - \frac{L_f}{L_0}}\right] \tag{C.28}$$

Combining with the result from Equation C.26 results in

$$t_f = t_s \ln\left[\frac{C_f}{C_0}\right] \tag{C.29}$$

In the case where diffusion is neglected ($k_2 = 0$) the governing equation for the system can be reduced to

$$\frac{\partial \bar{C}_m}{\partial \bar{z}}\left(\bar{z} - \frac{L_x(\bar{t})}{L_0}\right) + \bar{C}_m = 0 \tag{C.30}$$

as described in Chapter 3. The solution can be found by simple integration. Therefore

$$\frac{\partial \bar{C}_m}{\partial \bar{z}} = \frac{\bar{C}_m}{\frac{L_x(\bar{t})}{L_0} - \bar{z}} \tag{C.31}$$

$$\int \frac{1}{\bar{C}_m} d\bar{C}_m = \int \frac{1}{\frac{L_x(\bar{t})}{L_0} - \bar{z}} dz \tag{C.32}$$

$$\ln \bar{C}_m = -\ln\left(\frac{L_x(\bar{t})}{L_0} - \bar{z}\right) + R_1 \tag{C.33}$$

$$\bar{C}_m = \frac{R_1}{\frac{L_x(\bar{t})}{L_0} - \bar{z}} \tag{C.34}$$

where R_1 is a constant of integration. Applying the boundary condition from Equation 3.27 and simplifying gives

$$\bar{C}_m = \frac{1}{1 - \frac{L_0 \bar{z}}{L_x(\bar{t})}} \tag{C.35}$$

Applying the boundary condition from Equation 3.28 results in

$$\frac{C_f}{C_0} = \frac{1}{1 - \frac{L(\bar{t})}{L_x(\bar{t})}} \tag{C.36}$$

$$L_x(\bar{t}) = \frac{L(\bar{t})}{1 - \frac{C_0}{C_f}} \tag{C.37}$$

To find the filled length as a function of time, a simple mass balance on the solute in the system can be performed. The total mass of solute, m_{tot}, is first found by integrating the concentration over the length of the channel at an arbitrary time. This gives

$$m_{tot} = A\int_0^{L(\bar{t})} C_m dx + A\int_{L(\bar{t})}^{L_0} C_f dx \tag{C.38}$$

$$m_{tot} = A\int_0^{L(\bar{t})} \frac{C_0}{1-\frac{L_0\bar{z}}{L_x(\bar{t})}} dx + A\int_{L(\bar{t})}^{L_0} C_f dx \tag{C.39}$$

$$m_{tot} = AC_0 \ln\left(1-\frac{L_0 L(\bar{t})}{L_x(\bar{t})}\right) + AC_f(L_0 - L(\bar{t})) \tag{C.40}$$

The time rate of change of the total mass in the system is therefore given by

$$\dot{m}_{tot} = -AC_0L_0\frac{1}{1-\frac{L_0L(\bar{t})}{L_x(\bar{t})}}\left[\frac{\dot{L}(\bar{t})}{L_x(\bar{t})} - \frac{L(\bar{t})\dot{L}_x(\bar{t})}{L_x(\bar{t})^2}\right] - AC_f\dot{L}(\bar{t}) \tag{C.41}$$

Substituting the expression for $L_x(\bar{t})$ and simplifying results in the expression

$$\dot{m}_{tot} = -AC_f\dot{L}(\bar{t}) \tag{C.42}$$

The additional mass in the system is supplied through the inlet to the channel, and is given by the expression

$$\dot{m}_{tot} = C_0Av(t, z=0) \tag{C.43}$$

Substituting for the velocity using Equation 3.20 results in

$$\dot{m}_{tot} = C_0A\frac{q" P_p}{A}L(\bar{t}) \tag{C.44}$$

Equating the two expressions for the mass flow rate of solute results in

$$AC_f\dot{L}(\bar{t}) = -C_0A\frac{q" P_p}{A}L(\bar{t}) \tag{C.45}$$

$$\frac{\dot{L}(\bar{t})}{L(\bar{t})} = -\frac{C_0}{C_f}\frac{q" P_p}{A} \tag{C.46}$$

Integrating results in

$$\int_{L_f}^{L(\bar{t})} \frac{1}{L} dL = -\int_{t_f}^{t} \frac{C_0}{C_f} \frac{q" P_p}{A} dt \tag{C.47}$$

$$\ln\left(\frac{L(\bar{t})}{L_f}\right) = -\frac{C_0}{C_f} \frac{q" P_p}{A} (t - t_f) \tag{C.48}$$

$$L(\bar{t}) = L_f \exp\left(-\frac{C_0}{C_f} \frac{t - t_f}{t_s}\right) \tag{C.49}$$

Appendix D

Synthesis Procedure for Poly(4-methyl-2-pentyne)

An example recipe for synthesis of poly(4-methyl-2-pentyne) is given below. The recipe was scaled linearly depending on the volume of polymer desired. The procedure was performed in a nitrogen glovebox until the polymerization was complete, at which time the polymer was removed from the glovebox and the remaining procedure performed in a fume hood with ambient environment.

1. Combine 0.264 g niobium pentachloride with 0.428 g triphenyl bismuth in 21.6 mL of toluene to form the catalyst solution.
2. Stir the catalyst solution at 90 °C for 10 min.
3. Combine 2 g (2.8 mL) 4-methyl-2-pentyne in 2.8 mL of toluene to form the monomer solution.
4. Add the monomer solution dropwise to the catalyst solution, stirring constantly. The solution should gel quickly as the polymer is formed.
5. Hold the gelled polymer at 90 °C for 1 hour to ensure completion of the reaction.
6. Separate the gelled polymer from any remaining liquid toluene. Wash the gelled polymer with methanol, remove the polymer from the methanol, and dry the polymer under vacuum to remove all of the toluene from the gelled polymer.

7. Dissolve the polymer in 100 mL of cyclohexane. This dissolution will occur slowly, and can take in excess of 24 hours to dissolve completely. Periodic agitation will assist dissolution.

8. Precipitate the dissolved polymer in a large volume of methanol. This can be done by pipetting the dissolved polymer in 2 mL quantities into 400 mL of methanol, followed by closing the container and violently agitating the mixture after each addition of polymer solution.

9. Filter the polymer to remove the precipitated polymer from the methanol. This can be done using a polypropylene filter with 25 μm pores mounted in a vacuum filtration system.

10. Dry the removed polymer under vacuum to remove any remaining methanol, and re-dissolve in 100 mL of cyclohexane.

11. Repeat the previous three steps to re-precipitate and dissolve the polymer in cyclohexane, to ensure all of the catalyst is removed.

12. Dissolve the polymer in 100 mL of cyclohexane to prepare for solution casting.

Appendix E

Derivation of the Gibbs-Thomson Equation for Melting Temperature of a Spherical Nanoparticle

In this appendix, a first order approximation of the change in melting temperature of a nanoparticle as a function of the particle radius is developed. The system under consideration is that of a single nanoparticle under transition from solid to liquid, isolated from all other such solids or liquids. The following derivation follows that done by Buffat et al.[127]

A transition between a solid and a liquid phase occurs when the chemical potential of the two phases are equal, or $\mu_s = \mu_l$. The chemical potential can be expanded in a Taylor series around the bulk melting point temperature and pressure, $T_{m,\infty}$ and $P_{m,\infty}$. Keeping only the first-order terms results in

$$\mu_s(T_m, P_s) = \mu(T_{m,\infty}, P_{m,\infty}) + \left.\frac{\partial \mu_s}{\partial T}\right|_P (T_m - T_{m,\infty}) + \left.\frac{\partial \mu_s}{\partial P}\right|_T (P_s - P_{m,\infty}) \quad \text{(E.1)}$$

$$\mu_l(T_m, P_l) = \mu(T_{m,\infty}, P_{m,\infty}) + \left.\frac{\partial \mu_l}{\partial T}\right|_P (T_m - T_{m,\infty}) + \left.\frac{\partial \mu_l}{\partial P}\right|_T (P_l - P_{m,\infty}) \quad \text{(E.2)}$$

where T_m is the melting temperature of the particle, P_s is the pressure in the solid and P_l is the pressure in the liquid. Using the phase transfer condition

$\mu_s(T_m, P_s) = \mu_l(T_m, P_l)$ and the fact that chemical potentials of phases at the bulk melting temperature and pressure are also equal, the difference in the two above equations results in

$$\begin{aligned} 0 = \left(\left.\frac{\partial \mu_l}{\partial T}\right|_P - \left.\frac{\partial \mu_s}{\partial T}\right|_P \right) (T_m - T_{m,\infty}) + \\ \left(\left.\frac{\partial \mu_l}{\partial P}\right|_T (P_l - P_{m,\infty}) - \left.\frac{\partial \mu_s}{\partial P}\right|_T (P_s - P_{m,\infty}) \right) \end{aligned} \tag{E.3}$$

The partial derivatives can be evaluated by considering the Gibbs-Duhem equation, which is

$$-VdP + SdT + md\mu = 0 \tag{E.4}$$

where V is the volume of the particle, S is the entropy, and m is the mass. It follows that

$$\left.\frac{\partial \mu}{\partial T}\right|_P = -\frac{S}{m} = -s \tag{E.5}$$

and

$$\left.\frac{\partial \mu}{\partial P}\right|_T = -\frac{V}{m} = \frac{1}{\rho} \tag{E.6}$$

where s is the specific entropy and ρ is the density. Therefore

$$0 = (s_s - s_l)(T_m - T_{m,\infty}) + \left(\frac{1}{\rho}(P_l - P_{m,\infty}) - \frac{1}{\rho}(P_s - P_{m,\infty}) \right) \tag{E.7}$$

$$0 = (s_s - s_l)(T_m - T_{m,\infty}) + \frac{1}{\rho}(P_l - P_s) \tag{E.8}$$

The change in entropy associated with the phase change is related to the enthalpy of fusion $\Delta H_{m,\infty}$ by

$$(s_l - s_s) = \frac{\Delta H_{m,\infty}}{T_0} \tag{E.9}$$

The change in pressure between the two phases can be found by considering the different surface energies of the two phases. The pressure inside a sphere with radius r_p and surface tension γ may be found using the concept of virtual work. At equilibrium, the system must be an energy minimum.

That is, any small change in the radius of the droplet must not cause any incremental change in work. Therefore

$$\Delta P dV = \gamma dA \tag{E.10}$$

where ΔP is the pressure acting across the interface and A is the surface area. The change in surface area with respect to volume may be calculated as

$$\frac{dA}{dV} = \frac{dA}{dr}\frac{dr}{dV} \tag{E.11}$$

For a sphere, $A = 4\pi r_p^2$ and $V = \frac{4}{3}\pi r_p^3$. Therefore

$$\frac{dA}{dV} = \frac{2}{r_p} \tag{E.12}$$

The result is that

$$\Delta P = \frac{2\gamma}{r_p} \tag{E.13}$$

For the solid and liquid droplets, this results in

$$P_s - P_\infty = \frac{2\gamma_s}{r_p} \tag{E.14}$$

$$P_l - P_\infty = \frac{2\gamma_l}{r_p} \tag{E.15}$$

where P_∞ is the atmospheric pressure. The difference in the two pressures is therefore

$$P_l - P_s = \frac{2(\gamma_l - \gamma_s)}{r_p} \tag{E.16}$$

Substituting the expressions for the change in entropy and pressure into the phase equilibrium condition results in

$$0 = -\Delta H_{m,\infty}\frac{(T_m - T_{m,\infty})}{T_{m,\infty}} + \frac{1}{\rho}\frac{2(\gamma_l - \gamma_s)}{r_p} \tag{E.17}$$

$$T_m = T_{m,\infty}\left[1 - \frac{2(\gamma_s - \gamma_l)}{\rho r_p \Delta H_{m,\infty}}\right] \tag{E.18}$$

This is the Gibbs-Thomson equation, describing the variation in melting temperature caused by a finite particle radius.